MULTISCALE MODELING OF NANOPOROUS MATERIALS FOR ADSORPTIVE SEPARATIONS

A Dissertation
Presented to
The Academic Faculty

by

Ambarish R. Kulkarni

In Partial Fulfillment
of the Requirements for the Degree
Doctor of Philosophy in the
School of Chemical and Biomolecular Engineering

Georgia Institute of Technology
December 2014

MULTISCALE MODELING OF NANOPOROUS MATERIALS FOR ADSORPTIVE SEPARATIONS

Approved by:

Dr. David S. Sholl, Advisor
School of Chemical and Biomolecular Engineering
Georgia Institute of Technology

Dr. Christopher W. Jones, Co-advisor
School of Chemical and Biomolecular Engineering
Georgia Institute of Technology

Dr. Krista S. Walton
School of Chemical and Biomolecular Engineering
Georgia Institute of Technology

Dr. Yoshiaki Kawajiri
School of Chemical and Biomolecular Engineering
Georgia Institute of Technology

Dr. Srinivas Garimella
School of Mechanical Engineering
Georgia Institute of Technology

Date Approved: October 14, 2014

To friends & family

ACKNOWLEDGEMENTS

The time that I have spent at Georgia Tech working on my PhD thesis has been one of the most rewarding periods of my life, largely due to the people I have met and interacted with over the years.

First and foremost, I would like to thank my thesis supervisor, Dr. David S. Sholl for the continued support and patience during my doctoral work. In addition to being a great mentor and an incredible teacher, he has provided invaluable lessons regarding work ethic, time management and research philosophy. Even after being in his group for 5 years, I am still amazed by his dedication to the students and his involvement in the technical details of their work. I shall forever remain grateful for his advice and willingness to discuss my future career. For all this and much more, I shall always be indebted...

I must express special gratitude to my thesis co-advisor, Dr. Christopher W. Jones. Working with him on the Air Capture project has been quite an experience and I would like to thank him for his constant support and encouragement. It has indeed been a pleasure working with someone as motivated and energetic as him.

I have been very fortunate to have a group of excellent researchers and experimental collaborators as part of my thesis committee. I would like to thank Dr. Krista S. Walton, Dr. Yoshiaki Kawajiri and Dr. Srinivas Garimella for their guidance and genuine interest in my PhD work. A special thanks to Dr. Sankar Nair, whose experimental knowledge provided a very useful perspective towards the latter part of my PhD work. I must also acknowledge the contributions of Dr. Preeti Kamakoti for her

advice on both technical and non-technical aspects over the last few years. The chaotic teleconferences and joint meetings with the collaborators shall always be fondly remembered.

During my time at Georgia Tech, I had the pleasure of directly working with many members of Sholl and Jones group. Specifically, I would like to thank Taku, Ji, Hanjun, Emmanuel, Sung Gu, Rohan, Jason, Praveen and Steph for all the discussions technical, and otherwise.

A very fond thank you to the Indian gang - Dhaval, Prashant, Pramod, Prabuddha, Praveen, Meha, Nitesh, Aritra, Rohan, Paras, Gautami, Pradnya, Shweta and Jaya. The time spent together, the dinners and the road trips were as good as being home.

If it not were for my parents and families constant encouragement, I would have never pursued a PhD. I am eternally grateful for all that they have done and the compromises that they have made to ensure my happiness.

To the one person that I am indebted to, beyond what words can describe - to Tanu. There is absolutely no way I could imagine Georgia Tech without the endless love, the warm support and the constant motivation.

-Ambarish Kulkarni, Atlanta, October 2014

TABLE OF CONTENTS

LIST OF TABLES

LIST OF FIGURES

LIST OF SYMBOLS AND ABBREVIATIONS

CBMC	Configurational Bias Monte Carlo
DFT	Density Functional Theory
FF	Force Field
GCMC	Grand Canonical Monte Carlo
MC	Monte Carlo
MD	Molecular Dynamics
MOF	Metal-Organic Framework
PES	Potential Energy Surface
PSA	Pressure Swing Adsorption
TSA	Temperature Swing Adsorption

SUMMARY

The detrimental effects of rising CO_2 levels on the global climate have made carbon abatement technologies one of the most widely researched areas of recent times. A drawback of the benchmark aqueous amine process is that nearly 60% of the global emissions are from mobile or distributed sources. In this thesis, we first present a techno-economic analysis of a novel approach to directly capture CO_2 from air (Air Capture) using highly selective adsorbents. Our process modeling calculations suggest that the monetary cost of Air Capture can be reduced significantly by identifying adsorbents that have high capacities and optimum heats of adsorption. The search for the best performing material is not limited to Air Capture, but is generally applicable for any adsorption-based separation. Recently, a new class of nanoporous materials, Metal-Organic Frameworks (MOFs), have been widely studied using both experimental and computational techniques. In this thesis, we use a combined quantum chemistry and classical simulations approach to predict macroscopic properties of MOFs. Specifically, we describe a systematic procedure for developing classical force fields that accurately represent hydrocarbon interactions with the MIL-series of MOFs using Density Functional Theory (DFT) calculations. We show that this force field development technique is easily extended for screening a large number of complex open metal site MOFs for various olefin/paraffin separations. Finally, we demonstrate the capability of DFT for predicting MOF topologies by studying the effect of ligand functionalization during CuBTC synthesis. This thesis highlights the versatility and opportunities of using multiscale modeling approach that combines process modeling, classical simulations and quantum chemistry calculations to study nanoporous materials for adsorptive separations.

CHAPTER 1

INTRODUCTION

1.1. Nanoporous Materials

Porous materials have been widely used in the chemical industry for a variety of applications including separations, catalysis, sensing and gas storage. Porous materials are organic or inorganic frameworks that are commonly classified based on their pore size as macroporous (> 50 nm), mesoporous (2 - 50 nm) and microporous (< 2 nm). As the pore sizes associated with microporous materials is comparable to many common molecules, they are commonly referred to as nanoporous materials.[1] Due to their small pore sizes and narrow channels, these materials show interesting properties for a variety of separations and catalysis.[2]

Depending on the ordered or disordered nature of the underlying framework, nanoporous materials can be further classified as being amorphous or crystalline. For instance, amorphous materials like activated carbons do not have a well-defined crystal structure but have a distribution of pore sizes. In contrast, crystalline nanoporous materials such as zeolites, consist of a periodic and ordered structure that makes them amenable to computational modeling studies. In the past decade, another class of crystalline nanoporous materials, Metal-Organic Frameworks (MOFs) has attracted considerable attention by both experimental and computational research groups.[3] A brief overview of these materials is presented below.

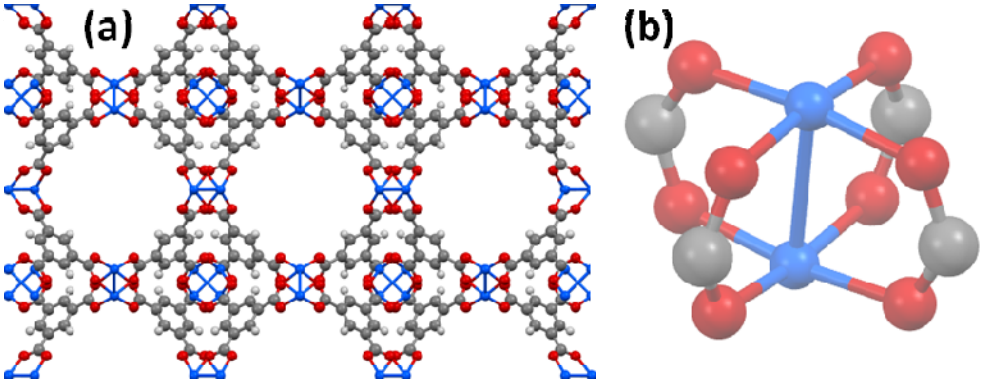

Figure 1.1 (a) Periodic structure of HKUST-1 and **(b)** the di-copper paddle wheel cluster with the Cu open metal site. The colors used are: oxygen (red), copper (blue), carbon (grey) and hydrogen (white).

1.2. Metal-Organic Frameworks

Metal-Organic Frameworks (MOFs) are 3-dimensional nanoporous materials comprising of metal centers that are interconnected via organic linkers to form an extended structure with permanent porosity. Since the early synthesis of a stable MOF framework more than a decade ago,[4] a huge body of computational and experimental research is now available in the literature. Combining the wide variety of available inorganic secondary building units (SBUs) with organic ligands of different connectivity, linker lengths and functionalities, MOFs provide a very versatile platform for many applications. Moreover, as MOF synthesis does not generally require the use of structure directing agents, thousands of structures have been experimentally reported.[5] Considerable work has been focused on tuning the properties of existing MOF structures using pre- and post-synthesis modifications[6-8] or via ligand exchange processes.[9] This relative ease of synthesis, coupled with the structural and functional tunability of properties, has made MOF research one of the fastest growing areas in synthetic chemistry.

An interesting property of some of the MOFs, which makes them potential candidates for separations, is the presence of coordinatively unsaturated metal centers.[10-12] Figure 1.1 (a) shows the atomistic representation of the well-studied HKUST-1 (also known as CuBTC). HKUST-1 consists of di-copper paddle wheel metal centers (Fig. 1.1 (b)) that the interconnected via 1,3,5-tricarboxylate ligands to form a periodic structure. During the solvothermal synthesis, these Cu metal sites are completely saturated with water molecules.[13] However, the bound water molecules can be removed by heating the sample to higher temperatures, leaving behind the under-coordinated Cu atoms. The activated form of HKUST-1 now consists of coordinatively unsaturated open metal sites that can interact with other guest molecules.[14] The ability to chemically bind to certain small molecules huge implications for sensing, separations and catalysis applications. Other examples of MOFs that exhibit open metal sites are PCN-16,[15] MIL-101[16] and the MOF-74[11] series. In addition to having open metal sites, other properties of MOFs that have attracted considerable research focus are flexibility,[17] tunability[18] and polymorphism.[19]

1.3. Multiscale Modeling

Given the huge diversity of available nanoporous materials, including MOFs and zeolites, it is a daunting challenge to identify high performing materials for a specific application. Even within MOFs, it is impractical to study the properties of each material and every possible variation using detailed experiments. Additionally, it is likely that only a handful of the studied candidate materials will be useful for the given application. Thus, a method of quickly and cheaply screening through a library of prospective materials is required. Computational molecular modeling and process simulation

approaches are ideally suited for this scenario and offer a very powerful tool towards accelerated materials discovery and process development. The strengths, the limitations and the utility of different modeling methods are presented below.

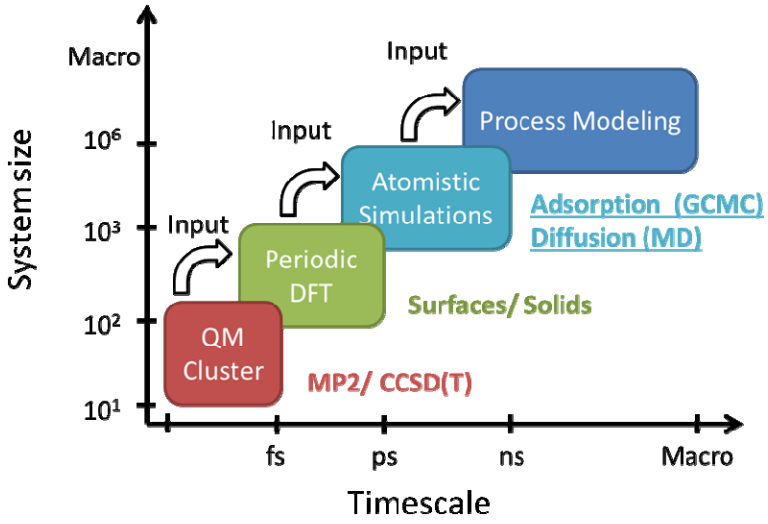

Figure 1.2 Hierarchy of molecular and process modeling methods.

1.4. Process Simulations

Figure 1.2 shows a simplified hierarchy of computational methods that are commonly used in molecular and process simulations. At the topmost level are process modeling techniques that describe macroscopic properties such as component flowrates, energy and mass balances, conversions etc. These methods are primarily used to analyze and optimize a technology at the process level. Consider a process that involves the adsorptive separation of two gases as an example. For this scenario, the process level description may include the adsorber bed operating in a cyclic pressure swing adsorption (PSA) process. Generally, macroscopic properties of the material such as adsorption isotherms and diffusivities of different components are inputs to a process model. The usefulness of process simulations lies in the ability to predict the overall performance of a

technology and to identify the essential properties of a material that maximizes the process performance.

1.5. Classical Atomistic Simulations

The next level of theory comprises of classical simulations that describes the interaction of individual gas molecules with the adsorbent framework at the atomic level. The intermolecular forces and interaction energies are represented by mathematical equations called force fields; and the macroscopic properties such as adsorption isotherms and diffusivities are obtained from statistical mechanics. In particular, Grand Canonical Monte Carlo (GCMC) is used to predict adsorption properties, while diffusivities are calculated from Molecular Dynamics (MD) simulations.[20] Typically, classical methods can be used to describe systems as large as 1 million atoms for a few nanoseconds of simulation time.

The accuracy of the GCMC and MD predicted properties are highly dependent on the quality of force fields used to describe the energetics of the system. Traditional or generic force fields are not transferrable and are found to be severely lacking in correctly describing the complex chemical environments in nanoporous materials. Moreover, force fields fitted to one set of experimental data are unable to predict adsorption in similar materials, rendering them unsuitable for material screening. For the atomistic simulations to be useful for screening applications, it is essential for the force field to have predictive capabilities.

1.6. Quantum Chemistry Methods

Quantum chemistry methods provide a better description of intermolecular interactions but are generally impractical to be directly used in the large scale GCMC or MD simulations required for calculating macroscopic properties. Within quantum mechanics (QM), different methods of varying computational cost and accuracies can be used for calculating various properties of the systems. Typically, highly accurate methods such as coupled cluster (eg. CCSD(T)) [21] and Moller-Plesset (eg. MP2) [26,70,128] can only be used for studying systems consisting of about 10 - 50 atoms. Moreover, these methods are only applicable for small representative clusters of the MOF and cannot be used for studying the periodic crystal structure of the framework.

A good compromise between accuracy and computational cost is provided by Density Functional Theory (DFT). Within DFT, the properties of the many-electron system is described by functionals that depend on the electron density. DFT has been widely used to study nanoporous materials, semi-conductors, bulk metals and surfaces.[22,23] In many cases, DFT provides a sufficiently accurate description of the intermolecular interactions for the adsorption systems of interest.[24]

1.7. Thesis Summary

The overall objective of this work is to study adsorption processes using the different computational methods outlined above. In Chapter 2, we discuss a novel technology for directly capturing CO_2 from air using process simulation methods. This study presents the first techno-economic analysis of an adsorption based air capture technology and concludes that further detailed analysis of this process is justified.

We turn from the process simulation approach of Chapter 2 to using molecular modeling methods to study nanoporous materials. In Chapter 3, we show that generic force field based methods are unsatisfactory for predicting adsorption isotherms of alkanes in MIL-47(V). We use a combined classical and quantum chemistry based approach to systematically develop force fields based on DFT calculations. Our results show that DFT-derived force fields give good predictions of macroscopic properties in MIL-47(V), and can be further used to study the flexible MIL-53 series.

These methods are extended to derive force fields for olefin and paraffin interactions with more complex open metal site MOFs in Chapter 4. In particular, we use periodic DFT calculations to develop force fields for modeling adsorption in HKUST-1. These force fields are then used for screening similar MOFs for olefin/paraffin separations at the process level.

In Chapter 5, we use a quantum chemistry approach to predict the crystal topology of HKUST-1 derivatives for different functionalized ligands. This study illustrates the versatility of DFT calculations for predicting the crystal structures of MOFs using periodic and cluster calculations.

Finally, we outline and discuss the main challenges and opportunities of molecular simulations for studying nanoporous materials in Chapter 6. This study provides a framework for understanding the different aspects of adsorption processes using a multiscale computational approach.

CHAPTER 2

ANALYSIS OF EQUILIBRIUM-BASED TEMPERATURE SWING ADSORPTION PROCESSES FOR DIRECT CAPTURE OF CO_2 FROM AIR [a]

In this chapter, we present a techno-economic analysis of an equilibrium based temperature swing adsorption (TSA) process for direct capture of CO_2 from air. By using a well-defined model that describes the adsorbent, the contactor and the adsorption process, we are able to estimate the performance of our Air Capture process using CO_2 purity and product throughput as metrics for comparison. Using the total energy requirement of the process and available sources of energy, such as steam and electricity, we perform an economic analysis to obtain a net operating cost for this process. Finally, we identify possible strategies for reducing the monetary cost and conclude that further analysis of adsorption-based Air Capture processes is justified.

2.1. Introduction and Literature Review

The growing levels of CO_2 in the atmosphere and their possible detrimental effect on the global climate have made carbon management technologies one of the most

---

[a] Portions of this chapter were adapted from A.R. Kulkarni and D. S. Sholl, Analysis of Equilibrium based TSA processes for direct capture of CO_2 from air, Ind. Eng. Chem. Res., 2012, 51 (25), pp 8631-864.

widely researched areas of recent times. The current CO_2 level in the atmosphere is 379 ppm.[25] One benchmark technology for reducing CO_2 emissions is using aqueous solutions of amines to capture CO_2 from post combustion flue gas. Other strategies available for capture of CO_2 from flue gas using absorption and adsorption have recently been reviewed.[26] Point sources like large coal-fired power plants typically account only for about 1/3 of the anthropogenic CO_2 released to the atmosphere[27] while, much of the remaining 2/3 is due to transportation, small power plants and chemical industries. Under the reasonable assumption that fossil fuels are going to continue to be the predominant source of global energy in the near future, no commercial carbon capture technology currently exists that can be used to offset CO_2 emissions from this two thirds of total emissions. If deep reductions in global CO_2 emissions are to be achieved, a broad range of technology and policy options need to be explored.

Direct capture of CO_2 from air, which we will refer to below as Air Capture, is one technology that has the potential for capturing CO_2 emissions from all possible sources. Air capture aims to make use of the concepts and technologies developed for CO_2 capture from flue gas capture and apply them to capture CO_2 from ultra-dilute concentrations in air. There has been far less work performed on air capture than on flue gas capture, but the economic and technical feasibility of air capture has been intensely debated.[28-30]

The first discussions of air capture as a technology to address rising atmospheric CO_2 levels was presented by Lackner in 1999 and 2001.[31,32] In 2004, a process was suggested that used sodium hydroxide solution to absorb CO_2 from air and convert it into soluble sodium carbonate, which was precipitated using quicklime and calcined at 900 °C

to recover CO_2.[33] A recent report on the feasibility of air capture by the American Physical Society (APS) focused exclusively on this sodium hydroxide based process, and estimated the cost of using this technology to be close to \$600 /tCO_2.[30] Concluding that air capture is economically infeasible based purely on the APS report is incorrect, as the report showed only that a particular process for air capture based on sodium hydroxide is highly unattractive. Based on an empirical analysis of processes *similar* to air capture, a recent report by House et al.[28] concluded that the cost of air capture systems exceeds ~ \$1000/tCO_2. As we will show below, we believe that constraints on the processes considered by led to cost estimates that are considerably too high.

The idea of an adsorption process for capture of CO_2 from air was first suggested by Lackner and Brennan[34] using a humidity swing with an ion exchange resin. A limitation of this initial report was that the details of an actual process or a device that would be used were not described by the authors.

Other adsorbents that been demonstrated as candidates for use in adsorption-based air capture include the hyperbranched amino silica materials described Jones and co-workers[35,36] and TRI-PE-MCM-41 class of adsorbents of Sayari and co-workers.[37] The heat of adsorption for CO_2 ranges between 50 kJ/mol and 118 kJ/mol for these amine functionalized materials.[38] Previous research relevant to adsorption based air capture has primarily focused on increasing the amine loading of the adsorbent to improve CO_2 adsorption capacity under ultra-dilute conditions.[37,39-42] These and other studies have reported high initial uptake rates for CO_2[40,43], enhancement of CO_2 adsorption at low values of relative humidity[37,39,40,44-46] and good stability of the adsorbent after multiple regeneration cycles. [38,40,45,47,48] Other amine-based sorbents have also been reported with

significant CO_2 uptake at concentrations relevant to ambient air.[49] Wurzbacher et al.[47] have demonstrated lab scale extraction of CO_2 from dry and humid air by using a temperature vacuum swing adsorption process. A packed bed of diamine-functionalized silica gel beads was used to study the effect of parameters such as adsorption time, desorption temperature and desorption pressure on the cyclic adsorption capacity. The same group has reported a higher cyclic capacity of 0.69 mmolCO_2/g using an amine-functionalized nanofibrillated cellulose as the adsorbent. [38]

Although the studies listed above have reported useful physical data for considering adsorbents for air capture, no study has yet examined a process-level description of using these materials. Modeling of air capture at this level is critical to determining whether specific processes are worth additional development and identifying the factors that limit the performance of a material or process. The key contribution of the APS report[30] on the sodium hydroxide process was to approach air capture from this process level. The aim of this chapter is to describe process-level models of adsorption-based air capture of CO_2 with a specific adsorbent, TRI-PE-MCM-41. We examine a number of related processes based on temperature swing adsorption (TSA), using product purity and throughput as a metric for comparison. For a specific contactor configuration, we calculate the mechanical and thermal energy requirement for each individual step of the air capture process and suggest possible strategies for reducing the energy requirements. We examine what kinds of cyclic processes can be used to enhance the purity and volume of CO_2 that is captured, and provide initial operating cost estimates for these processes. Our results show that the estimated operating cost of capturing CO_2 from air using adsorption processes to be ~\$100/tCO_2 in terms of net CO_2 capture. This

preliminary study indicates that more detailed analysis of the technological and economic feasibility of adsorption based air capture processes is worthwhile.

The chapter is organized as follows. The process model and the assumptions involved are described in Section 2.2, which is followed by the methodology used for estimating energy requirements (Section 2.3). The process performance is evaluated in terms of the product throughput, energy cost and monetary costs in Section 2.4. Finally, in Section 2.5 we discuss potential avenues to reduce the costs of adsorption-based air capture.

2.2. Process Model Description

2.2.1. Temperature driving forces

Since the performance of the air capture process will depend considerably on the climate at a given location, we choose six US locations based on their proximity to ongoing geologic sequestration experiments.[50] The locations and a summary of the temperature data for each location from the National Climatic Data Center (NCDC)[51] is presented in Table A1 (Appendix A). In this case, the temperature driving force for desorption is provided by using low pressure steam at 105–120 °C that is available as waste heat from chemical and manufacturing facilities.[27,52] In estimating operating costs for TSA processes using steam desorption below, we compare scenarios in which steam is available for free from waste heat sources and where steam must be generated specifically for the air capture process. The calculations for different locations were performed for an entire calendar year and the results were scaled using 330 operating

days/year as a basis. The daily CO_2 throughput was obtained by considering 365 days in a year.

2.2.2. Adsorption processes

The adsorption processes considered below are modifications of a simple equilibrium based TSA cycle. Briefly, adsorption of ambient air occurs at a lower temperature, T_1, and ambient pressure and desorption and product recovery occurs at a higher temperature, T_2, and a slightly lower pressure. As the heat of adsorption and the uptake of CO_2 are higher than that of N_2, the product contains more CO_2 than ambient air. A dominant factor in the performance of the cycle is the magnitude of the temperature swing, $T_2 - T_1$. Higher temperature swings yield better performance both in terms of CO_2 purity in the product and the total moles of product

A schematic of process is presented in Figure A2 (Appendix A). The process is initiated with the system at equilibrium at the lowest temperature of the first day (January 1 unless otherwise mentioned). This is shown as stage 0 at the start of the cycle, where the system consists of a solid adsorbent phase that is in equilibrium with the gas phase at temperature T_{eq}. The process then proceeds through the following steps.

Step 1: The gas phase from the previous stage is discarded and fresh air at temperature T_1 is flowed through the contactor (using wind or fans, if required) until the adsorbent is in equilibrium with air and the contactor is then closed.

Step 2: A pre-determined fraction (90% unless otherwise specified) of the gas phase, α, is removed while the temperature is kept constant at T_1. We assume that the gas phase is removed rapidly such that the composition of the adsorbed phase does not change. The adsorbent and remaining gas phase now contain more CO_2 than ambient air.

Step 3: When a fraction of the gas phase has been removed as waste at the lower temperature, steam is introduced to desorb the CO_2 and N_2. It is assumed that steam at 110 ºC is passed through the adsorbent continuously until a fixed fraction (usually 90%) of the adsorbed phase components is recovered as product. The continuous flow of steam results in almost zero CO_2 partial pressure in the gas phase, allowing for high recoveries. It may be possible that small amounts of CO_2 (close to those of ambient air) are present in steam, depending on its source. The continuous flow of steam ensures that the CO_2 partial pressure at the surface does not increase because of desorption, but instead remains constant at the low inlet concentration.

Step 4: The water gas and product mixture is cooled sufficiently to condense out the water and the process is then repeated. After the separation of water and CO_2 at ambient pressures, purified CO_2 is obtained as the product from the process. This gaseous product will be saturated with water vapor, as is the case for CO_2 exiting most large-scale CO_2 capture technologies such as aqueous amine absorption.

2.2.3. Contactor

To make even approximate estimates of the cost for operating the processes of interest, we must specify the form of the contactor containing the adsorbent. One approach is to use monoliths consisting of numerous parallel channels that are coated with the adsorbent. [53] The length of the monolith must be sufficiently long to adsorb a reasonable fraction of CO_2 from air. On the other hand, the mechanical costs associated with flowing significant quantities of air require that the pressure drop across the contactor be as low as possible. Based on a preliminary analysis of various contactor parameters (coating thickness, channel diameter, monolith wall thickness and contractor

length), a monolith configuration was chosen and the parameters are listed in Table 2.1. We assume cordierite as the material of construction, as it is a common choice for ceramic monoliths. [51,54] Our choice of contactor configuration is practically realizable as cordierite monoliths with similar wall thicknesses (2 mils / 3 mils) and higher cell density (900/600 cpsi) are commercially available. [51]

The surface area and volumes associated with a single monolith block[51] are too small to have significant removal rate of CO_2 and larger units comprised of many individual monoliths will be necessary for practical applications. For ease of manufacturing and transportation, we assume that dimensions of a commercial air capture unit will be smaller than a standard shipping container (2.4×2.4×12.0 m). Specifically, each unit is designed to consist of 20 contactor-modules, each 2.24×2.24×0.5 m with a combined volume of 50 m^3 per unit. Each module has a length of 0.5 m and an exposed surface area of 5 m^2, and the flow of air occurs over the smallest dimension of the module. All the results presented later are with respect to a 50 m^3 air capture unit.

Table 2.1 Details of the monolithic contactor used in this study

Parameters	Value
Physical dimensions (m)	2.24 × 2.24 × 0.5
Channel density (cells per sq. inch)	100
Channel internal dimensions (mm)	2.47 × 2.47
Density of monolith material (Cordierite), ρ_m (kg/m^3)	2600
Monolith wall thickness (mils)	2.86 [a]
Internal surface area (m^2/m^3)	1530
Adsorbent coating thickness (microns)	100
Adsorbent density, ρ_a (kg/m^3)	1000
Adsorbent loading (kg/m^3)	146.8
Empty volume	79.6 %
Pressure drop (Pa)	100 Pa
M_a / M_m [a]	1

[a] chosen to ensure equal mass of the adsorbent and bulk monolith, M_a: Mass of adsorbent, M_m: mass of monolith

2.2.4. Adsorbent

Due to the dilute concentrations of CO_2 in air, an ideal adsorbent needs to have high adsorption capacity and high selectivity for CO_2 at ambient conditions. The adsorbent used in our calculations is amine functionalized silica, TRI-PE-MCM-41, developed by Sayari and co-workers.[55,56] The adsorption of CO_2 is explained by two independent adsorption mechanisms – chemisorption by the amine groups and

physisorption by the bare silica surface.[57] The experimental adsorption isotherm for CO_2 [57] and N_2 [58] is modeled by the Toth equation.

2.2.5. Assumptions

To make our calculations feasible using physical data that is currently available, a number of assumptions are required. An important assumption is that the air entering the process contains only N_2 and CO_2 *under dry conditions*. This assumption is driven by the lack of available isotherm data for humid gases for amine-functionalized silica adsorbents. We are *not* advocating that air be dried before entering an air capture unit, as this would likely be economically infeasible and technically disadvantageous. Nevertheless, studying models based on dry air is a reasonable initial approach because the presence of water vapor typically enhances the CO_2 selectivity and capacity of amine-functionalized adsorbents. [37,39,44-47,59] For TRI-PE-MCM-41, the CO_2 uptake has been shown to be higher in the presence of humidity for 5% CO_2/N_2 mixtures.[59] More recently, enhancement of CO_2 uptake has been reported for fused silica impregnated with polyethylenimine at air capture conditions.[41]

When steam is used as a purge, we assume that the presence of water does not have an effect on the adsorption isotherm of CO_2. In this case, steam maintains a low partial pressure in the gas phase during desorption and provides a thermal driving force for desorption. When steam comes in contact with the monolith, the heat of condensation of steam is utilized for desorption of the adsorbates. A portion of the available thermal energy is also used to raise the temperature of the adsorbent and the monolith to the desorption temperature. Additionally, stability of functionalized silica adsorbents in steam has been shown to depend on the nature of the silica support and the operating

conditions.[60] Our work implicitly assumes that the presence of low pressure steam does not cause significant degradation of the adsorbent.

As the processes we consider use ambient temperatures as all or part of the driving force, the cycle half times of the individual cycles are of the order of a few hours. On this timescale, heat and mass transfer restrictions are assumed to be negligible. We assume that the time scale for attaining local equilibrium is much smaller than the half-cycle time of the adsorption cycle. This appears to be reasonable when compared to earlier studies that have shown that the adsorption of CO_2 on amines is relatively fast, especially in the presence of water. [39,41,43,58] Similarly, we assumed that the gas phase can be removed rapidly such that the composition of the adsorbed phase remains unaffected. These assumptions imply that three distinct timescales exist, namely (in increasing order), withdrawal of gas phase by external pumps, achievement of local equilibrium with the gas phase, and half-cycle time of the process.

2.3. Estimation of Energy Requirements

To judge how viable the above processes would be in relation to other approaches, it is critical to examine the costs associated with their operation. In this section, we outline the methodology used in estimating the energy requirements for these processes. These estimates are not intended to provide the fidelity that could be achieved in a detailed economic analysis; rather, they provide guidelines for deciding whether future detailed analysis is warranted.

The concentration of CO_2 in air is ~400 ppm, which is equivalent to 16.6 mmol CO_2/m^3 of air. Because of this dilute concentration, a large quantity of air must be flowed through the contactor to adsorb a significant amount of CO_2. The pressure drop across a

contactor depends on the average velocity of air and on the physical parameters of the contactor. Higher velocities lead to a higher gas side mass transfer coefficient but a smaller residence time for the monolith, changing the equilibration time during adsorption. Higher velocities also cause a larger pressure drop and increase the energy requirement for blowers. Accurate calculation of the equilibration time and associated breakthrough curves requires models of significant complexity. These calculations are well established but a significant hurdle in performing calculations of this kind is the lack of experimental data for various rate processes.

Instead of attempting detailed calculations of this type, we use the approach suggested by the recent APS report.[30] The authors defined a characteristic length of the adsorbent, L_0, which defines the capture fraction, $\alpha_{capture}$, for the system. The capture fraction is defined as the fraction of CO_2 that is adsorbed by the contactor from air during the adsorption stage. The characteristic length is defined as

$$L_0 = \eta U d^2 / D \qquad (2.1)$$

$$\alpha_{capture} = 1 - \exp(-L / L_0) \qquad (2.2)$$

where, U is the average velocity in the monolith channels, L is the length over which the air flow occurs, D is the gas phase diffusivity of CO_2, and η is a parameter whose value depends the rate of removal of CO_2 at the surface. For the ideal case of instantaneous adsorption at the wall, η is 0.068. [30] Allowing for the possible limitations associated with dynamics of the system, we assumed a value of η that is 25 times larger than the ideal case. The parameters used in the energy calculations are listed in Table 2.2.

Table 2.2 Physical properties of the vapor phase and the contactor material used in this study.

Parameters	Value
Kinematic viscosity, ν (m^2/s)	1.5×10^{-5} [a]
Diffusivity, D (m^2/s)	2.1×10^{-5} [a]
Equivalent diameter, d (mm)	2.27 [b]
Density of air, ρ (kg/m^3)	1.2 [a]
Heat capacity of adsorbent, Cp_a (J/gºC)	1
Heat capacity of monolith material, Cp_m (J/gºC)	1.4
η	1.7 [a]
Schmidt number, Sc	0.71

[a] values obtained from ref [30], [b] for 100 micron adsorbent coating

The mechanical energy for air flow depends directly on the pressure drop across the system. The velocity through each monolith channel was calculated by assuming laminar flow as [61]

$$U = \frac{P_{drop} d^2}{32 \rho L \nu} \qquad (2.3)$$

where, P_{drop} is the pressure drop across the length L. The power required is the product of the volumetric flow rate and the pressure drop. The total energy required for air flow will depend on the duration of time for which air flows through each contactor, t_{ads}. This time is estimated by calculating the average CO_2 uptake required by the adsorbent to achieve equilibrium with air for every adsorption-desorption cycle.

The second component of mechanical energy that needs to be included is the electrical energy required for withdrawal of gases from the monolith using a vacuum

pump. A bound can be placed on the cost of the partial vacuum based on the energy required for compression of gas from the vacuum to ambient pressure. The minimal amount of energy is required when an isothermal reversible process is used and is given by $W = nRT\ln(P_1 / P_2)$ where, P_1 and P_2 are the initial and final pressures, respectively. Because of the time scales associated with the vacuum pump, we assumed an irreversible process for our calculations. The energy required for reducing the pressure inside the monolith from P_1 to P_2 and irreversibly compressing the withdrawn gases to fixed external pressure, P_{ext} (1 bar), is given by

$$W = -P_{ext} \times V\left[\frac{P_1}{P_{ext}} - \frac{P_2}{P_{ext}} + \ln\left(\frac{P_2}{P_1}\right)\right] \qquad (2.4)$$

The energy costs described above yield a CO_2-enriched product exiting the process at a relatively low pressure. Finally, it is useful to also consider the additional compression cost that would be associated with compressing the product to CO_2 pipeline ready pressures (specifically, 14 MPa). The thermodynamic analysis presented by House et al.[62] was used to estimate this contribution. Considered together, the mechanical energy calculations include the energy required for flowing air through the monolith, E_f, for removal of waste and products by application of partial vacuum, E_v and for compression of the product stream, E_c. For all mechanical energy requirements (blower, vacuum pump and compressor), an overall efficiency of 80% was assumed.

The calculation of the thermal energy component is more straightforward. The minimum energy required for regeneration of the adsorbent is calculated using the heat of adsorption of CO_2 and N_2. This quantity depends only on the adsorbent characteristics and not on the capture process. For the diurnal process, the thermal energy for desorption

is provided by the ambient surroundings and does not require external energy inputs. The actual thermal energy for desorption of CO_2 will depend on the relative contribution of physisorption and chemisorption component. An upper bound for thermal energy is obtained by using heat of chemisorption of CO_2. If pure CO_2 is obtained as the product, the minimum energy required for desorption is ~1530 MJ/tCO_2 for the chosen adsorbent. This by itself, is higher than the reported thermal energy input of ~ 1100 MJ/tCO_2 for the humidity swing air capture process of Lackner et al [34].

When steam desorption is used, it is unlikely that all the steam supplied will be used only for desorption. Though it is undesirable, a part of this energy will be used for the sensible heating requirements of the bulk monolith and will depend on the material of construction employed. The energy associated with the sensible heat requirements for the adsorbent, E_{ta}, and the monolith, E_{tm}, can then be calculated as,

$$E_{ta} = M_a C_{pa} \Delta T \tag{2.5}$$

and

$$E_{ta} = M_a C_{pa} \Delta T \tag{2.6}$$

where, M_a and M_m are the masses and C_{pa} and C_{pm} are the specific heats of the adsorbent and the monolith, respectively. Unlike the thermal energy for desorption, the sensible heat requirements for the monolith represent a parasitic loss, as they do not scale favorably with the throughput of CO_2 obtained as the product. During the regeneration step, it is not necessary to raise the temperature of the entire monolith to the desorption temperature; the only requirement for steam flow being that sufficient amount of CO_2 has been desorbed. Practically, the amount of the thermal energy utilized as sensible heat will depend on the relative rate of desorption of CO_2 and the thermal conductivity of the

monolith material. By considering the entire mass of the monolith for the sensible heat, we obtain an upper bound for the parasitic losses associated with the process.

Our energy calculations assume that the pressure at the inlet of the process is close to ambient conditions, implying that the energy required for the pressurization of air is smaller than E_f. For processes that require higher inlet pressures for operation, the energy required for air pressurization may be significant. Our process involves continuous flow of steam through the monolith, causing some water to remain condensed in the channels. In reality, the cost of product recovery will also involve the mechanical energy associated with the flow of this two phase mixture of steam and condensed water. This aspect has not been included in the energy estimates that follow. We have not accounted for energy requirements or possibilities of heat recovery in the separation of the resulting CO_2-steam mixture via condensation, under the assumption that this process will typically be straightforward using cooling from ambient conditions. Because of these assumptions, our energy estimates for the total energy requirements of the process are lower bounds.

Figure 2.1 Schematic of the air capture process used for the calculation of minimum work

For each of the scenarios examined, it is useful to compare the energy required for the real process to the theoretical minimum work required for the same separation by a completely reversible process. The process outlined in Figure 1 is an isobaric and

isothermal separation of ambient air into two streams, with stream 3 being the purified product. Assuming ideal gas mixtures, the minimum work required per mole CO_2 captured is

$$W_{\min} = -RT\left[\frac{n_1}{n_3}\left(y_1^{CO_2}\ln y_1^{CO_2} + y_1^{N_2}\ln y_1^{N_2}\right) - \frac{n_2}{n_3}\left(y_2^{CO_2}\ln y_2^{CO_2} + y_2^{N_2}\ln y_2^{N_2}\right) - \left(y_3^{CO_2}\ln y_3^{CO_2} + y_3^{N_2}\ln y_3^{N_2}\right)\right]$$

(2.7)

where, n_i is the total number of moles and y_i, the compositions of the various streams. For a given temperature, the minimum work is only a function of the purity of the product obtained, $y_3^{CO_2}$ and the process throughput, n_3/n_1 .

2.4. Process Performance

Initially, calculations were performed for a single contactor-module with the adsorbent coating thickness of 100 microns. In each scenario examined, the purity of CO_2 obtained at the end of process and the total amount of product gas obtained per unit (50 m^3 volume) per year (tons CO_2 $unit^{-1}$ $year^{-1}$) were used as metrics for the process performance.

2.4.1. Product purity and throughput

Figure 2.2 (a) shows the annual variations of temperature for two locations, FL and UT. Calculations were performed for each day, with adsorption being carried out at the lower temperature and desorption using purge steam. Fig. 2.2 (b) shows a strong correlation between the adsorption temperature and the working capacity of the process. The average working capacity for FL (0.87 mmol/g) is lower than the UT value (1.12 mmol/g). The better performance in UT is because the average adsorption temperature at

UT (5.5 ºC) is almost 10 ºC lower than that at FL (16.3 ºC). This also implies that the uptake rate of CO_2 may be slower in UT than FL. Average purities of ~ 88% and daily recoveries of 250 – 320 $kgCO_2$ are predicted for one desorption step per day for the various locations (Table 2.3).

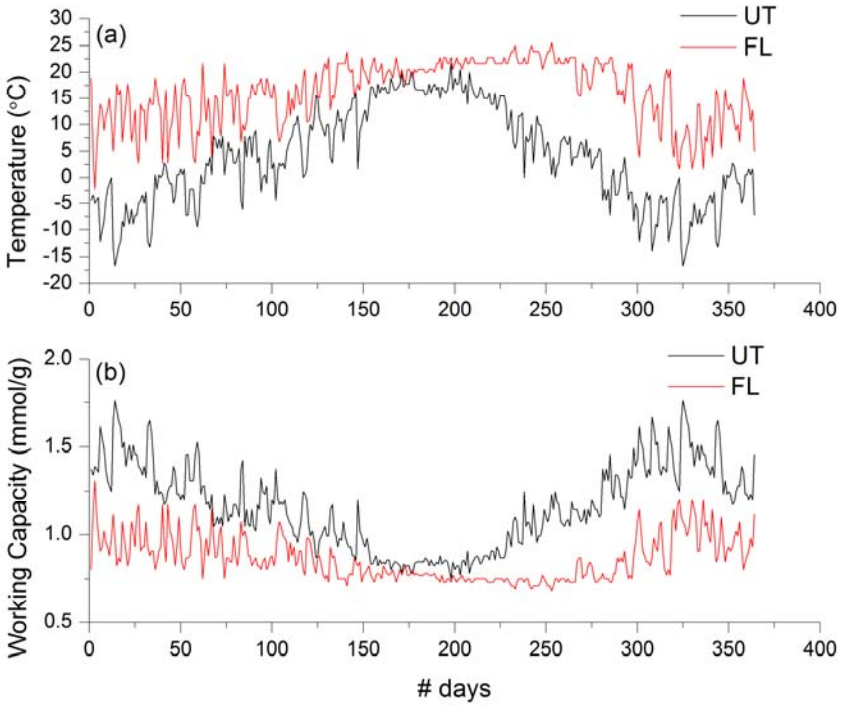

Figure 2.2 (a) variations of ambient temperature and **(b)** working capacity for UT (black) and FL (red). The desorption temperature is fixed at 90 ºC for all locations.

For a pressure drop of 100 Pa across the contactor, the characteristic length, L_0 is calculated as 74.2 cm. Using Eq. 2.2, this give an overall capture fraction of 49 %. Table 2.3 shows that the average adsorption time, t_{ads}, is less than 2 hours for the six chosen locations. The performance of the process can be improved by repeating both adsorption and desorption steps, multiple times a day. For air capture conditions, faster desorption

half cycles have been reported for TSA process using air at 85 ºC as the purge, [41] though the oxidative stability of materials at these conditions is unclear. [63]

Table 2.3 Process performance at different locations for one adsorption-desorption cycle per day.

Location	t_{ads} [a] (min)	Purity CO_2 (percent)	CO_2 throughput (tCO_2 $unit^{-1}$ $year^{-1}$)	Product throughput (t-product $unit^{-1}$ $year^{-1}$)
FL	91.3	88.7	92.0	103.8
AL	101.5	88.6	104.1	117.5
UT	113.9	88.5	119.4	135.0
GA	103.0	88.6	106.1	119.8
WA	111.4	88.5	116.5	131.5
TX	104.4	88.6	107.8	121.7

[a] t_{ads} calculated for a pressure drop of 100 Pa.

The combination of both temperature and concentration driving force for desorption would ensure that the time required for desorption step will be significantly lower than $t_{ads.}$ Thus, the minimum cycle time used is set at four hours (i.e. six cycles per day) to ensure that the total time for each case is at least two times t_{ads}. We find that the product purity remains almost constant at approximately 88.5 % for all the locations on using more cycles. The total amount of CO_2 recovered, however, increases almost linearly with the number of daily cycles. Allowing for considerable margin of error in the calculation of adsorption times and possibly slower uptake rates at lower temperatures, a total cycle time of six hours is used. For four cycles per day, this version of the process produces > 400 tCO_2 per unit per year with an average purity of 88.5 %.

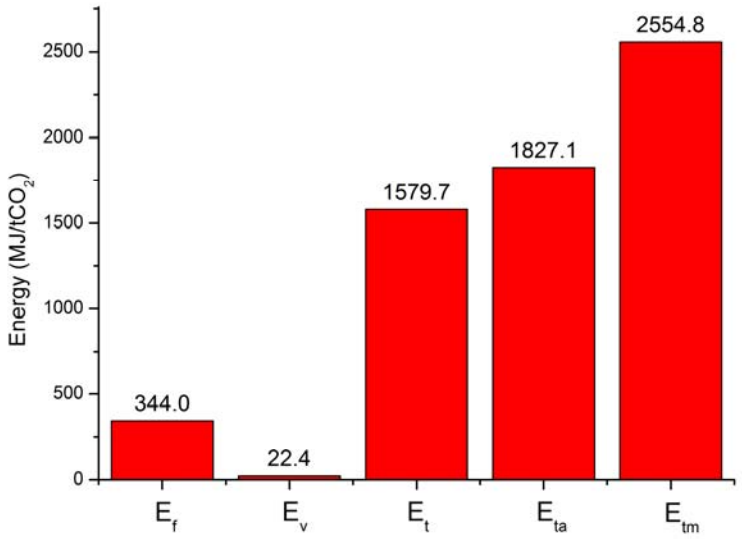

Figure 2.3 Energy requirements of the process for four cycles per day at the UT location. Energy required for air flow, E_f, is calculated for a pressure drop of 100 Pa across the contactor.

2.4.2. Energy Cost

We now consider the energy associated with operating the TSA process. When four cycles per day are used, 1.1 tCO_2/day is obtained at a purity of 88.5%. The energy requirements for this case are shown in Figure 2.3. The total energy required is 6328 MJ/tCO_2 and is dominated by the thermal energy requirements ($E_t + E_{ta} + E_{tm}$) of the system. As noted earlier, this thermal energy is provided by the condensation of steam inside the monolith channels. The energy required for desorption, E_t, is 1580 MJ/tCO_2, which compares favorably with the theoretical minimum for 100 % CO_2. This energy scales with the amount of CO_2 desorbed and can (in principle) be reduced on a per tCO_2 basis by using an adsorbent with a lower heat of adsorption if other properties of the adsorbent are unchanged. For the chosen contactor configuration, the 40.4 % (28.9 %) of the total energy is associated with the sensible energy requirement of the monolith (adsorbent). Together, these parasitic losses are responsible for approximately 70% of the

total energy requirements. In contrast, the electrical energy associated with flowing air through the contactor is ~5.4 % of the total energy at a pressure drop of 100 Pa. Thus, even though the low concentration of CO_2 in air requires flow of considerable amount of air through the contactor, the energy required for this does not necessarily dominate the energy cost. Instead, the most critical energy cost is incurred regeneration of the adsorbent, specifically in cyclic heating of the bulk monolith that does not directly contribute to the CO_2 throughput. The sensitivity of the various process parameters and possible options for reducing the parasitic losses are explored later in Section 2.4.

At this stage it is useful to consider the second law efficiency of the overall process. From Eq. 7, the minimum work calculated for an air capture process with 49% CO_2 capture and final product purity of 88.5% (at 1 bar) is 466 MJ/tCO_2 (or 20.5 kJ/molCO_2). When compared to the total energy requirement, the overall second law efficiency of the process is 7.4%. Our analysis of energy requirement is based on simplistic model and gives a reasonable lower bound for the process; a detailed analysis will predict higher energy requirements and lower second law efficiencies. Nonetheless, we will show later in Section 4.3 that it is possible to improve the thermodynamic efficiency of the process (~ 11%) by using a better contactor configuration and higher working capacities.

It is important to compare our results with the analysis of House et al.[28], which considered design of air capture processes based on existing gas purification methods. House et al. predicted the efficiency of air capture to be less than 5%. The thermodynamics and the optimal second law efficiency for the industrial processes considered by the authors (flue gas capture, N_2/O_2 separation, ethanol distillation), are

constrained by downstream process requirements such as flow rate, conversion, removal fraction etc. Such constraints are not directly applicable to air capture, so the optimal second law efficiencies are not determined by identical process economics. Our thermodynamic analysis is based in part on the observation that adsorption is a spontaneous process (it requires no energy input). After this spontaneous adsorption step, the system is no longer dilute with regards to CO_2, and a higher thermodynamic efficiency for the energy intensive desorption step is possible than is seen in the analysis of House et al.. Both these factors are addressed again in Section 5.

As the throughput obtained by this process is of the order of hundreds of kilograms of CO_2 per day per unit, it is useful calculating the energy, E_c, required for compressing the product CO_2 to sequestration ready pressures. A compression energy requirement of ~ 13 kJ/mol-gas, [62] is used for this calculation. Using the value of purity obtained earlier and assuming no further concentration of the CO_2 stream, the energy for compression, 417 MJ/tCO_2, is comparable with the energy for air flow (344 MJ/tCO_2) and represents ~ 55% of the overall electricity cost. It is important to note that compression costs are also present in any process that removes CO_2 from concentrated point sources such as power plant flue gases. The analysis presented above, four cycles per day, is used as a reference scenario for the remainder of this work.

2.4.3. Monetary Cost

In the previous section, we have described a plausible process that can capture ~ 1.2 tons of CO_2/day at 88.5 % purity, and requires 5962 MJ/tCO_2 from steam and 784 MJ/tCO_2 of mechanical energy from electricity. Depending on the energy source used, we must account for CO_2 that would have been emitted back to the atmosphere for

powering the process. In this section we aim to estimate the monetary cost for net CO_2 capture. We only estimate operational costs, and have not attempted to estimate capital expenditures and maintenance costs.

Instead of using an average cost of electric power, we follow methodology similar to House et al. [28]. In their analysis, the authors calculated the cost of air capture for various sources of electricity, accounting for differences in the cost and CO_2 emission factors among these sources. Assuming electricity as the only source of energy, the authors predicted air capture costs > \$1000/tCO_2 without the energy required for compression of capture CO_2 to pipeline specifications.

Table 2.4 Comparison of emission factors for steam and electricity generation

Type of energy	Reported value [a]	Unit	Value (MJ/tCO_2)
Steam generation	88.18 [65]	kgCO_2/MMBtu	11964.8
Avoided emissions from sale of steam	79.71 [65]	kgCO_2/MMBtu	13236.2
Electric power generation (US average)	0.676 [64]	tCO_2/MWh	5325.4

[a] valid for reporting years 2003 and later

The total electricity required is only 5.4 % of the total energy requirements. When the energy for compression is included, this number increases to a little over 11 %. The US Energy Information Administration has reported the CO_2 emission factor for electric power generation of 0.676 tCO_2/MWh.[64] The same study suggested CO_2 emission factors to be used for steam generation of 88.18 kgCO_2/MMBtu, [65] and for calculation of avoided emissions from energy sales as 79.71 kgCO_2/MMBtu. [65] This data is summarized in Table 2.4 using consistent units. A key observation here is that for every ton of CO_2 released, twice as much energy can be obtained from using steam than from using electricity. Equivalently, for the same amount of energy used, the emissions caused by using steam are almost a factor of two lower than electricity. It should be also noted that

the suggested emission factor for avoided emissions due to purchased steam is more favorable than for steam generation.

The dollar cost and the CO_2 intensities for different sources of electricity analyzed by House et al.[28] and the corresponding values for using steam are summarized in Appendix A. The monetary costs for electricity have been updated from a recent report by the US Energy Information Administration[66] and differ slightly from House et al.[28]. An important observation is that the cost of steam, \$15.2/MWh[67] is significantly lower than electricity.

We have considered four different cases for calculation of cost based on the availability of steam, which are described below

Scenario I (No Steam): All the energy required for the process is provided by electricity. Even though it is impractical to assume that the energy for desorption and sensible heating of the monolith is provided by electricity, this analysis is consistent with the method of House et al. [28]. In this case, we assume no loss of electrical power while supplying the thermal energy to the system.

Scenario II (Dedicated Steam): This is a more realistic scenario in which all the steam required by the process is obtained by production of low pressure (LP) steam dedicated for the air capture process. The cost of steam and the emission factor is obtained from Table A2. The energy for the blowers and pump is provided by electricity.

Scenario III (Purchased Steam): In this scenario we assume that a source of LP steam is present in the vicinity of the air capture process and this steam is purchased and used for performing the air capture process. The cost of steam and the CO_2 capture fractions are again considered in the calculation of net CO_2 capture cost.

Scenario IV (Waste Steam): This scenario is very similar to Scenario III in the sense that all the steam requirements of the process are provided by the same nearby source. The difference is that we assume that unless the air capture plant were to use the LP steam, it would be entirely wasted at the source. Thus, because of the presence of the air capture plant all the CO_2 emissions caused due to the generation of LP steam are avoided. For the calculations, the CO_2 emission factor for steam was set to zero to replicate the avoided emissions.

Realistically, the analysis of the actual process will be a combination of Scenarios II, III and IV depending on the extent of availability of steam from other sources. The range of values defined by these scenarios should be a reasonable estimate of the monetary cost.

The estimation of monetary costs for the TSA process with four cycles per day in UT is shown in Table 2.5. The values for Scenario I are significantly higher than the other cases and range from \$160 - \$500/tCO_2-captured. This is not surprising since, 1) the CO_2 emission factor is unfavorable for electricity relative to steam and 2) the cost of electricity is higher than for steam. For scenario I the optimum source of electricity becomes a trade-off between having the most favorable emission factor and having the lowest cost per kWh. The minimum cost obtained is using hydroelectric power. This analysis is consistent with previous work,[28] but is unrealistic for processes based on adsorption-regeneration as is it is undesirable to provide thermal energy via electricity.

Table 2.5 Cost of reference TSA process (four cycles per day at UT) for different assumptions regarding the availability of steam during the desorption step

Electricity source	Monetary cost ($/tCO$_2$-net) [a]			
	Scenario I No Steam [c]	Scenario II Dedicated Steam	Scenario III Purchased Steam	Scenario IV Waste Steam
Coal				
Conventional coal	N/A [b]	162.8	138.2	58.6
IGCC	N/A [b]	161.3	138.5	60.9
IGCC with CCS	408.1	120.2	108.3	57.3
Natural Gas				
Conventional combined cycle	494.3	95.9	85.5	43.3
Advanced combined cycle	471.9	94.3	84.1	42.6
Advanced CC with CCS	196.8	92.5	83.8	45.4
Other				
Advanced nuclear	213.4	100.0	90.9	50.0
Wind	181.7	92.7	84.2	46.3
Wind—offshore	455.7	156.4	142.1	78.1
Solar PV	394.8	142.2	129.2	71.0
Solar thermal	584.2	186.3	169.3	93.0
Biomass	337.1	108.9	98.1	51.9
Hydro	161.9	88.0	80.0	44.0

[a] electricity requirement = 783.6 MJ/tCO_2, steam requirement = 5961.6 MJ/tCO_2, [b] the net amount of CO_2 captured is negative and results in net emission of CO_2, [c] similar to the analysis of House et al.

The estimated costs for Scenario II and III are similar as they only differ in the value of CO_2 emission factor used for steam. For most of the cases, the cost of the process when steam must be generated is ~ 10% higher than Scenario II. Recalling that

the net cost of capture is favored by low cost electricity and a favorable CO_2 emission factor, two trends can be observed. Firstly, the carbon free sources of electricity such as solar and off-shore wind are more expensive (\$130-170 MJ/tCO_2, Scenario III) because of the high cost of generating this electricity. Similarly, cheap sources of electricity such as coal (without CCS) are more expensive (~ \$140/tCO_2) because of high CO_2 emissions from these sources. Secondly, the minimum cost is obtained with electricity sources that have both zero CO_2 emissions and a reasonable cost (advanced nuclear = \$90.9, wind = \$84.2 and hydro = \$80.0/tCO_2), or cheap conventional sources with lower emissions than coal such as natural gas (~ \$85/tCO_2). When compression costs are not included these costs reduce to \$60 - \$70/tCO_2 for natural gas and \$70-\$90/tCO_2 for coal based electricity. Depending on the source of electricity, decreases of 25% - 45% are obtained when the cost of compression is not added.

For practical purposes, Scenario IV is exactly the same as Scenario III. The subtle difference between the two scenarios is the ownership of emitted CO_2 released due to the generation of low pressure steam used in the process. Assuming that there is a source of LP steam that will otherwise be wasted, the values reported for Scenario IV should be interpreted as the monetary cost that will be incurred to prevent wasteful emission of ton of CO_2 to the atmosphere. Unlike the previous scenarios, this will depend strongly on the CO_2 emission portfolio of the relevant industry as the responsibility of the relevant CO_2 emission still lies with the industry. This cost is again the lowest for natural gas based sources and is ~\$40/tCO_2 (Table 2.5).

An interesting observation is associated with the implementation of carbon capture and sequestration (CCS) processes for conventional sources like coal and natural

gas. When CCS is implemented for natural gas, the estimated price of electricity increases but the net cost for air capture decreases slightly (from \$84.1 to \$83.8/tCO_2). For coal the effect is more dramatic as the cost reduces from ~ \$138/tCO_2 (for IGCC) to \$108/tCO_2 when CCS is implemented. In this case, implementation of CCS processes causes an increase in the electricity cost, but at the same time reduces the CO_2 emissions from 0.9 to 0.2 tCO_2e/MWh. We emphasize that air capture processes are not intended to be an alternative for point source capture. Instead of being a competitive technology, air capture is intended towards being a complimentary technology that captures CO_2 that is inaccessible to other conventional methods.

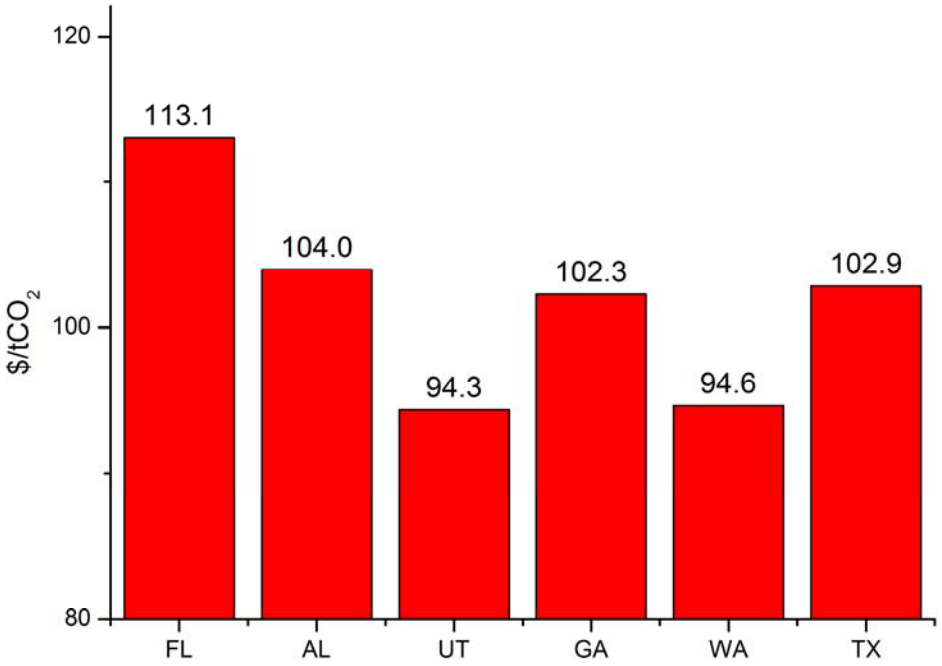

Figure 2.4. Cost of process (Scenario II) for four cycles per day at different locations assuming natural gas advanced combined cycle as the source of electricity.

At this stage it is useful to analyze the cost of air capture at the different locations. Figure 2.4 compares the cost of air capture process for four cycles per day at different locations assuming generation of dedicated steam (Scenario II) and advanced combined cycle as the source of electricity. The cost in UT, \$94.3/tCO_2, is approximately 15 % smaller than the cost in FL (\$113.1/tCO_2). As explained earlier, this is a direct result of higher working capacities in UT.

For a commercialized air capture process, electricity will typically be obtained from the grid. It may appear that the entire discussion of the source of electrical power is moot as any operator would always pay a power cost that is weighted over all the sources of electricity generation. The usefulness of the above analysis lies in the fact that for all the possible sources of energy, the cost of air capture is not as high as previously expected.[28]

In this section, our analysis of a specific TSA process suggests the operating cost to be of the order ~\$80 - \$150/tCO_2 captured. It should be highlighted that these estimates include only the energy of operation of each process; they do not include costs of capital expenditures for constructing and/or maintaining equipment. Keeping in mind the relatively high yields (~1 tCO_2/day) and purities (88.5%) possible, this process may form the basis for a useful approach to capturing CO_2 from air. Efforts targeted towards establishing detailed process models and economic analyses for this process would be worthwhile.

2.5. Potential Process Improvements

From the analysis presented above, it is clear that the dominant contribution to the cost of adsorption-based air capture is associated with the sensible heat requirements of

the monolith. For the reference case presented above (including compression), the thermal heat requirements are ~ 38% for the monolith and ~27% for the adsorbent. In this section, we discuss two different strategies for reducing the overall cost of air capture. Of the different sources of electricity explored in the earlier section, IGCC with CCS (coal), Advanced combined cycle (NG) and wind are used as examples (Scenario II).

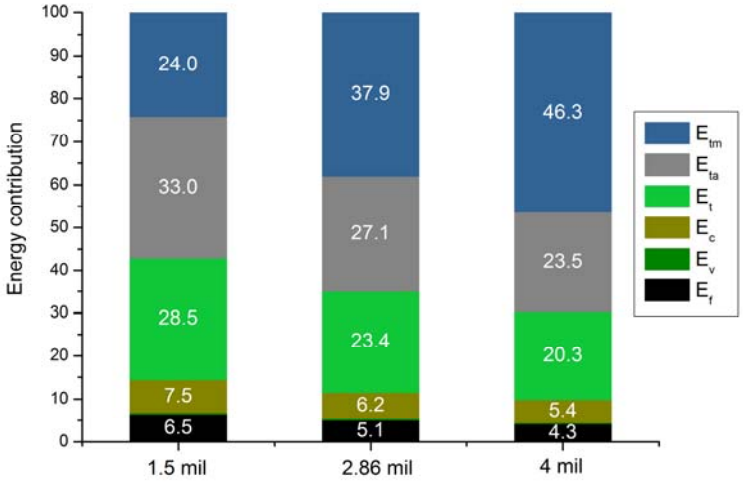

Figure 2.5. Energy requirements for 1.5, 2.86 and 4 mil wall thickness. The total energy requirements are 5536, 6745 and 7774 MJ/tCO_2, respectively.

2.5.1. Monolith configuration

The first approach is to reduce the mass of the monolith by keeping the amount of adsorbent constant and to change the wall thickness of the monolith, since this will directly decrease the sensible heat required for the process. Figure 2.5 shows the distribution of energy requirements for three different wall thicknesses, 1.5 mil, 2.86 mil and 4 mil. These correspond to adsorbent to monolith ratios of 1.9, 1.0 and 0.71 kg-adsorbent/kg-monolith respectively. By reducing the wall thickness, the total energy decreases from 7774 MJ/tCO_2 (4 mil) to 5536 MJ/tCO_2 for 1.5 mil and the contribution of E_{tm} decreases from ~47% to less than 25%, respectively.

The decrease in energy requirements affects the cost required for capture. Figure 2.6 shows the monetary cost for different monolith configurations. For electricity generated from natural gas, the cost decreases from \$94.3/tCO_2 (reference case) to \$66.2/tCO_2 for the minimum thickness. For the more unfavorable scenario of a larger wall thickness, the cost increases to \$132.0/tCO_2. The trends for other sources of electricity are very similar, and are shown in Figure 2.6.

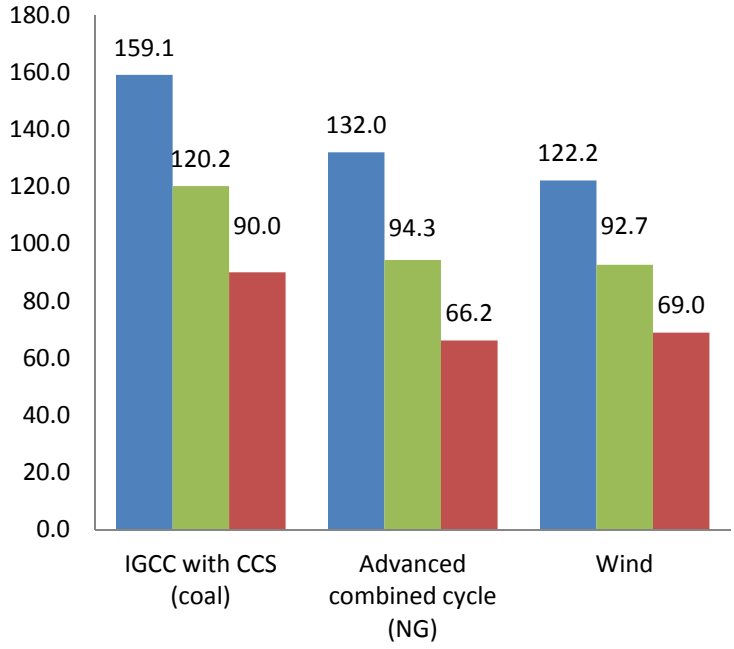

Figure 2.6 Monetary cost of the process using four cycles per day at UT for a 1.5 mil (red), 2.86 mil (green) and 4 mil (blue) channel wall thickness of the contactor.

These results show that there is a strong dependence on the cost of the process with the energy required for regeneration of the adsorbent. This depends on the parasitic losses incurred for the sensible heat requirements of the monolith. It is important to note that a minimum parasitic loss is determined by the structural strength of the material of construction rather than by thermodynamics. An ideal material of construction should

have a low thermal mass without compromising on the structural strength required for manufacturing processes.

2.5.2. Adsorbent capacity

We have shown that the amount of product recovered in the process is not affected by the sensible heat requirements of the process. It is of course useful to minimize the parasitic losses per unit of CO_2 captured and ideally, a high ratio of the adsorbent to the monolith is desired. Practically, this ratio will be decided by the manufacturing limitations of the contactor and cannot be easily improved beyond a certain value. Another approach is to increase the throughput of CO_2 obtained during *each* adsorption desorption cycle. One way of achieving this is by increasing the adsorption capacity of CO_2 at ambient conditions. Recently, various adsorbents with higher uptakes of CO_2 than TRI-PE-MCM-41 have been reported.[38-41] For the amine modified silica adsorbents of interest, this is possible by increasing the amine loading of the adsorbent.[39,40]

To explore the impact of increased adsorption capacity, we performed calculations with modifications of the adsorption isotherm used above. Specifically, the maximum chemisorption capacity of CO_2, $(ns_0)_{chemi}$, was increased from 3.64 mmol/g in steps of 20%, which resulted in increased uptakes at ambient conditions. It should be noted that a change in ns_0 does not directly imply a corresponding change in CO_2 uptake; as ns_0 is a theoretical capacity obtained from a mathematical fit, while the real uptake will depend both on the partial pressure and the temperature. We find that the average uptakes during adsorption increase from 1.07 mmol/g for the original case, to 2.14 mmol/g for the largest change in $(ns_0)_{chemi}$. Even the highest uptake is reasonable as recent studies have

reported values as high as 1.71 mmol/g at 420 ppm CO_2 (dry) for PEI grafted fumed silica.[41] The same study has reported CO_2 uptake of 1.74 mmol/g (humid) by a similar adsorbent.[41] This increase in the CO_2 adsorption capacity implies that larger amount of air must flow through the contactor to saturate the adsorbent, resulting in longer adsorption time. The calculated adsorption time increases from 1.7 hours for the original case to a maximum of 3.3 hours. The assumption of four cycles per day is still reasonable, as the adsorption times are still much smaller than the total cycle time of six hours per cycle. For the specific case of amine modified adsorbents, studies have shown that increasing the amine loading causes a reduction in the adsorption rates of CO_2.[39] In these calculations we have inherently assumed the validity of the equilibrium model at large adsorption time scales for all working capacities.

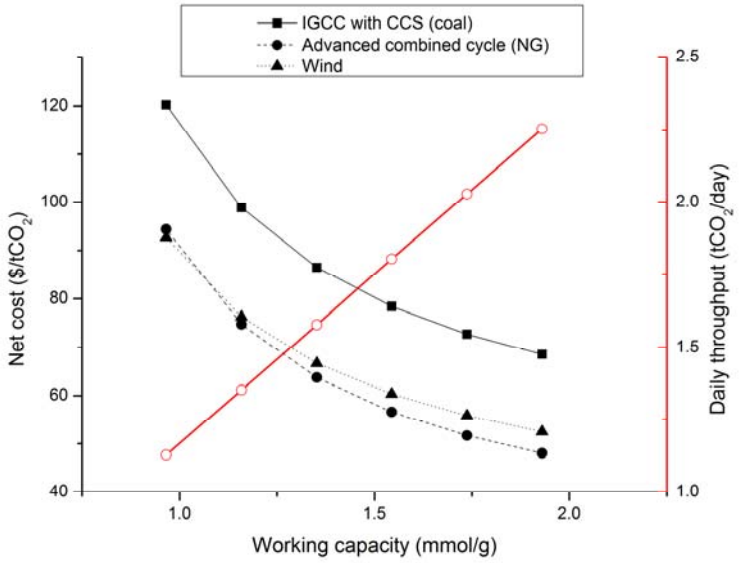

Figure 2.7 Daily throughput of CO_2 (red, open) and cost capture (black) as a function of increasing working capacity of the process

The increase in the adsorption capacity of CO_2 causes more CO_2 to be present in the system relative to N_2, and results in a higher purity of the product. More importantly,

the increased CO_2 uptakes directly result in a linear improvement of CO_2 product recovery (Figure 2.7). The total CO_2 obtained increases from 1.1 tCO_2/day (at a working capacity < 1 mmol/g) to 2.25 tCO_2/day at the highest working capacity of 1.93 mmol/g CO_2. This also results in a decrease of the total energy requirements, as the parasitic losses incurred due to the monolith are reduced. Figure 2.7 also shows the monetary costs as a function of increasing working capacity of the adsorbent. By increasing the working capacity to ~2 mmol/g, the cost of CO_2 capture can be decreased to $50-80 for different sources of electricity.

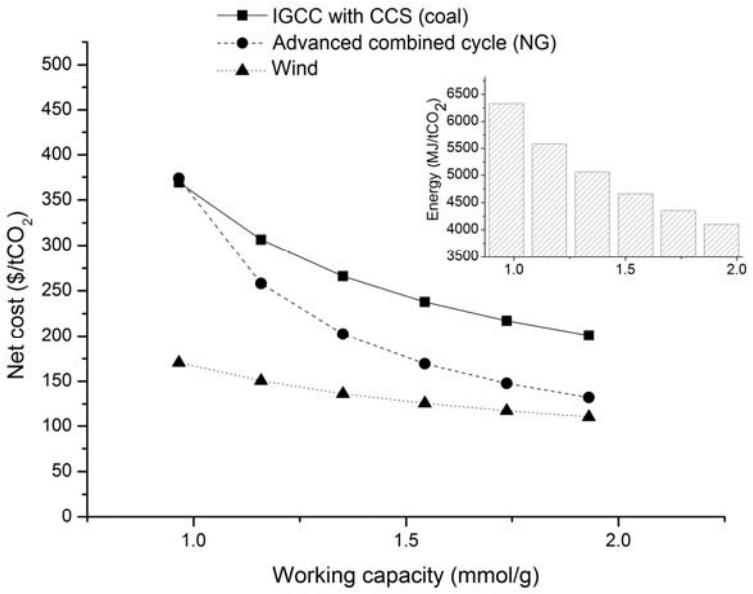

Figure 2.8. The cost of capture and the total energy (inset) as a function of working capacity, calculated based on the methodology of House et al.[28]

It is also useful to analyze the cost of the process using the methodology of House et al.,[28] assuming all the energy is provided by electrical power. In order to be consistent with the previous calculations, [28] compression of the product is not included. For the working capacity of the process using the actual adsorbent (0.97 mmol/g), the cost of the process is estimated to be ~ $375 MJ/$tCO_2$ for an energy requirement of ~ 6328 MJ/tCO_2.

As the working capacity increases, the energy required decreases from 6328 to 4102 MJ/tCO_2 (Figure 8, inset) and the second law efficiency is improved from 7.4 % to 11.6 %. These energy requirements are in reasonable agreement with the predictions of Wurzbacher et al.[47] (166kJ/molCO_2 or 3772.7 MJ/tCO_2) for a 2 mmolCO_2/g working capacity. Their calculated value is lower, as it does not account for the CO_2 emissions associated with generation of the required energy. At the highest working capacity of 1.93 mmol/g, the costs can be reduced to ~ \$110 - \$200/tCO_2 depending on the source of electricity. Thus, even under the assumption that all the energy is obtained from electricity, the cost obtained is much lower than \$1000/tCO_2 estimated by House et al.[28]

2.6. Conclusions

For a technology intended to capture of CO_2 from ambient air to be economically feasible, it needs to be applicable on a large scale at low costs. Prior to this work, the only technology for this purpose that had been examined in detail was absorption into alkaline solutions. This approach was shown to have very high operational costs.[30] Most of the current research in adsorption based technologies has focused on materials development for CO_2 adsorption and on lab scale adsorption experiments. [37,39,40,43-48,55-59] To determine the economic feasibility of the technology, analysis at the process simulation level is essential.

In this chapter, we have considered several variations of temperature swing adsorption processes based on a highly selective adsorbent that has been demonstrated previously in lab scale experiments. [37,45,55,57] We have developed preliminary process models to estimate the product purity, throughput, and operation costs. These models

made it possible to vary a number of key process parameters to understand which factors have the most significant impact on process performance.

When using steam for desorption and purging, a specific process was described in which about 1.1 tCO_2 is obtained per day from a unit the size of a standard shipping container at purities of ~ 88.5 % CO_2. For this process the total energy requirement was calculated as 6745 MJ/tCO_2 (including compression), of which 5962 MJ/tCO_2 was thermal. Assuming that the electricity is obtained from natural gas and that dedicated steam needs to be generated for the process, the operational cost for this process is estimated to be $\$95/tCO_2$ for the reference scenario. Realizing that the sensible heat for monolith contributes ~ 39% of the total energy requirements and represents a parasitic loss to the process, we explored different possibilities of improving the process. Our results suggest that using a suitable material for the monolith and using adsorbents with higher uptakes, can lead to a further reduction of the operating energy and monetary costs.

CHAPTER 3

DFT DERIVED FORCE FIELDS FOR MODELING HYDROCARBONADSORPTION IN MIL-47(V)

Molecular modeling calculations using generic force fields such as UFF and DREIDING are widely used for predicting molecular adsorption and diffusion in metal-organic frameworks (MOFs), but the accuracy of these force fields is has not been thoroughly tested. In this chapter, we describe a general framework for developing transferable force fields for modeling adsorption of alkanes in MIL-47(V) using periodic Density Functional Theory (DFT) calculations. By calculating the interaction energies for a large number of energetically favorable adsorbate configurations using DFT, we obtain force fields that give good predictions of adsorption isotherms, heats of adsorption and diffusion properties for a wide range of alkanes and alkenes in MIL-47(V). Encouragingly, our results suggest that the force field is transferable to related materials such as MIL-53(Cr) and can be used to calculate the free energy differences for the experimentally observed phases of MIL-53(Fe).

3.1. Introduction and Literature Review

Hydrocarbon separations are of considerable importance in the chemical industry, and many MOFs have been studied using both experimental and computational techniques.[68] For instance, open metal site MOFs such as HKUST-1[2,69,70] and MOF-

74[71,72] series show preferential adsorption of olefins over paraffins for both long[73,74] and short chain[75] hydrocarbons. This selectivity is primarily attributed to the strong interaction of the unsaturated metal center with the olefin double bond. [69,71] Another interesting separation that has been widely studied using MOFs is the removal of p-xylene from mixture of C_8 alkyl aromatics.[76-78] The most commonly reported MOFs used for this application includes the MIL-47 and MIL-53 series, which show selective adsorption of *p*-xylene.[79,80] A number of MOF materials have been studied for various other hydrocarbon separations, as summarized in a recent review by Herm et al.[68]

The ordered crystalline structure of MOFs makes them amenable to computational studies for predicting adsorption properties. Grand Canonical Monte Carlo (GCMC) simulations have been used to calculate adsorption isotherms for various small molecules using generic force fields. For example, this approach has been employed for high throughput screening of MOFs for CO_2 capture[81] and methane storage[82] applications. Generic force fields such as DREIDING[83] and the Universal Force Field (UFF)[84] are straightforward to implement and give reasonable results for simple systems.

A limitation of generic force fields is their suitability for systems that involve specific interactions [85]. For example, due to the presence of open metal sites, UFF and DREIDING fail at predicting adsorption of CO_2 in the MOF-74 series.[50,51] Similarly, the adsorption of olefins in HKUST-1 MOF cannot be well described by traditional approaches.[86-88] These observations suggest that due to the large diversity of available MOFs and functional groups, generic force fields may not always be suitable for describing complex MOF/adsorbate.[89]

One approach that is gaining in popularity is to use force fields that have been developed from quantum chemical calculations to model interactions nanoporous materials.[90-93] A recent review from Fang et al.[89] provides a summary of the work in this area. A reasonable trade-off between computational cost and accuracy in many circumstances is provided by using Density Functional Theory (DFT). Force fields obtained from DFT have been previously used for modeling diverse systems including CO_2/zeolites,[24,94] water/HKUST-1[85], CH_4/HKUST-1[95], CO_2/MOF-74[51] and H_2O/MOF-74.[51]

As summarized above, most of the literature on ab-initio force field development for MOFs has been focused on modeling interactions of open metal sites with small molecules (CO_2, H_2O) or with olefins.[89] The limited number of computational studies for long hydrocarbons use off-the-shelf force fields such as DREIDING or UFF to model the MOF framework.[96-98] Even though the predicted isotherms may be in reasonable agreement with experiments, the accuracy of the generic force fields to model the interactions is unclear. To the best of our knowledge, first principles derived force fields for long chain paraffin and olefins have not been reported for MOFs.

In this Chapter, we propose a general methodology for obtaining force fields for long chain flexible adsorbates in MOFs using periodic DFT calculations. Of the MOFs that have been studied for alkane adsorption, reliable experimental data is available for MIL-47(V) and the MIL-53 series.[96,97] To avoid complications associated with framework flexibility of MIL-53 series,[17,99,100] we choose MIL-47(V) as our model system for force field development.

The Chapter is organized as follows. In Section 3.2, a brief overview of our algorithm and the computational methods is presented. Sections 3.3-3.5 describe the development and application of our force fields for predicting adsorption and diffusion of alkanes in MIL-47(V). A brief extension of our approach to modeling olefins is presented in Section 3.5. Finally, in Section 3.6, we evaluate the transferability of the force field to MIL-53(Cr), and study the guest-induced structure transitions of MIL-53(Fe).

3.2. Force Field Development Algorithm

3.2.1. Overview

The goal of our force field development strategy is to ensure that the force field parameters reproduce the DFT energy for various configurations of the adsorbates in MIL-47(V). Briefly, this is done by generating a number of configurations from an initial generic force field, calculating the DFT interaction energies for these configurations for the periodic system and fitting a classical force field to the DFT data to obtain the new force field. Next, this new force field is used to generate another set of adsorbate configurations and this process is repeated until sufficient convergence of the force field parameters is obtained.

3.2.2. Structure optimization

The structure for MIL-47(V) was obtained from the literature[101] and was fully optimized using DFT as implemented in Vienna ab-initio Simulation Package (VASP). The GGA functional of Perdew, Burke and Ernzerhof [102] was used with Grimme's D2 [103] corrections to include dispersion interactions with the PAW method[104]. The lattice

constants were optimized at a plane wave cutoff of 700 eV while, the internal coordinates were energy minimized at a 400 eV cutoff. All single point DFT calculations were performed at the Γ-point to reduce computational cost. The DFT optimized lattice constants give good agreement with the experimental data.

3.2.3. Initial configurations and DFT interaction energy

For a force field to be well suited to predicting adsorption, it is essential to describe the energetics of the relevant low energy adsorbate configurations accurately. One approach to is to generate hundreds of adsorbate configurations randomly for single point energy calculations.[24,94] For extended molecules such as linear C_3 - C_9 hydrocarbons this approach is not straightforward as the adsorbate molecules are flexible. Additionally, it is likely that only a small fraction of randomly generated configurations will be energetically favorable. Instead, we performed configurational bias Monte Carlo (CBMC)[105] using an initial force field to obtain candidate low energy adsorbate configurations at P/P_0 = 0.1 and 303 K. Specifically, we use the generic DREIDING force field[83] and Lorentz-Berthelot mixing rules to obtain the preliminary set of hydrocarbon configurations, as it has been shown to reasonably predict hydrocarbon adsorption in MIL-47 (V).[96]

The hydrocarbons are modeled as flexible molecules using the united atom TraPPE force field[106]. In the TraPPE description of hydrocarbons, no charges are assigned to the united atoms and the intermolecular interactions are described by a simple Lennard-Jones potential. To be consistent with the TraPPE force field, the pairwise interactions of the adsorbates with the MOFs are modeled using only Van der Waals

terms. Details of the fluid-fluid interaction model, DREIDING parameters and the atom types for MIL-47(V) are provided in Table B1.

The interaction energy of the adsorbate molecules with the framework is defined as

$$E_{interaction} = E_{MOF+ads} - E_{MOF} - E_{ads} \quad (3.1)$$

where E_{MOF} and E_{ads} refer to the DFT energies of the empty MIL-47(V) framework and the hydrocarbon molecule, respectively, while $E_{MOF+ads}$ is the DFT energy of the combined system. Typically, we use 300 - 600 adsorbate configurations to derive a set of force field parameters. Note that only united atom positions are obtained from CBMC snapshots. Thus, hydrogen atoms must be correctly added to carbon chains prior to the DFT calculation. The length of a linear C_6 hydrocarbon (~ 6.3 Å) is comparable to the unit cell size along the *a* axis of MIL-47(V), so DFT calculations with 1×1×1 unit cell may cause overlap of the adsorbate with its own periodic image. Thus, all the DFT single point energy (SPE) calculations are performed using a 144 atom, 2×1×1 supercell of MIL-47(V) with reciprocal space sampled at the Γ point.

The interaction of hydrocarbons with MIL-47(V) is dominated by dispersion interactions and a DFT method that accounts for these interactions is required. Since the goal of this work is to develop force fields that are consistent with a given DFT method, we use two different DFT methods, PBE-D2 [103] and vdW-DF2 [107] for our calculations.

3.2.4. Parameter fitting and functional forms

The DFT energies obtained from CBMC configurations are fit to a chosen potential form of a force field in a least squares sense. Specifically, we consider two functional forms, namely the Lennard-Jones (LJ),

$$V = \sum 4\varepsilon_{ij}\left[\left(\frac{\sigma_{ij}}{r}\right)^{12} - \left(\frac{\sigma_{ij}}{r}\right)^{6}\right] \tag{3.2}$$

and the Buckingham potential,

$$V = \sum p_0 e^{-p_1 r} - \frac{p_2}{r^6}. \tag{3.3}$$

Compared to the two parameter (ε and σ) LJ potential, the Buckingham potential has three parameters (p_0, p_1 and p_2) and should therefore fit the underlying data better. For the LJ potential, two types of parameter fits were attempted. In the first case, we fix the σ parameter to the value given by Lorentz-Berthelot mixing rules (DREIDING + TraPPE) and only vary the ε parameter during the fitting procedure. In the second fitting procedure we allow both the ε and σ of each interacting pair to vary. All the parameter fitting calculations were implemented in MATLAB.

3.2.5. Adsorption isotherms and convergence of force field parameters

The newly fitted force field parameters were used for calculation of adsorption isotherms using configurational-bias Monte Carlo (CBMC) as implemented in the RASPA simulation code [108]. The pairwise interaction potentials were truncated and shifted to zero at a cutoff of 13.0 Å. The CBMC calculations were carefully equilibrated

using at least 100,000 cycles. Production runs of 400,000 cycles were used for measuring macroscopic properties.

The first iteration of the FF parameters is obtained by fitting the configurations obtained from a generic force field. Even though interaction energies are calculated using DFT, they may not be well converged with respect to the DFT method within a single iteration. To ensure convergence, we obtained configurations from the new force field and repeated steps described above in sections 3.2.3 - 3.2.5 to obtain the next iteration of the FF parameters. At each step, the configurations from all the previous iterations are used for fitting. As we show later, typically, 2 iterations are sufficient to obtain well converged FF parameters and adsorption isotherms.

3.3. Comparison of DREIDING FF with DFT

Before moving to the FF development of ethane, it is useful to compare the energies of the generic DREIDING FF with the PBE-D2 DFT method for long hydrocarbons. We obtained adsorption isotherms and CBMC configurations for several C_5 alkane and alkene isomers using the DREIDING FF. Figure 3.1 compares the PBE-D2 and DREIDING interaction energies for 100 configurations of pentane, 1-pentene and trans-2-pentene in MIL-47(V). The mean absolute deviation (MAD) for the alkenes (3.6 and 5.6 kJ/mol) are significantly higher than for pentane (2.6 kJ/mol). The DREIDING interaction energies for trans-2-pentene shows a systematic underprediction for low energy configurations. This indicates that the DREIDING FF is not consistent with PBE-D2 and that a FF can be developed to better reproduce the DFT energies.

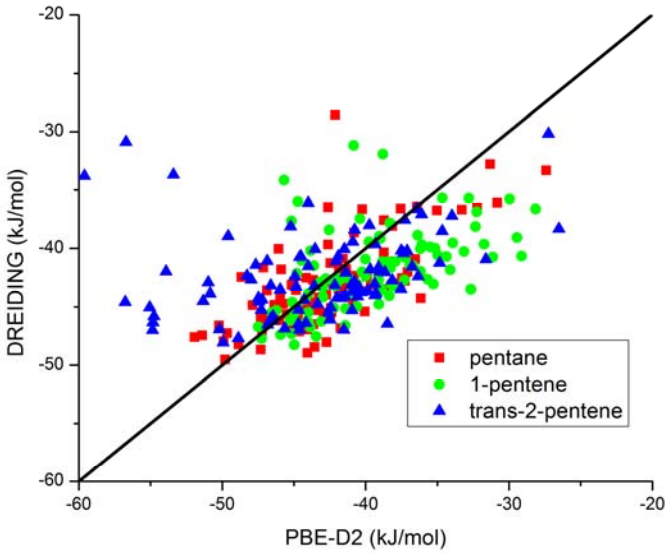

Figure 3.1. Interaction energies for 100 configurations of pentane (red squares), 1-pentene (green circles) and trans-2-pentene (blue triangles) using the DREIDING FF and PBE-D2 in MIL-47(V).

3.4. Force Field Development for Ethane

3.4.1. Method overview

We now move to modeling adsorption of ethane in MIL-47(V) using our force field algorithm. As summarized in Section 2.3, we use a generic force field to obtain the initial set of configurations for DFT calculations. Figure 3.2 shows the PBE-D2 interaction energies (blue triangles) for 200 configurations obtained from the DREIDING FF. Compared to PBE-D2, the DREIDING FF overpredicts adsorption energies by ~3 kJ/mol with a MAD of 2.5 kJ/mol. To make our classical FF consistent with PBE-D2, we fit the ε parameter for each LJ interaction pair (4 element types in all) using least squares fitting and recalculate the interaction energies with the new force field (denoted as FITTED_LJ). In this case, the σ values were held constant. By definition, the interaction

energies calculated with FITTED_LJ (Figure 3.2, red circles) show much better agreement with PBE-D2 than the results from the DREIDING FF; The MAD is reduced to ~1.3 kJ/mol with a mean deviation (MD) of 0.03 kJ/mol.

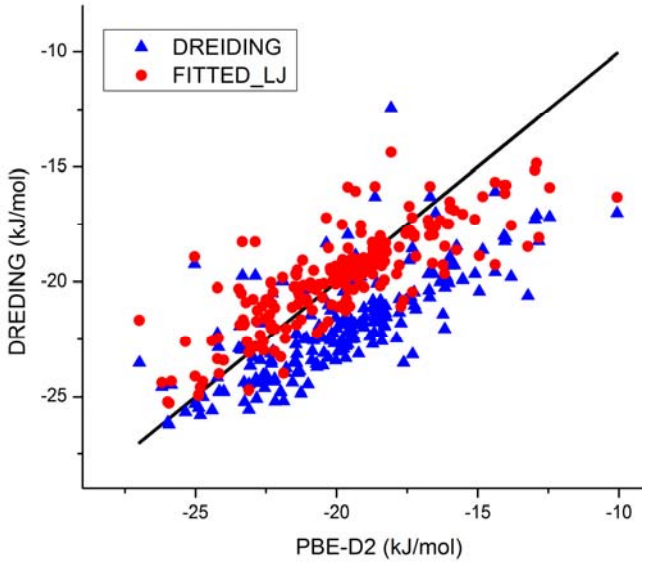

Figure 3.2. PBE-D2 interaction energies for 200 configurations of ethane in MIL-47(V) compared with generic DREIDING FF (blue triangles) and FITTED_LJ FF (red circles).

3.4.2. Convergence of FF parameters.

To ensure that the new FF (FITTED_LJ) reproduces the PBE-D2 data consistently, we performed CBMC again with the new FF and obtained 200 additional ethane configurations. These configurations were used to calculate PBE-D2 interaction energies and to re-parameterize the FF by fitting the ε values. The evolution of the force field parameters for 3 such iterations (Table B2) shows that the fitted FF parameters do not change significantly after 2 iterations. At each FF iteration, all the configurations from the previous iterations are included during the fitting procedure. We find that the fitting results and isotherms are essentially insensitive to the vanadium FF parameters.

This is not surprising as the V atom is octahedrally coordinated and does not directly interact with the adsorbates. Thus, the ε value for V is set to zero for all further calculations.

The convergence of the FF parameters is further confirmed by comparing the adsorption isotherms for various FF iterations in Figure 3.3. The adsorption isotherms for iteration 1, 2 and 3 do not differ significantly, but are all lower than the original DREIDING force field. The ethane force field is now consistent with PBE-D2 and is henceforth referred to as PBE-D2 FF. For all the results presented in this work, at least 2 force field iterations were used to guarantee good convergence of the parameters.

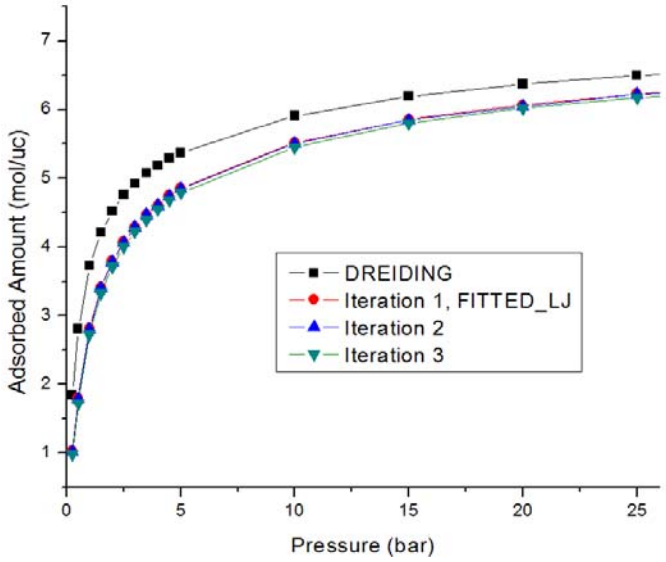

Figure 3.3 Ethane adsorption isotherms in MIL-47(V) at 303 K using 3 iterations of the DFT derived FF. The isotherms from the DREIDING FF is also shown for comparison.

3.4.3. Choice of classical potential form

In the previous section, we have shown that our approach can be used to develop force fields that can reproduce DFT energies in MIL-47(V) for a large number of configurations. We now turn to exploring the potential form used for fitting the data. The

MIL-47(V) framework consists of four types of elements, C, H, O and V. The ethane molecule is represented by the CH_3 united atom, resulting in four distinct pairwise interactions. Earlier, we used a LJ potential form and only allowed the 4 ε values to vary during the least squares fitting. Figure 3.4 shows the fitting results when the 4 σ values are also allowed to change, leading to a total of 8 fitting parameters for the system (blue triangles). Similarly, we can use Buckingham potential for each interacting pair resulting in 12 total parameters (Figure 3.4, green squares).

The MAD using 4 LJ parameters is reduced from 1.3 kJ/mol to 1.2 kJ/mol (1.1 kJ/mol) when 8 LJ parameters (12 Buckingham parameters) is used. Even though there is slight improvement in the quality of the fit by using more parameters, the final converged adsorption isotherms are not significantly different for various functional forms of the force field. To simplify the implementation of our DFT derived FFs, we choose the 4-parameter LJ model for all further calculations. The converged PBE-D2 FF parameters for ethane obtained by using 600 PBE-D2 calculations and fitted to a 4-parameter LJ potential form are presented in Table 3.1.

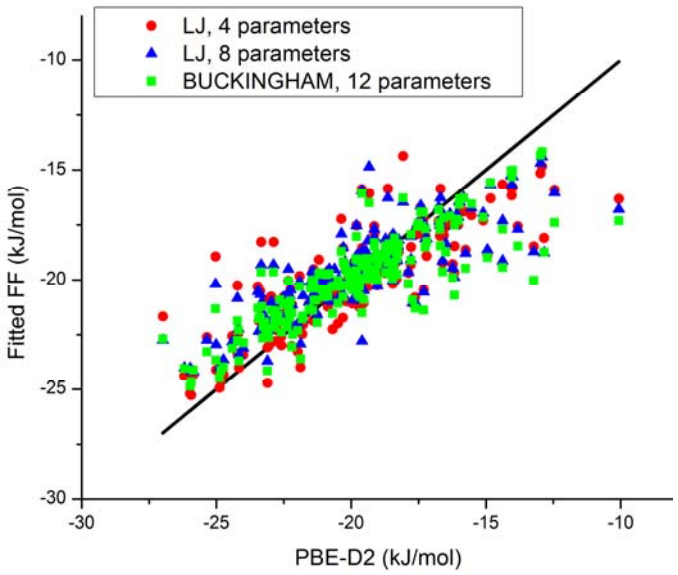

Figure 3.4. Comparision of the fitted FF interaction energies with PBE-D2 for different potential functional forms: LJ 4 parameters (red circles), LJ 8 parameters (blue triangles) and Buckingham, 12 parameters (green squares)

3.4.4. Choice of DFT method

We now discuss the FF development using DFT calculations using the vdW-DF2 functional (denoted as VDW-DF2 FF), which will be compared with the previous PBE-D2 FF. Figure 5 shows the PBE-D2, vdW-DF2, and DREIDING energies for 200 configurations of ethane in MIL-47(V) MOF. The data has been arranged according to increasing PBE-D2 interaction energies. For the most favorable configurations, the average vdW-DF2 interaction energy (-29 kJ/mol) is more negative than the PBE-D2 (-26 kJ/mol) result. Coincidentally, for these configurations, the DREIDING energies (-25 kJ/mol) are comparable to PBE-D2. As we move towards the less favorable configurations (towards the right in Fig. 3.5), the difference between the two DFT methods diminishes to zero at approximately -17 kJ/mol. For DFT interaction energies less negative than -17 kJ/mol, DREIDING FF overestimates the ethane-framework interactions relative to the DFT results.

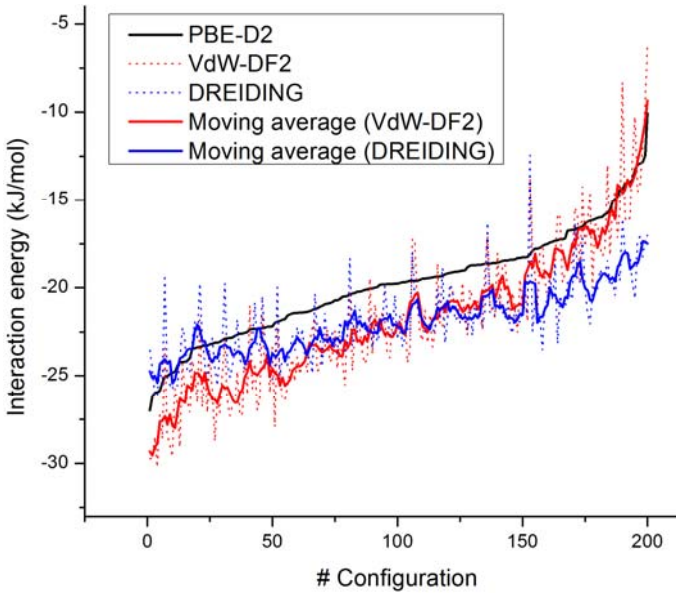

Figure 3.5. Interaction energies for 200 configurations of ethane in MIL-47(V) calculated using PBE-D2 (black, solid line) and vdW-DF2 (red, dotted line), and DREIDING FF (blue, dotted line). The moving average for vdW-DF2 (red, solid line) and DREIDING FF (blue, solid line) is calculated using 5 configurations for each data point.

Even though the DREIDING energy landscape is more flat than vdW-DF2, it is interesting to note that, the average interaction energies over the entire range are quite similar for the two methods (-21.8 kJ/mol). Comparing this to the PBE-D2 average (-19.9 kJ/mol), we expect PBE-D2 FF to predict lower ethane adsorption than both DREIDING and VDW-DF2 FF.

Similar calculations as before were performed using vdW-DF2 and the final VDW-DF2 FF is obtained after 3 FF fitting iterations. From the comparison of the vdW-DF2 interaction energies with the fitted force field for 600 ethane configurations, we find that the MAD for the vdW-DF2 derived force field is slightly higher (2.1 kJ/mol) compared to the PBE-D2 (1.3 kJ/mol) version.

Table 3.1 compares the final converged ethane force fields developed using the PBE-D2 and vdW-DF2 methods with the original DREIDING FF. It is interesting to note that ε(C-CH3) for DREIDING and VDW-DF2 FF are close to each other and are ~10 K

higher than the PBE-D2 FF. More importantly, both the DFT force fields predict a higher ε(O-CH3) than the DREIDING FF, indicating that increasing the O-CH3 interaction by 55 % (40 %) relative to the DREIDING value is necessary to better reproduce the PBE-D2 (vdW-DF2) interaction energy.

Table 3.1. Comparison of ε force field parameters for modeling adsorption of ethane in MIL-47 (V) using DREIDING, PBE-D2 FF and VDW-DF2 FF.

Adsorbate atom type	MOF atom type	DREIDING (ε, K)	PBE-D2 FF (ε, K)	VDW-DF2 FF (ε, K)	All FFs (σ, Å)
CH3_sp3_UA	C1	68.49	54.23	64.80	**3.61**
CH3_sp3_UA	C2	68.49	54.23	64.80	**3.61**
CH3_sp3_UA	C2	68.49	54.23	64.80	**3.61**
CH3_sp3_UA	O1	68.72	106.86	96.59	**3.39**
CH3_sp3_UA	O2	68.72	106.86	96.59	**3.39**
CH3_sp3_UA	V [#]	28.09	0.00	0.00	**n/a**
CH3_sp3_UA	H	27.38	6.13	14.08	**3.30**

[#] Note that the ε value for V-CH3_sp3_UA interaction has been set to zero.

3.4.5. Comparison with experimental data

As both PBE-D2 and vdW-DF2 are dispersion corrected DFT methods, it is difficult to determine *a priori* the most suitable approach. One way of resolving this issue is to compare the simulated adsorption isotherms with experimental data. Figure 3.6 compares the predicted ethane adsorption isotherms using the DREIDING, PBE-D2 FF and VDW-DF2 FF with the experimental data from Rosenbach et al.[97] at 303 K. Consistent with our predictions in Section 3.4.4, the PBE-D2 FF isotherms are indeed lower than the VDW-DF2 FF and DREIDING values. Additionally, due to the similar average interaction energies, the predicted uptakes from VDW-DF2 FF and DREIDING FF are comparable.

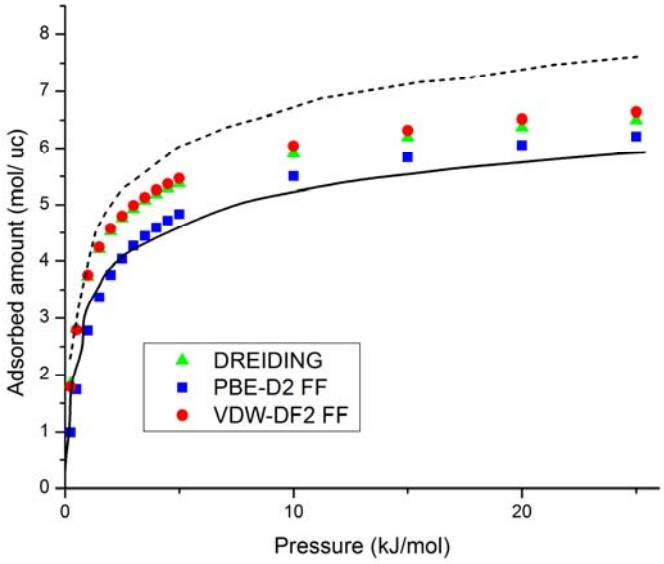

Figure 3.6. Ethane adsorption isotherms in MIL-47(V) using the PBE-D2, vdW-DF2 and DREIDING FFs. The simulation data is compared to the scaled (dashed line) and unscaled (solid line) experimental data from Rosenbach et al. [97]

Before comparing the DFT FF predictions with the experimental isotherms, it is useful to discuss the quality of the MOF sample used in the adsorption experiments [97]. The measured surface area for the MIL-47(V) sample (1200 m^2/g) was significantly smaller than the simulated value (1540 m^2/g), and the authors suggest scaling up the experimental isotherms by ~28% for comparison with simulations.[97] In this case, the low surface area of MIL-47(V) was attributed to an incomplete removal of terephthalic acid from the pores during the activation.[97] Similar to this approach, other groups have employed pore volumes to derive the necessary scaling factors.[109]

With regards to the measuring the BET surface area, Snurr and co-workers[65,110] have highlighted the importance of using an appropriate pressure range for the calculation [111]. They conclude that BET calculations with the standard pressure range ($0.05 < P/P_0 < 0.3$) may underestimate the true value. Given the nuances associated with measurement

of BET surface areas and the activation process, simply scaling up the experimental adsorption isotherm by almost 30% to compare with calculated data is less than optimal.

To explain this further, instead of considering the BET surface area as one number, we introduce error bars to this measurement and calculate the bounds on the scaling factors necessary to match the perfect sample. This is summarized in Table 3.2. If the error bar for a given BET measurement less than ±5%, then a scale up of anywhere between 22-35 % is necessary. If the error bar is now increased to ± 10%, the scaling factor range increases to 27-43 %. This quick calculation indicates that scaling adsorption isotherms for samples that are reported to have low BET surface areas compared to ideal theoretical values may lead to large uncertainties, depending on the accuracy of the BET calculation.

Table 3.2. Scaling factors for different hypothetical error bars in the measured BET surface area. The baseline surface area for the experimental and 'perfect' sample are 1200 m^2/g and 1540 m^2/g, respectively.

% Error in BET measurement	Scaling factor range
0	1.28
< ± 5	1.22 - 1.35
< ± 10	1.17 - 1.43
< ± 15	1.12 - 1.51

For situations in which the adsorption data has not been reproducibly reported by multiple groups, we choose to compare our simulated results with both the scaled and unscaled experimental isotherms. Figure 3.6 shows that the predicted adsorption isotherms from the two DFT methods, along with the DREIDING force field, lie in between the two experimental curves.

Although viewing the experimental data in this way does not indicate that any of the three FFs give implausible results, we cannot draw a clear conclusion about the suitability of the DFT derived force fields based only on this ethane adsorption data. Nonetheless, as we will show in the following sections, we are able to extend our method to higher alkanes and this allows us to compare our results to more reliable experimental adsorption measurements.

3.5. Force Field Development for Propane

From the ethane calculations above, we now have force field parameters that describe the interaction of the CH3_sp3_UA group with the MOF framework. As shown in Figure 3.7, propane molecules consists of two CH3_sp3_UA and one CH2_sp3_UA interaction centers. Similarly, within TraPPE, a hexane molecule is described by two CH3_sp3_UA and four CH2_sp3_UA interaction centers. To model the adsorption of higher linear alkanes, we need to correctly model the interaction of CH2_sp3_UA site with the MIL-47(V) framework atoms.

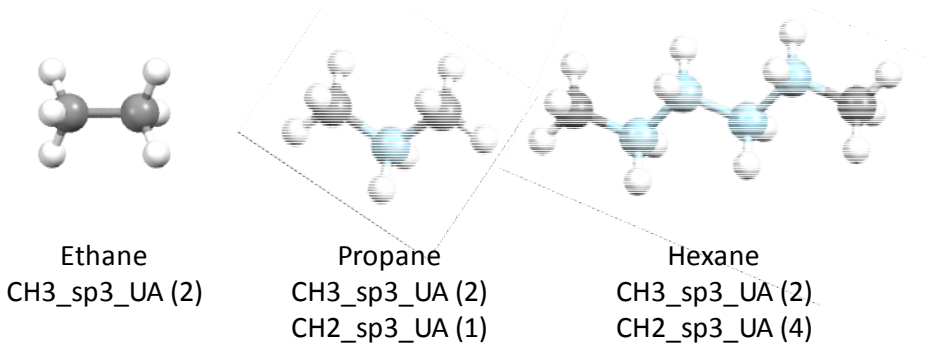

Figure 3.7. Description of linear alkanes using the TraPPE united atom model consisting of CH3_sp3_UA (grey) and CH2_sp3_UA (blue) interaction sites. The hydrogen atoms (white) have been shown for clarity and are not explicitly defined in the TraPPE force field. The number in the parentheses indicate the number of interaction sites of each type.

This is achieved by repeating the FF development algorithm for propane using the PBE-D2 and vdW-DF2 methods. Figure 3.8 (a) and (b) show the results of fitting propane interactions with the framework for PBE-D2 and vdW-DF2 methods, respectively. To make the force field transferable across different linear alkanes, we only allow the CH2_sp3_UA interaction parameters to vary during the parameter fitting, while the CH3_sp3_UA parameters from our ethane results (Table 3.1) are held constant. Similar to the ethane calculations, the LJ potential form with 4 ε parameters was used for fitting. Starting with an initial set of 600 configurations used for the fitting, we considered 600 additional configurations confirm the convergence of the FF parameters. The final mean absolute deviations for PBE-D2 FF and VDW-DF2 FF are 1.6 kJ/mol and 2.1 kJ/mol after two force field iterations, showing that the optimized force fields successfully reproduce the DFT energies.

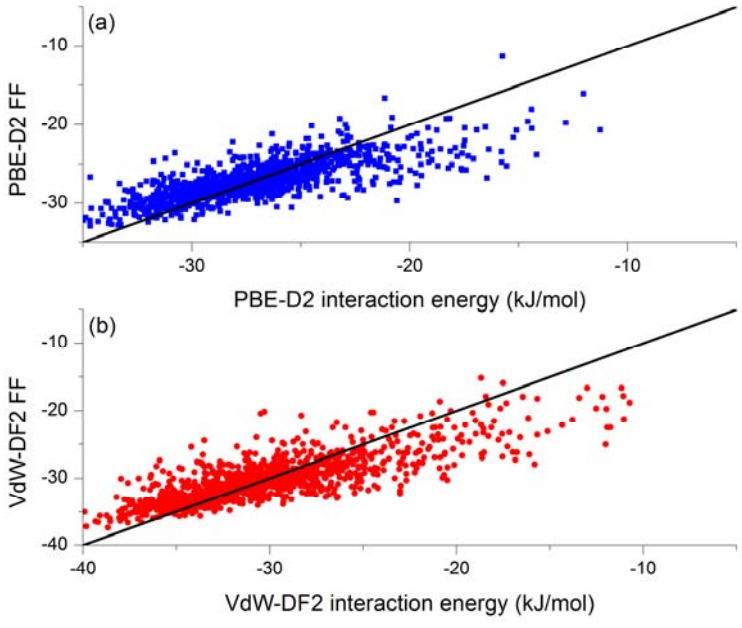

Figure 3.8. Force field fitting results for adsorption of propane in MIL-47(V) using (a) PBE-D2 and (b) vdW-DF2 DFT energies. In each case, 1200 adsorbate configurations

were used. Only the CH2_sp3_UA interaction parameters were allowed to vary, while the CH3_sp3_UA parameters were obtained from the ethane results in Table 3.1.

From a comparison of the two DFT methods for 600 propane configurations in MIL-47(V), we find that the vdW-DF2 method predicts stronger interaction energies than PBE-D2, especially for the more favorable configurations.

The new CH2_sp3_UA interaction parameters for DREIDING, PBE-D2 FF and VDW-DF2 FF are presented in Table 3.3. Comparing the ε values for DREIDING with the DFT FFs shows that the ε(C-CH2) does not change much, while the ε(O-CH2) increases ~50%. This is similar to the higher ε(O-CH3) observed for our DFT-derived ethane force fields in Section 3.4.4.

Table 3.3 Comparison of ε force field parameters for modeling adsorption of propane in MIL-47 (V) using DREIDING, PBE-D2 and vdW-DF2 derived force fields.

Adsorbate atom type	MOF atom type	DREIDING (ε, K)	PBE-D2 FF (ε, K)	VDW-DF2 FF (ε, K)	All FFs (σ, Å)
CH2_sp3_UA	C1	46.92	47.14	44.94	3.71
CH2_sp3_UA	C2	46.92	47.14	44.94	3.71
CH2_sp3_UA	C2	46.92	47.14	44.94	3.71
CH2_sp3_UA	O1	47.08	72.79	69.70	3.49
CH2_sp3_UA	O2	47.08	72.79	69.70	3.49
CH2_sp3_UA	V [#]	19.24	0.000	0.00	3.55
CH2_sp3_UA	H	18.75	2.84	19.65	3.40

[#] Note that the ε value for V-CH2_sp3_UA intraction has been set to zero.

The adsorption isotherms for propane in MIL-47(V) at 303 K using DREIDING, PBE-D2 FF and VDW-DF2 FF are shown in Fig. B1. The VDW-DF2 FF predicts higher uptake of propane than PBE-D2 FF and DREIDING. This is expected as the highest interaction energies are obtained with the VDW-DF2 DFT calculations (Fig. B2).

Similar to the ethane case discussed earlier, all three adsorption isotherms lay between the scaled and the unscaled experimental data. The experimental data for propane comes from the same study as the ethane data discussed above. For the same reasons as with the experimental ethane isotherms, the propane data does not allow a firm conclusion to be drawn on which simulated isotherm is more accurate.

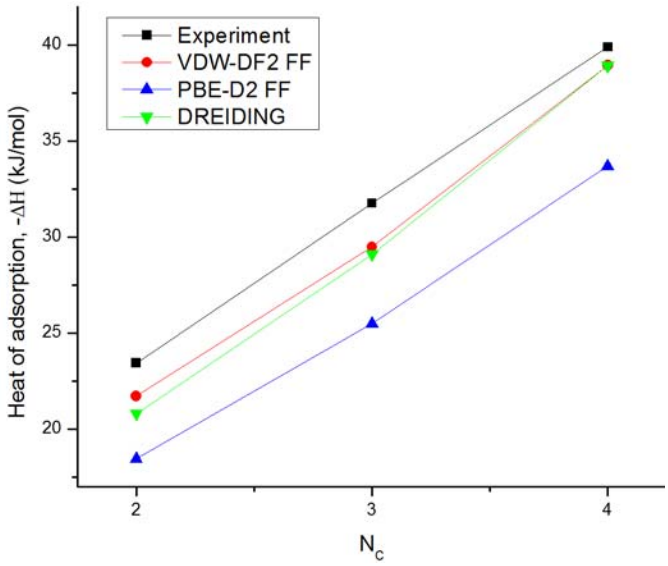

Figure 3.9. Comparison of the simulated heat of adsorption for ethane, propane and butane in MIL-47(V) at 303 K. The experimental microcalorimetry data measured by Rosenbach et al. [97] is included for comparison. N_C refers to the number of carbon atoms in the hydrocarbon molecule.

Even though we choose to not compare our GCMC results for light hydrocarbons to the full experimental isotherms, it is reasonable to compare the experimental and simulated heat of adsorption (ΔH) at low loadings. Figure 3.9 compares the low loading (P/P_0 = 0.001) ΔH obtained from CBMC simulations with the microcalorimetry measurements of Rosenbach et al.[97] at 303 K for ethane, propane and butane. As expected from our DFT calculations, the simulated heat of adsorption for C_2-C_4 hydrocarbons is the lowest for PBE-D2 FF. The VDW-DF2 FF and DREIDING values

are comparable to each other and are within 2 kJ/mol of the experimental measurement. It is encouraging that the slope of the line for VDW-DF2 FF (8.6 mol per -CH_2) is similar to the experimental result (8.25 kJ/mol per -CH_2).

Having verified that the predicted low loading heats of adsorption for C_2 to C_4 hydrocarbons are reasonable, we now proceed to extending our method to higher alkanes.

3.6. Force Field for Higher Alkanes

Linear alkanes described using the TraPPE FF consist of only two types from interaction centers: CH3_sp3_UA and CH2_sp3_UA. Using the force field parameters listed in Table 1 and 3 we can predict the adsorption of all linear alkanes using our DFT derived FFs.

Figure 3.10 (a), (b) and (c) compares the experimental adsorption isotherms for C_5-C_9 alkanes in MIL-47 (V) at 303 K reported by Déroche et al.[96] with the predicted uptakes using DREIDING, PBE-D2 FF and VDW-DF2 FF, respectively. Even though the BET surface areas of the MOF sample has not been explicitly reported by Déroche et al. [96] they did not rescale the adsorption isotherms while comparing their simulated isotherms. We therefore compare our data to the experimental results on the same basis, while acknowledging that this would be more satisfactory if information about the surface area of the experimental sample was available.

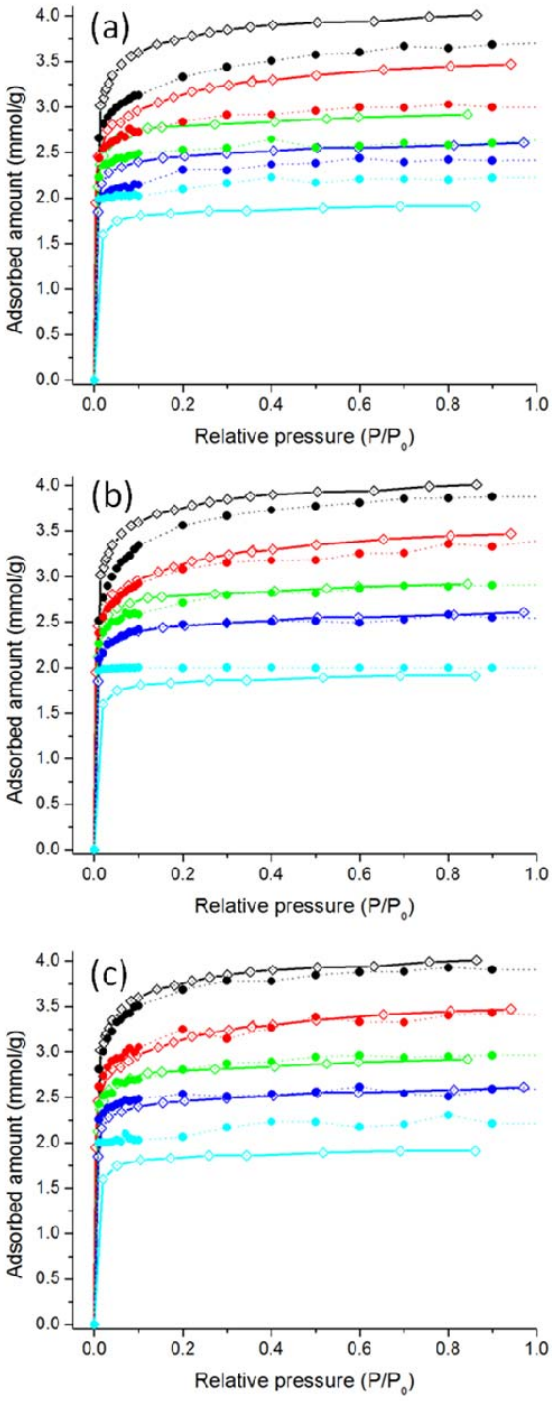

Figure 3.10. Adsorption isotherms for pentane (black), hexane (red), heptane (green), octane (blue) and nonane (cyan) in MIL-47(V) at 303 K. The predictions from CBMC (filled circles) using (a) DREIDING FF, (b) PBE-D2 FF and (c) VDW-DF2 FF are compared with the experimental data from Déroche et al. [96] (open diamonds).

We will first discuss the adsorption of C_5-C_8 alkanes using the three force fields. The DREIDING force field underestimates the adsorption of C_5-C_8 alkanes over the

entire pressure range. For these alkanes, the saturation capacity is systematically ~0.5 mmol/g lower than the experimental value. On the other hand, PBE-D2 FF gives significantly better agreement with the experimental data for C_6 to C_8 alkanes, both at lower pressures and at saturation. For pentane, a slight underestimation of ~0.2 mmol/g is observed at all pressures. The best prediction of the experimental data over the whole pressure range is obtained for the VDW-DF2 FF. In addition to getting the correct saturation capacity for C_5-C_8 at higher pressures, the shape of the predicted isotherm is in very good agreement with the experimental data for the C_5-C_8 linear alkanes.

We now turn to the inconsistency in the simulated and experimental isotherms for nonane (Fig. 3.10). Given that VDW-DF2 FF works well for the other alkanes, it is surprising that the saturation capacity of nonane is overestimated. The case for nonane is interesting because the experimental isotherm is lower than the simulated values for all three FFs. To examine this discrepancy, we used the experimental and VDW-DF2 FF isotherms to calculate the number of C atoms per unit cell at saturation for C_5-C_9 alkanes. Our calculations show that the MIL-47(V) unit cell saturates at approximately 20 C-atoms/unit cell for all hydrocarbons, except when the experimental nonane saturation capacity is used (1.9 mmol/g, 17 C/u.c). In contrast, the saturation capacity from the VDW-DF2 FF (2.2 mmol/g) corresponds to the same density (20 C/u.c.) calculated for the other cases. This result suggests that the experimental results for nonane adsorption may have been influenced by a kinetic limitations that cannot be considered in our equilibrium calculations. [54,96] It is noteworthy that the excellent adsorption predictions in Fig. 10 (b) and (c) are obtained by using FFs that are developed purely from theoretical methods and do not require any information or parameter tuning from experimental data.

The performance of VDW-DF2 FF is further confirmed comparing the low loading heat of adsorption (ΔH) for different force fields with the experimental values obtained by using Henry constants.[112] Figure 3.11 shows that the simulated ΔH values for C_5-C_7 hydrocarbons from VDW-DF2 FF are within 1 kJ/mol of the experimental data. The PBE-D2 FF systematically underpredicts the heat of adsorption, which is consistent with the relatively lower PBE-D2 interaction energies for ethane and propane (Fig. 3.5). On the other hand, DREIDING FF gives reasonable agreement with experimental and vdW-DF2 heat of adsorption, but fails at predicting the correct saturation capacities (Fig. 3.10 (c)).

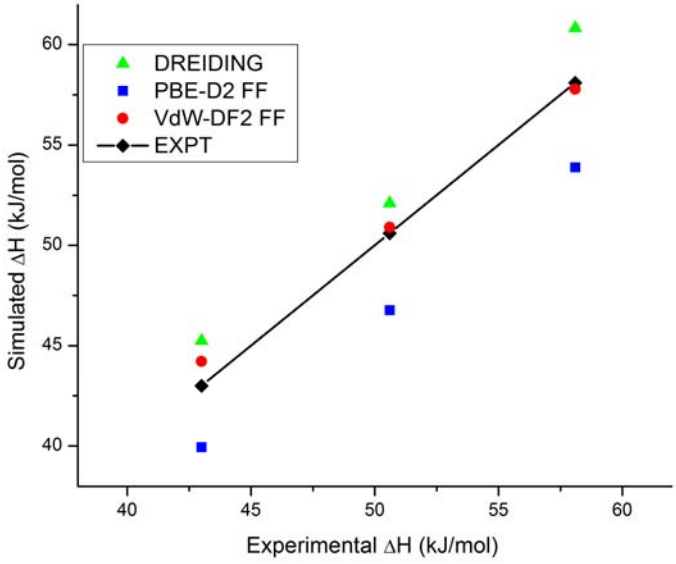

Figure 3.11. Simulated heat of adsorption for C_5, C_6 and C_7 alkanes at low loadings (P/P_0 =0.001) from DREIDING, PBE-D2 FF and vdW-DF2 FF compared with experimental zero-coverage heat of adsorption obtained from experimental Henry constants.[112]

In summary, as the VDW-DF2 FF gives excellent agreement with low coverage heat of adsorption measurements and experimental adsorption isotherms for a wide range of linear alkanes, we conclude that VDW-DF2 FF correctly describes the alkane/ MIL-

47(V) system. Even though the PBE-D2 FF does not perform as well as VDW-DF2 FF, it is still a considerable improvement over the original DREIDING force field.

3.7. Comparison of DFT-derived and generic FFs

Given that our DFT-derived FFs perform significantly better than DREIDING, it is important to explore the characteristics that distinguish them from the generic models. Similar to our DREIDING calculations, Déroche et al. [96] have reported adsorption isotherms for C_5 - C_9 alkanes using (1) the UFF force field and (2) a combined UFF + DREIDING approach. In both the cases, unsatisfactory prediction of the saturation capacities and/or the low pressure region is observed. Typically, self-interaction parameters defined by UFF or DREIDING for the framework atoms are combined with the fluid model using Lorentz-Berthelot mixing rules to obtain the required cross-species interactions. For the FFs developed in this work, we directly derive the cross-species interaction parameters from fitting to DFT calculations (Table 3.1 and 3.3). Using these cross species interactions and assuming Lorentz-Berthelot mixing rules to be valid; we obtain the self interaction parameters for the framework atoms based on DFT FF parameters. The force fields are referred as PBE-D2-LB and VDW-DF2-LB in Table 3.4.

Table 3.4. Self-interaction parameters (ε, K) for generic and DFT derived force fields to be used in conjunction with Lorentz-Berthelot mixing rules.

Framework atom	UFF	DREIDING	PBE-D2-LB FF	VDW-DF2-LB FF
C - C	52.87	47.87	39.16	43.38
O - O	30.21	30.21	115.85	100.41
V - V	8.06	8.06	0.00	0.00
H - H	22.16	7.65	0.28	5.21

Our calculations show that the ε(C-C) self-interaction parameters for the DREIDING (UFF) force fields is only ~20% (10%) higher than the VDW-DF2 FF. On the other hand, for both the DFT derived FFs, the ε(O-O) values are ~300% higher than the generic FFs. This observation indicates that the chemical environment of the oxygen atom bound to the metal center and subsequently, its interaction with the hydrocarbon is not well represented by UFF or DREIDING. Instead, using DFT calculations to derive the FF parameters allows for a more accurate description of the system and results in better prediction of adsorption properties.

3.8. Diffusion of alkanes in MIL-47(V)

Previously, we demonstrated that the VDW-DF2 FF performs better than the generic FFs at predicting the adsorption properties of alkanes in MIL-47(V). In this section, we discuss the diffusion properties of alkanes using VDW-DF2 FF and DREIDING FF.

Molecular Dynamics (MD) simulations in the NVT ensemble were used to calculate the diffusivities of C_2 - C_7 alkanes in MIL-47(V) at 300 K. All MD calculations were performed in RASPA[108] using a rigid 8×2×2 supercell of the framework. A time step of 1.0 fs was determined to be sufficient to ensure energy conservation. A typical MD trajectory consisted of a 10^6 equilibration steps followed by a 10^7 production steps during which mean squared deviation (MSD) of the alkane was measured. An order-N scheme[20] was used to calculate the self-diffusion coefficients from the MSD data. We used a minimum of 5 independent trajectories calculate the average self-diffusion coefficient for each hydrocarbon.

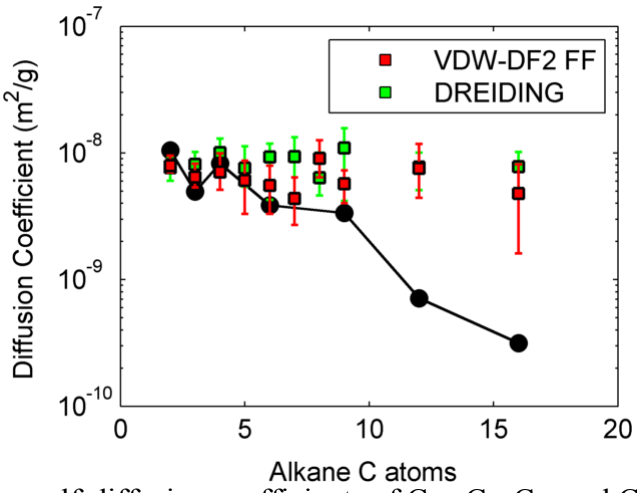

Figure 3.12. Average self-diffusion coefficients of C_2 - C_9, C_{12} and C_{16} alkanes obtained from NVT MD simulations at 300 K using VDW-DF2 FF (red squares) and DREIDING FF (green squares). The error bars denote the range of D_s values obtained from 5 independent MD simulations. Experimental QENS values reported by Rives et al. [98] are represented by the black circles. Note that the orientationally average self-diffusion coefficient is defined as $D_s = D_{1D}/3$.

Figure 3.12 compares the self-diffusivities (D_s) obtained for different alkanes at a fixed loading of 3 C atoms per unit cell at 300 K. This allows us to compare our self-diffusivities with experimental QENS measurements at the same loading.[98,113] The MD results in Figure 3.12 show that the self-diffusivity of alkanes in MIL-47(V) calculated using VDW-DF2 FF is in good agreement with the experimental results for C_2-C_7 alkanes. For these alkanes, slightly higher diffusion coefficients are predicted for the DREIDING FF. Because of its large 1D pores, it is not surprising that the diffusivities of alkanes in MIL-47(V) are insensitive to the details of the FF. Moreover, the observed diffusivities are similar to the expected self-diffusion coefficients for liquid hydrocarbons.[114,115] The experimentally observed sharp decrease in the diffusivity for longer alkanes (C_8-C_{16}) is not observed from our calculations with either FF. Similar discrepancies have been previously observed for silicalite, and may arise due to the inability of the intramolecular bending and torsion parameters to correctly describe the confinement of the long alkane molecules. [98,116]As MIL-47(V) consists of large 1-D

pores, our results suggest that D_s is not a strong function of carbon chain length for short alkanes.

A decrease in the self-diffusion coefficient has been reported by Jobic et al.[113] at higher loadings of ethane, propane and butane in MIL-47(V). Similar to our previous approach, we calculated diffusivities for C_2-C_4 alkanes at multiple loadings (0.5-3.5 molecules/u.c.) using VDW-DF2 FF. The predicted ethane and butane self-diffusivities agree very well with the QENS measurements (Figure 3.13). However, our MD simulations overestimate propane diffusion at low loadings. The experimental measurements indicate that butane diffuses faster than propane, which has been described by a so-called "blowgun" effect.[113] This effect is not seen in our MD simulations using VDW-DF2 or DREIDING FF, where the diffusivity decreases going from ethane to butane over the entire range of alkane loadings.

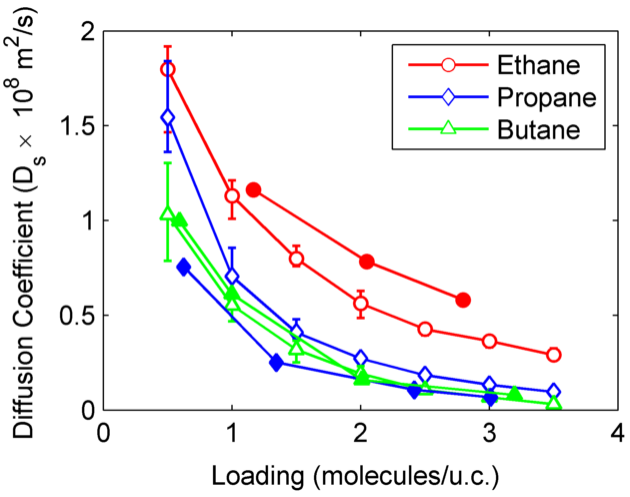

Figure 3.13. Self-diffusion coefficients calculated from NVT MD simulations at 300 K using VDW-DF2 FF for ethane (open red circles), propane (open blue diamonds) and butane (open green triangles). The error bars denote the range of D_s values obtained from 5 independent MD simulations. The experimental QENS measurements from Jobic et al.[113] are shown with filled symbols.

Having established that the DFT-derived VDW-DF2 force field successfully predicts the adsorption and diffusion of alkanes in MIL-47(V), we now focus on evaluating the transferability of our force field to the MIL-53 series. Since its first synthesis by Millange et al.,[17,117] the MIL-53 family of flexible MOFs has attracted attention due to its guest induced breathing behavior.[17,118,119] A number of experimental and modeling groups have studied the structural transitions in MIL-53(Al, Fe, Cr, Ga, Sc) upon the adsorption of H_2, CH_4, CO_2, H_2O and hydrocarbons.[17,100,119-123] These and related studies have been recently reviewed by Alhamami et al.[118] and Schneemann et al.[124] Even though a variety of techniques have been explored for modeling these materials,[124] our focus here is limited to studying the adsorption of short linear alkanes in MIL-53(Cr) and MIL-53(Fe) using the VDW-DF2 FF.

3.9. Alkane Adsorption in flexible MIL-53(Cr)

We will first discuss the breathing behavior in MIL-53(Cr) [97]. X-ray powder diffraction results and adsorption measurements[97,99] indicate a narrow pore (NP) to large pore (LP) structural transition in MIL-53(Cr) on adsorption of ethane, propane and butane (Figure C1). This transition is clearly seen as substeps in the experimental propane and butane adsorption isotherms (Figure C2), while the transition due to ethane is suggested from XRD results of Llewellyn et al.[99] The XRD results also suggest that the both LP and NP phases exist simultaneously over a significant pressure range.[99]

The predicted CBMC isotherms are obtained using the following procedure. We first optimize LP and NP structure for MIL-53(Cr) using DFT, based on experimentally reported cell parameters for ethane, propane and butane adsorption.[99] For both LP and NP structure corresponding to each alkane, we predict CBMC isotherms using the rigid

framework and the VDW-DF2 FF. The predicted adsorption data is then fit to a dual site Langmuir model. The final combined isotherms are obtained by directly using "phase mixture" model of Rosenbach et al. [97] for propane and butane. This model was derived from hybrid GCMC/MD simulations of the MIL-53(Cr) framework.[125] As a significant step in the ethane adsorption isotherm is not observed experimentally, we only report the LP adsorption isotherm. Details of DFT optimization, phase mixture model and dual site Langmuir fits are presented in Appendix C.

Figure 3.14 compares the experimentally reported adsorption isotherms for (a) ethane, (b) propane and (c) butane with the predicted CBMC isotherms using the aforementioned procedure. Figure 3.14 (a) indicates that the predicted ethane adsorption isotherm in the LP MIL-53(Cr) structure slightly overestimates (~0.15 mmol/g) the experimental data, though the shape of the isotherm is well predicted. By using the phase mixture model,[97] we obtain a good description of the transition region for butane but the saturation capacity is slightly overestimated (~0.1 mmol/g). For propane, the phase mixture model predicts a much sharper transition region than the experimental observations. However, the VDW-DF2 FF isotherm in the LP form is in very good agreement with the experimental data.

Overall, we can conclude that the VDW-DF2 FF reasonably predicts the transition region and the adsorption isotherms over the entire pressure range. The discrepancies noted in the predicted and the experimental adsorption isotherm may arise from simultaneous existence of LP and NP phase leading to continuous volume change on hydrocarbon adsorption.

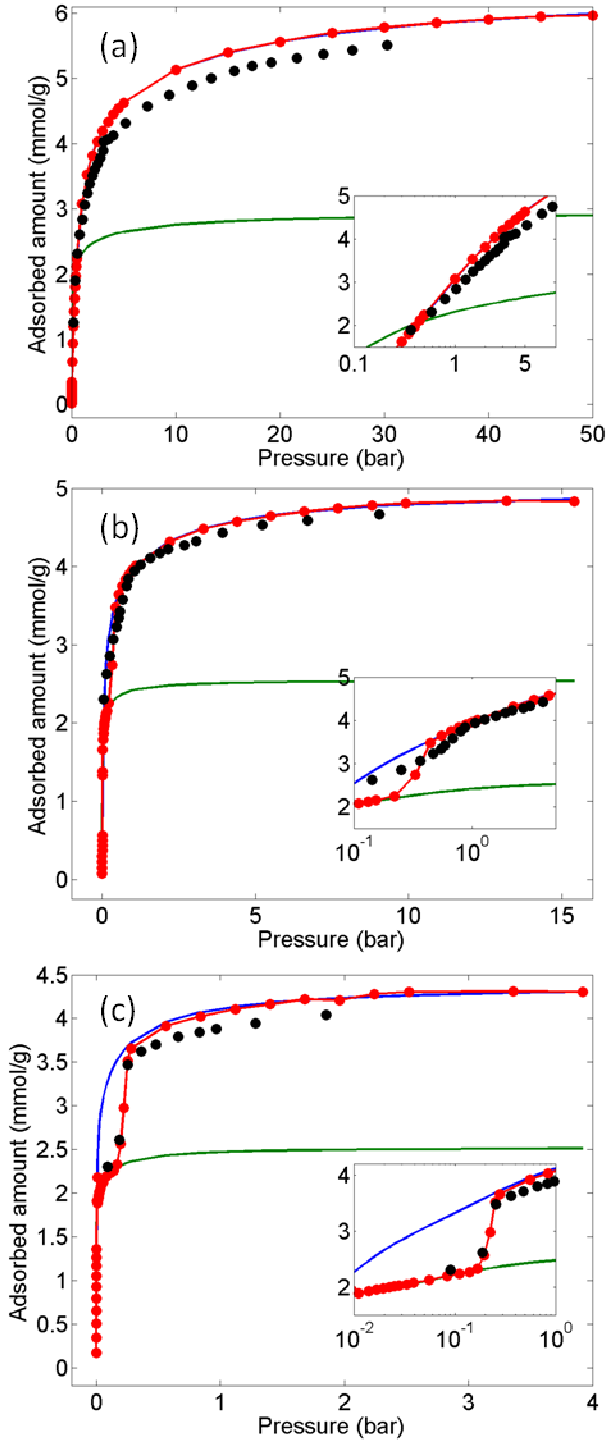

Figure 3.14. Adsorption isotherms for (a) ethane, (b) propane and (c) butane in MIL-53(Cr) at 303 K. The experimental data from Rosenbach et al. [97] (black circles) is compared to the CBMC predictions (red circles). The dual site Langmuir fits to the LP and NP CBMC adsorption isotherms are shown by the blue and green solid lines respectively. The inset in each figure shows the zoomed-in region close to the transition pressure.

3.10. Phase transitions in flexible MIL-53(Fe)

Given that the VDW-DF2 FF predictions for MIL-53(Cr) are in good agreement with experimental data, we now turn to studying the adsorption in the Fe version of MIL-53. Compared to the MIL-53(Cr) case, hydrocarbon adsorption in MIL-53(Fe) is further complicated by the existence of a two more phases in addition to the LP and the NP form.[100,126] These are denoted as very narrow pore form (VNP) and intermediate (INT) phases and are shown schematically in Figure D1.[100] In this section, we discuss the application of our force field to calculate the relative free energy differences for the experimentally observed phases of MIL-53(Fe) using OFAST.[127]

Llewellyn et al.[100] have measured the experimental adsorption isotherms of ethane, propane and butane in MIL-53(Fe) at 303 K (Figure D2). In contrast to the MIL-53(Cr) case, a guest-induced transition for all three alkanes is clearly observed. The complex adsorption behavior for the three alkanes and the phase transitions has been described in the original publication.[100]

The free energy differences of MIL-53(Al, Cr, Sc, Ga) analogues have been studied using DFT calculations and/or the OFAST approach for different adsorbates.[121,122,128,129] To the best of our knowledge, there have not been any computational studies for modeling hydrocarbon adsorption in MIL-53(Fe). As a "phase mixture" model[125] for MIL-53(Fe) has not been reported in the literature, we use the Osmotic Framework Adsorbed Solution Theory (OFAST) approach to describe the various transitions.[123]

The governing equation for the isothermal OFAST calculation is,

$$\Delta\Omega(P) = \Delta F_{host} - RT\int_0^P \left(\frac{\Delta N_{ads}(P)}{P} dP \right) \quad (3.4)$$

where $\Delta\Omega(P)$ is difference in the grand potential between two structures, ΔF_{host} is the host-host free energy difference and $N_{ads}(P)$ is the adsorption isotherm. The OFAST method uses the host-host free energy difference (ΔF_{host}) and an adsorption isotherm dependent solvation term (second term in Eq. 3.4) to predict the thermodynamically preferred phase at each adsorption condition. Alternatively, if the transition pressure is known from experimental isotherms, then we can obtain ΔF_{host} for the corresponding transition. The experimentally observed transitions pressures for ethane, propane and butane isotherms are summarized in Table D1. In the following section, we use the VDW-DF2 FF predicted adsorption isotherms and the experimental transition pressures to calculate the ΔF_{host} for VNP $\rightarrow$ INT $\rightarrow$ NP $\rightarrow$ LP transition.

Similar to the approach described for MIL-53(Cr), the following steps are used to predict ethane, propane and butane adsorption isotherms in MIL-53(Fe): (i) DFT optimization using the experimentally reported lattice parameters, (ii) CBMC simulations with the LP, NP and INT forms of MIL-53(Fe) (iii) Fitting CBMC results to the dual site Langmuir isotherms and (iv) OFAST method to obtain the final combined isotherms and calculate ΔF_{host}.

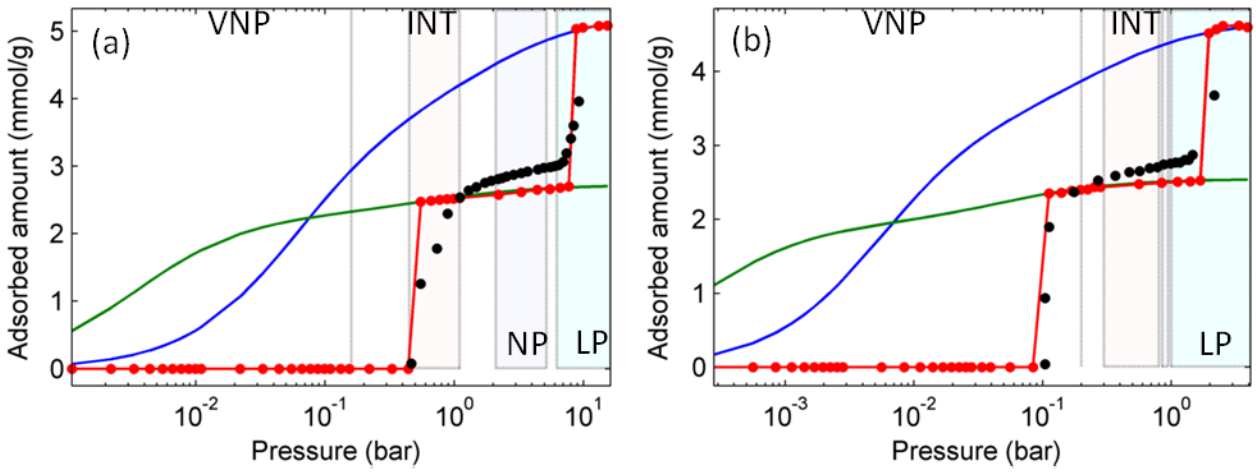

Figure 3.15. Adsorption isotherms for (a) propane and (b) butane in MIL-53(Fe) at 303 K. The experimental data from Llewellyn et al. [100] (black circles) is compared to the CBMC predictions (red circles). The dual site Langmuir fits to the LP and NP CBMC adsorption isotherms are shown by the blue and green solid lines respectively. The light colored regions indicate the experimentally observed dominant phase at different pressures from XRD measurements.

As discussed earlier, the OFAST approach necessitates *a priori* knowledge of ΔF_{host}. We use the, approach Coudert et al.[119], which relies on using the experimentally observed transition pressure and CBMC isotherms to estimate this value.

Figure 3.15 (a) and (b) shows the adsorption isotherms (black circles) for propane and butane, respectively, in MIL-53(Fe) at 303 K. The figure also shows the dual site Langmuir fit for the LP (blue lines) and NP (green lines) structures. For both the alkanes, no adsorption uptake is observed at very low pressures. Power XRD experiments[100] suggest the non-porous VNP to be the dominant structure at these pressures. As the pressure is increased, a transition is observed that results in an uptake corresponding to the NP form (green line) of MIL-53(Fe) for both propane and butane. These results imply that the free energy difference calculated from this transition is dominated by the VNP → NP transition. Encouragingly, the calculated free energy differences from the propane isotherm (-30.0 kJ/mol-u.c.) is similar to the butane value (-32.5 kJ/mol-u.c.).

As the pressure is increased further, a second step in the adsorption isotherm is observed for both propane and butane. Based on XRD results [100], this corresponds to the NP → LP transition and the calculated free energy difference is -6.12 kJ/mol-u.c. (from propane) and -6.59 kJ/mol-u.c. (from butane). As only one structure is predicted from OFAST at each pressure, the steps for the simulated isotherms are much sharper than the experimental data. In the actual material, the LP, NP and INT phase co-exist [100] and result in a smooth isotherm close to the transition pressure.

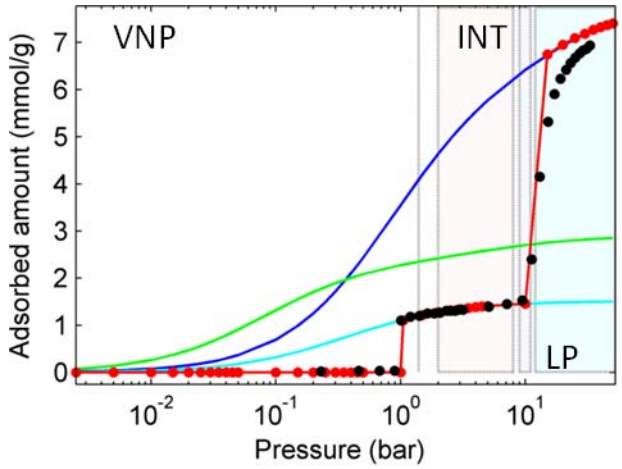

Figure 3.16. Adsorption isotherms for ethane in MIL-53(Fe) at 303 K. The experimental data from Llewellyn et al. [100] (black circles) is compared to the CBMC predictions (red circles). The dual site Langmuir fits to the LP and NP CBMC adsorption isotherms are shown by the blue and green solid lines respectively. The solid cyan line is the single site Langmuir fit to the INT part of the isotherm (1.0 bar < P < 9.4 bar). The light colored regions indicate the experimentally observed dominant phase at different pressures.

We now turn to describing the ethane adsorption isotherm using the OFAST approach. As with propane and butane, the near-zero uptake region at pressures less than 1 bar corresponds to the non-porous VNP phase. As the pressure is increased, we observe a first step corresponding to ~ 1.3 mmol/g, which is 50% of the first VNP → NP transition for propane (~2.7 mmol/g) and butane (~2.64 mmol/g) isotherm (refer Figure

D2). Compared to the NP structure, where all the pores are available for adsorption, 50% of the pores in INT structure of MIL-53(Fe) are closed (Figure D1). It is likely that the step corresponding to 1.33 mmol/g is dominated by INT phase. Moreover, this seems to be consistent with the power XRD results (Fig. 3.16) that indicate the presence of the INT phase. We conclude that unlike propane and butane isotherms (VNP $\rightarrow$NP transition), the first step in the ethane isotherm actually corresponds to the VNP $\rightarrow$ INT transition.

The CBMC isotherms using the VDW-DF2 force field predicts zero ethane uptake in the INT form of MIL-53(Fe) at all pressures. However, our DFT calculations for few ethane configurations indicates that large interaction energies (-35 kJ/mol). Further analysis of these configurations shows the ethane molecule to be highly confined small channels with largest cavity diameter of 3.1 Å. At such short distances, the united atom description of ethane fails at describing the energetics and zero uptakes are incorrectly predicted.

To circumvent this issue, we fit the isotherm corresponding to the INT phase (1.0 bar < P < 9.4 bar) to a single site Langmuir model (cyan solid line in Fig. 3.16) and repeat the OFAST calculations to obtain the free energy difference of -6.18 kJ/mol-u.c. corresponding to the VNP $\rightarrow$ INT. Since only a small region of the experimental data is used to fit the Langmuir isotherm, errors in the ΔF_{host} calculations are possible. Finally, by comparing the CMBC isotherm from the LP form (blue solid line in Fig. 3.16) with the experimental data, we can conclude that the second step observed at ~9.4 bar corresponds to the INT $\rightarrow$ LP transition with a free energy difference of -30.0 kJ/mol-u.c. These free energy differences can be represented by the energy level diagram shown in

Figure 3.17. The results indicate that the relative free energies calculated from ethane, propane and butane adsorption isotherms are consistent with each other.

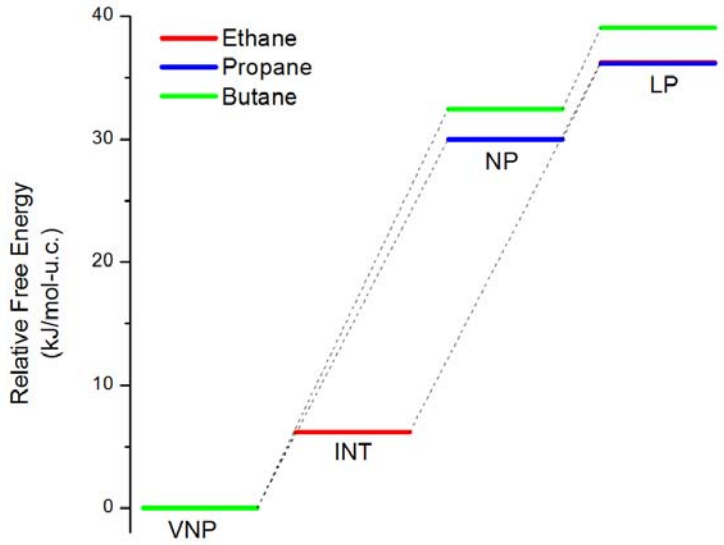

Figure 3.17. Relative free energy differences for the very narrow pore (VNP), intermediate (INT), narrow pore (NP) and large pore (LP) structures of MIL-53(Fe) from the ethane (red), propane (blue) and butane (green) isotherms.

3.11. Conclusions

In this Chapter, we have presented a general framework for developing *ab-initio* force field for adsorbate molecules in nanoporous structures using periodic DFT calculations. This approach has been illustrated for modeling the interactions of short and long alkanes in MIL-47(V) and good predictions of adsorption and diffusion properties are obtained. Our results suggest that even for simple systems such as adsorption of hydrocarbons in non-open metal site MOFs, the performance of generic force fields such as UFF and DREIDING can be improved using first-principles derived FFs. An advantage of using this approach is that the developed force fields are likely to be transferable across different adsorbates and can be used for studying related MOF materials. We believe that this approach would be an important step in evaluating and

improving the performance of generic force fields before systems that are more complex are considered.

CHAPTER 4

SCREENING OF COPPER OPEN METAL SITE MOFS FOR OLEFIN/PARAFFIN SEPARATIONS USING DENSITY FUNCTIONAL THEORY DERIVED FORCE FIELDS

In this chapter, we extend our previous force field development methodology for modeling adsorption of olefins and paraffins in Metal-Organic Frameworks containing copper open metal sites. By performing numerous single point energy calculations using Density Functional Theory (DFT), we develop a transferable force field that successfully predicts adsorption of alkanes and alkenes in CuBTC. This force field is then used for screening a variety materials for ethylene/ethane, propylene/ propane and hexene/hexane separations.

4.1. Introduction and Literature Review

Metal-Organic Frameworks have been widely studied for various applications such as separations and catalysis over the past decade.[68] One reason for the continuing interest in (MOFs) is the possibility of using a variety of linkers and metal centers for the synthesis. This clearly indicated by the increasing number of studies that describe the synthesis and characterization of MOF with novel ligands, metal nodes, topologies and chemical functionalities. Of the multitude of structures that have been previously reported and the new MOFs that are being continuously synthesized, it is a daunting challenge to identify a subset of MOFs with ideal properties for a given application. A thorough experimental investigation involving synthesis, activation, and characterization studies

will likely be limited to only a handful of structures. Moreover, single-component and binary adsorption isotherms at different temperatures are necessary to assess materials for many separations applications, which further limits the rate at which MOFs that can be experimentally studied in this context.

One way of making this process more efficient is to utilize computational modeling techniques to rapidly evaluate and study the separation properties of a large library of MOFs, and to use results from these calculations to guide experimental synthesis by identifying top performing candidates. This approach has been previously used for screening of MOFs for a various applications such as H_2 storage[130,131], CH_4 separations[132,133], carbon capture[81,82,134-136], SO_2/NO_x removal[137] and noble gas adsorption.[138] Further examples of MOF screening studies for other applications have been reviewed by Meek et al.[139]

Most of the computational screening studies that involve a large library of materials (> 100) have been limited to using off-the-shelf[84] force fields (FFs) for predicting the adsorption properties. For instance, early work by Haldoupis et al.[81] used the generic Universal Force Field (UFF)[84] force field to calculate CO_2/N_2 uptakes from Grand Canonical Monte Carlo[20] (GCMC) simulations. A similar approach was used by Wilmer et al.[82] to study methane uptake in > 137 000 hypothetical MOF structures. Another example is the use of the DREIDING[83] FF by Lin et al.[140] to study zeolitic imidazolate frameworks (ZIFs) for carbon capture. In these and similar studies, it is assumed that the generic force fields provided a reasonable description of the adsorbate-framework interactions. Even though the predictions from generic force fields are reasonable for simple systems, the performance of these approaches can be unsatisfactory

for systems that involve more complex interactions. For instance, generic force field do not accurately represent the interactions of CO_2[50,51,95,141,142], H_2O[85] and olefins[69,109,143] with MOFs that contain coordinatively unsaturated metal sites.

Considerable attention has been directed towards developing first principles force fields that allow for accurate representation of complex adsorbate-host interactions in nanoporous materials such as MOFs[50,51,85,95,141,142,144-146] and zeolites.[24,94] The available literature in this area has been recently reviewed by Fang et al.[89]

Related work in MOFs has been focused on describing interactions of H_2 [144,145], CO_2[50,51,95,141,142], CH_4[146] and H_2O[85] with open metal site MOFs using a*b-initio* force fields. Examples of quantum chemical cluster methods used for this application include coupled cluster (CCSD(T)/CBS) [21], 2nd order Moller-Plesset (MP2) [50,93,147] and Symmetry Adapted Perturbation Theory (SAPT) [148,149]. The high computational cost of these methods limits their applicability to studying relatively small systems.

An alternate approach is to perform quantum chemistry calculations using the periodic structure of the MOF to obtain the force field. We have previously used this approach to derive force fields for CO_2 adsorption in zeolites[24,89,94] and for hydrocarbon adsorption in MIL-47(V). Our results suggest that periodic Density Functional Theory (DFT) provides a reasonable trade-off between accuracy and computational cost for modeling these nanoporous materials.

Force field development studies for olefin/ paraffin adsorption in open metal site MOFs have received less attention. Many of the previous studies in this area have used empirical corrections to the generic force fields to predict adsorption of C_2 and C_3 hydrocarbons in CuBTC (HKUST-1).[69,87,88,109,143,150] Examples of these modifications

include adjusting the adsorbate charges[150,151] and increasing the Cu-adsorbate Lennard-Jones parameter [86,152] to better fit the experimental data.A notable exception is the study by Fischer et al.,[69,109,153] who used cluster DFT calculations to develop a force field for propylene adsorption in CuBTC. This force field gave good agreement with the experimental ethylene and propylene isotherms at various temperatures, but the transferability to other Cu open metal site MOFs was not explored.

Assuming that reliable force fields are available, molecular simulations provide an ideal tool for rapidly studying large sets of materials for a target separation. A significant number of the MOF screening studies have focused on carbon capture or on gas storage applications. Hydrocarbon separations involving olefins and paraffins are of primary importance in the chemical industry[68]. Typically, these energy intensive separations are performed using distillation, though alternate adsorption-based processes using zeolties have been explored.[154-156] The presence of open metal sites in MOFs allows for preferential adsorption of olefins, leading to high olefin/paraffin selectivities.[2,69,75,143] The development of MOF adsorbents with appropriate properties may lead to more energy efficient separations and considerable economic savings. To the best of our knowledge, no computational studies have systematically evaluated a large library of open metal site MOFs for olefin/paraffin separations. Due to the specific nature of the interactions of the olefins with the open metal sites, generic force fields are unsuitable for this study.[95,109]

In this Chapter we develop transferable force fields that can accurately predict the adsorption of olefins and paraffins by copper open metal site (OMS) MOFs using periodic DFT calculations. Since, the adsorption properties of CuBTC have been well

studied using both computational and experimental techniques, we choose CuBTC as the model system for force field development. We also show that the force fields developed for CuBTC are transferable to other MOFs, and can be used to screen through a library of MOFs to identify top performing MOFs for various olefin/paraffin separations.

The remaining part of this Section is organized as follows: An overview of our force field development algorithm and the computational details are first presented in Section 4.2. Section 4.3 and 4.4 describes the derivation of force field for C_2 and C_3 hydrocarbons from periodic DFT calculations for CuBTC. The transferability of the force field to other Cu containing MOFs is discussed in Section 4.5. Next, we discuss our algorithm to efficiently identify open metal site MOFs from a large library of structures (Section 4.5). Finally, in section 4.6, we present the screening results for propylene/propane separations using different processes.

4.2. Computational Methods and Force Field Development Algorithm

4.2.1. Overview

The force field development approach used here is similar to the one used in Chapter 3. We first calculate the interaction energies for a few (< 150) preferred adsorbate configurations using Density Functional Theory (DFT). These interaction energies are fit to a classical potential form to obtain an initial version of the force field. We use the new FF parameters in a Grand Canonical Monte Carlo (GCMC) simulation to generate isotherms and a larger set (300 - 600) of adsorbate configurations. Again, DFT interaction energies are obtained for the new configurations and the FF parameters are recalculated using a least-square fit to yield the final, DFT-consistent version of the force

field. The calculation details for each step of the FF development algorithm are discussed below.

4.2.2. Structure optimization

The initial crystal structure for CuBTC is obtained from original synthesis report by Chui et a.[10] The DFT structure optimization of the 156-atom primitive, rhombohedral unit cell was performed with the Vienna ab-initio Simulation Package (VASP) using the GGA functional of Perdew, Burke and Ernzerhof [102] with Grimme's D2[103] corrections to include the dispersion interactions. A plane wave cutoff of 700 eV is used to optimize the lattice constants, while the internal atomic positions are obtained at a lower 400 eV cutoff. The energy minimization is terminated when the individual atomic forces are less than 0.03 eV/Å. To reduce the computational cost, the DFT calculations were performed at the Γ-point. The dicopper metal cluster in CuBTC is known to be anti-ferromagnetic[157] and periodic calculations are initialized with the appropriate spin ordering. The PBE-D2 optimized lattice constants are in good agreement with experimental data.

4.2.3. Single point energy DFT calculations

Our FF development approach is based on fitting the interaction energies obtained from periodic DFT calculations to a classical potential form. The interaction energy of the adsorbate molecule is defined as

$$E_{interaction} = E_{MOF+ads} - E_{MOF} - E_{ads} \qquad (4.1)$$

where E_{MOF} and E_{ads} refer to the DFT energies of the CuBTC framework and the

adsorbate molecule, respectively, while $E_{MOF+ads}$ is the DFT energy of the adsorbed hydrocarbon/MOF system.

Within DFT, the electron exchange-correlation can be described by different functionals that may result in different interaction energies for the given configuration of the adsorbate. Our previous results (Chapter 3) for hydrocarbon adsorption in MIL-47(V) suggest that FFs derived from the vdW-DF2 functional of Langreth and Lundqvist[107] give better agreement with experimental isotherms than the PBE-D2 [102,103] method. Thus, in the following sections, we only use the vdW-DF2 method for force field development.

4.2.4. GCMC Simulations

All GCMC simulations were performed within the RASPA simulation code developed by Dubbeldam and co-workers.[108] For adsorption simulations involving longer hydrocarbons configurational-bias Monte Carlo (CBMC)[105] was employed. A 2×2×2 supercell of CuBTC was used and the pairwise interaction potentials were truncated at a spherical cutoff of 13.0 Å. Analytical tail corrections were included to model the long-range dispersion interactions. The CBMC calculations were carefully equilibrated using at least 100,000 cycles, and production runs of 400,000 cycles were used for measuring the macroscopic properties.

To model the adsorption of hydrocarbons in CuBTC, interaction parameters for the C, O, H and Cu framework atoms are required. Previous results have shown that generic force fields are unsuitable for modeling the Cu atoms and better representation of the OMS is necessary.[109] As the objective of this work is to eventually use the Cu OMS force field to predict adsorption in other Cu containing MOFs, we use the generic

DREIDING[83] FF to represent the C, H and O atoms in CuBTC. As discussed later, the Cu interaction parameters are obtained by fitting the DFT interaction energies.

The fluid-fluid interactions in our calculations are modeled using the united atom TraPPE force field[106] for hydrocarbons. The TraPPE unite atom description of alkanes and alkenes does not include point charges on the adsorbate atoms and only considers Lennard-Jones terms to model the intermolecular dispersion interactions. To be consistent with the TraPPE FF, we do not explicitly consider any Coulombic interactions in our calculations. The cross interaction parameters for the framework and the hydrocarbon molecules are obtained from the Lorentz-Berthelot mixing rules.

In addition to the TraPPE FF, an alternate united atom alkane force field suggested by Dubbeldam et al.[158] can be used for predicting adsorption in nanoporous materials (denoted as Dubbeldam FF). It is important to note that the TraPPE force field was obtained by fitting to experimental fluid phase properties[106], while the Dubbeldam FF was fit to reproduce the experimental hydrocarbon adsorption isotherms in zeolites[158].

Given that the TraPPE FF accurately reproduces the experimental vapor-liquid equilibria, liquid densities, equation of states and other fluid phase properties for a wide range of alkanes,[106] we use TraPPE FF for the force field development. Details of the force field parameters for the DREIDING, TraPPE and Dubbeldam FF are presented in Table E1-E3.

4.3. Force Field Development for Ethane and Ethylene

We will first discuss the application of our force field development methodology for modeling ethylene and ethane adsorption in CuBTC.

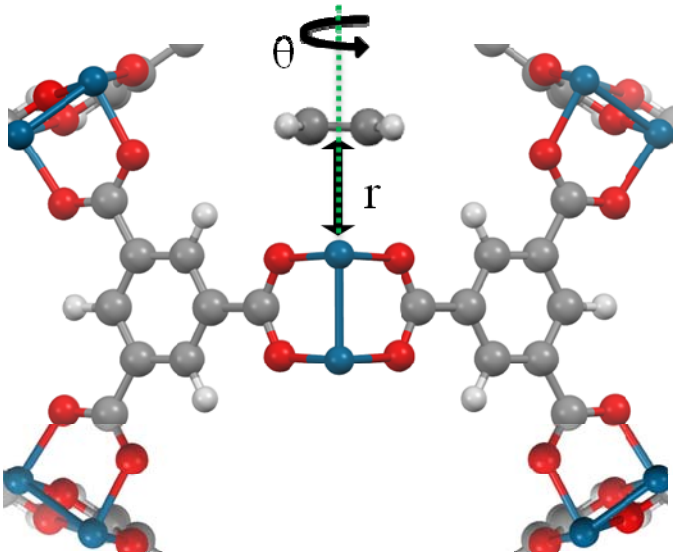

Figure 4.1 Orientations used for calculating the interaction energies of ethylene with the periodic CuBTC structure at different values of r and θ. The dotted green line represents the direction of the Cu-Cu vector. The ethylene molecule is place on top of the Cu atom plane of the molecule is normal to the Cu-Cu direction. The color scheme used is C (grey), O (red), H (white) and Cu (blue).

4.3.1. Initial configurations

Multiple configurations of the ethylene molecule are generated in the periodic CuBTC structure to calculate the total DFT energy (Fig. 4.1). To maximize the interaction of the pi bond with the Cu OMS, the ethylene molecule is placed directly above the Cu atom using the following constraints: (1) the center of the C=C double bond lies in the direction of the Cu-Cu vector (dotted green line), (2) the C=C double bond is perpendicular to the Cu-Cu vector and (3) the plane of the ethylene molecule is to be normal to the direction of the Cu-Cu vector. The total energy of the system is calculated at 13 different distances (denoted as r, Fig. 4.1) of ethylene from the Cu atom ranging from 2 to 5 Å. To better describe the interactions with the Cu OMS, 10 additional configurations are generated at each r distance by randomly rotating the adsorbate about the Cu-Cu axis (θ, Fig. 4.1). For generating the ethane potential energy surface (PES), an

additional random rotation about the C-C single bond is included to sample a wider configuration space arising due to the positions of the H atoms.

4.3.2. FF Iteration 1: Fitting Cu OMS/adsorbate interactions

The interaction energies for 130 configurations of ethylene and ethane are obtained using the DFT procedure outlined in Section 4.3.1. Of the various configurations sampled at each distance, Figure 4.2 shows the minimum interaction energies at a given r for ethane and ethylene calculated using the vdW-DF2 functional.

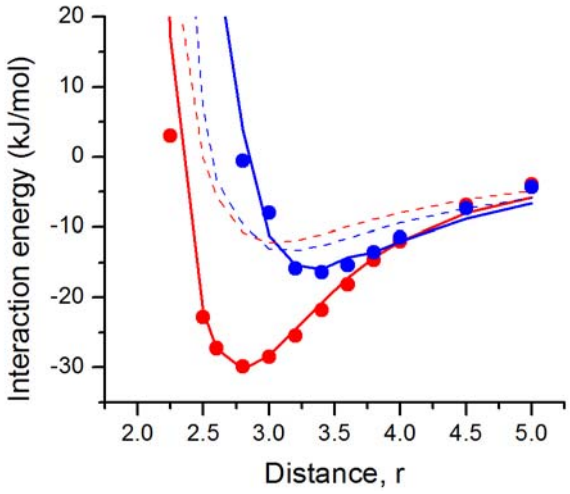

Figure 4.2. Interaction energies for initial configurations of ethane (blue) and ethylene (red) in CuBTC calculated using vdW-DF2 DFT method (filled circles) and the fitted force field (solid lines). The dotted lines represent the contributions from the generic DREIDING FF for C, H and O interactions.

From the DFT data in Fig. 4.2, the most favorable configuration for ethylene is ~2.8 Å from the Cu atom with an interaction energy of -29.9 kJ/mol. This interaction has been previously attributed to the pi-electron donation to the empty vacant p-orbital of the metal and d-orbital back-bonding from the Cu atom. Compared to the ethylene results,

the ethane interactions are considerably weaker (-16.4 kJ/mol) and are dominated by the dispersion interactions.

For the ethane and ethylene configurations presented in Fig. 4.2, we also calculated the DREIDING/TraPPE FF contributions only including the interactions of the C, H and O atoms with the adsorbates (dotted lines). The similar nature of the ethane and ethylene curves suggests that DREIDING/TraPPE FF gives a comparable description of the non Cu atoms for both adsorbates. Comparing the ethylene DFT data with the generic component indicates that the Cu-adsorbate interactions are dominant, and a correct description of the Cu atom is required to reproduce the vdW-DF2 results. We can also conclude that a relatively smaller Cu interaction is required to correctly describe the ethane DFT data.

As discussed in Section 4.2.3, we assume that the DFT interaction energy can be decomposed into two parts,

$$E_{DFT} = E_{generic,non-Cu} + E_{Cu-ads} \tag{4.2}$$

where E_{DFT} is the total DFT interaction energy, $E_{generic,non-Cu}$ is the contribution of the non-Cu atoms (H, C and O) calculated from DREIDING/TraPPE FF and E_{Cu-ads} is the interaction energy from the Cu OMS with the adsorbate.

Using the DFT interaction energy and the generic FF contributions, we calculate E_{Cu-ads} required to reproduce the DFT data. This is then fit to a pairwise Morse potential,

$$U = D_0\left[\exp\left(\alpha\left(1-\frac{r}{\rho}\right)\right) - 2\exp\left(\frac{\alpha}{2}\left(1-\frac{r}{\rho}\right)\right)\right] \tag{4.3}$$

where D_0 is energy minimum, ρ is the distance corresponding to the energy minimum and α indicates the width of the potential well. We chose the Morse potential as, the three fitting parameters (D_0, ρandα) allow it to be more flexible than the 2 parameter Lennard-Jones potential.

Table 4.1. Fitted Morse parameters for the interaction of the Cu OMS with the ethane and ethylene united atoms in CuBTC.

Framework atom	Adsorbate united atom	D_0 (kJ/mol)	ρ (Å)	α
Cu	CH3_sp3	1.54	11.93	3.40
	CH2_sp2	10.46	8.83	2.64

The fitted Morse parameters for ethane and ethylene are presented in Table 4.1. The total interaction energies including the fitted Morse potential (solid lines, Fig. 4.2) for ethane and ethylene agree well with the DFT data indicating that the Morse potential is appropriate for this system. This version of the force field that is obtained by fitting vdW-DF2 interaction energies to the Morse potential is denoted as VDW-DF2 FF (Iteration 1). Note that in this approach the framework H, C and O interactions are described by generic DREIDING FF.

The next section will discuss the performance of the generic and DFT-derived for predicting adsorption properties in CuBTC using GCMC simulations.

4.3.3. GCMC simulations

We begin the discussion by evaluating the performance of the generic FFs for ethane and ethylene adsorption. The experimental pore volume of the CuBTC sample

used by Want et al.[151] (0.658 cc/g) and Jorge et al.[143] (0.71 cc/g) is lower than the calculated pore volume for the ideal CuBTC material (0.84 cc/g) used in our GCMC simulations. To compare the GCMC isotherms with the experimental measurements, we scale up the experimental isotherms based on the ratio of the pore volumes of the ideal and the experimental crystal.[109]

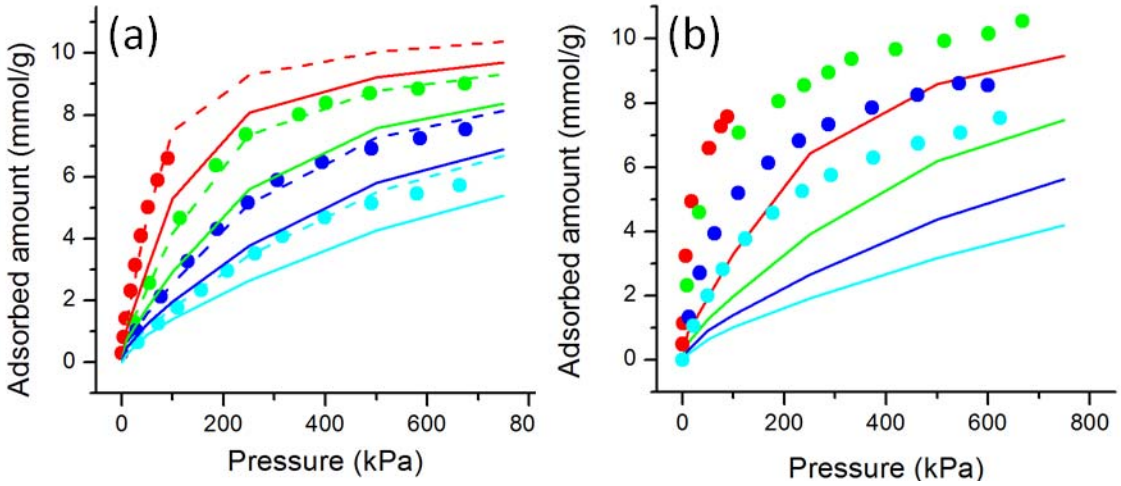

Figure 4.3. GCMC predicted adsorption isotherms for (a) ethane and (b) ethylene in CuBTC using the DREIDING FF for the framework atoms and the TraPPE FF (solid lines) for the adsorbates at 295 K (red), 323 K (green), 348 K (blue) and 373 K (cyan). The predictions using DREIDING FF and Dubbeldam FF for ethane are shown by the dotted lines in (a). The scaled experimental adsorption isotherms from Wang et al.[151] at 295 K (red) and Jorge et al.[143] at 323 K (green), 348 K (blue) and 373 K(cyan) are shown by filled circles.

Figure 4.3 (a) and (b) compares the predicted isotherms for ethane and ethylene in CuBTC with the scaled experimental data from Wang et al.[151] and Jorge et al.[143] at various temperatures. Compared to the experimental data, the DREIDING/TraPPE FF (solid lines) underestimates both ethane and ethylene isotherms. As the correct description of the Cu OMS is more important for ethylene adsorption, the disagreement of the predicted ethylene isotherms is more severe. Figure 4.3 (a) also shows that the

ethane isotherms from DREIDING/Dubbeldam FF (dotted lines) are in good agreement with experimental data. However, since the Dubbeldam FF is not parameterized to reproduce the ethane/ethane interactions, it is unclear if the fluid phase is being modeled correctly.

The ethane and ethylene adsorption isotherms using the VDW-DF2 (Iteration 1) FF are shown in Figure 4.4. Note that the fluid-fluid interactions are represented by the TraPPE FF. Compared to the DREIDING/TraPPE FF results, the predictions for both ethane and ethylene are significantly improved when VDW-DF2 FF is used. The GCMC predictions for ethane are in good agreement with the experimental isotherms at 295, 323 and 348 K while, a slight overestimation at 373 K is observed at higher pressures.

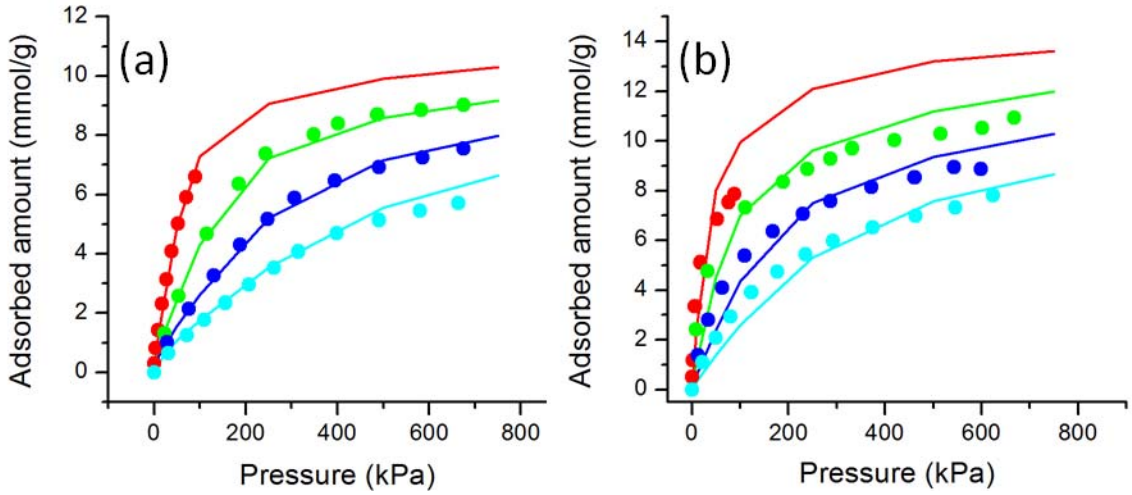

Figure 4.4. GCMC predicted adsorption isotherms for (a) ethane and (b) ethylene in CuBTC using the VDW-DF2 (Iteration 1) FF for the framework atoms and the TraPPE FF (solid lines) for the adsorbates at 295 K (red), 323 K (green), 348 K (blue) and 373 K (cyan). The scaled experimental adsorption isotherms from Wang et al.[151] at 295 K (red) and Jorge et al.[143] at 323 K (green), 348 K (blue) and 373 K(cyan) are shown by filled circles.

Figure 4.4 (b) shows that the ethylene predictions are significantly improved when VDW-DF2 FF is used. Reasonable agreement with the scaled experimental

measurements is observed at lower partial pressures and a slight overprediction is seen at the higher pressures. The deviation is more significant for the 295 K data of Wang et al.[2] In this case, the experimental data at 295 K approaches the 323 K isotherm at ~88 kPa, which may indicate incomplete equilibration at the lower temperature.[143] Despite these deviations from the scaled experimental data, using the DFT-derived force fields substantially improves the quality of the predictions.

4.3.4. FF Iteration 2 for ethane

The previous results indicate that the predictions from the VDW-DF2 (Iteration 1) FF give good agreement with the experimental ethane and ethylene isotherms. This version of the force field was obtained by only considering a limited set of favorable orientations of the adsorbate. For the force field to be truly consistent with DFT, we need to ensure that the DFT interaction energies for other configurations are also reproduced.

Similar to our previous work, we carried out GCMC simulations (1 bar and 295 K) using the Iteration 1 FF to generate a new set of configurations for ethane and ethylene. For these new configurations, periodic DFT calculations are performed to obtain the vdW-DF2 interaction energies. As the TraPPE hydrocarbon model only defines the CH3_sp3 and CH2_sp2 united atoms, it is necessary to add the appropriate hydrogen atoms prior to the DFT calculation.

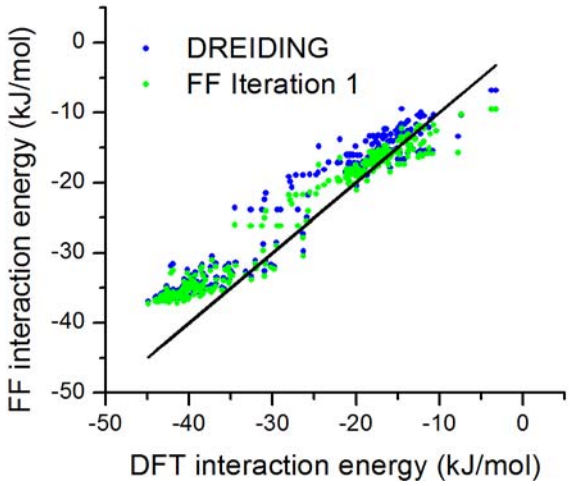

Figure 4.5. Comparison of the interaction energies calculated from vdW-DF2 DFT method with the DREIDING FF (blue) and VDW-DF2 (Iteration 1) FF (green) for 300 configuration of ethane in CuBTC.

Figure 4.5 compares the interaction energies for 300 configurations of ethane in CuBTC calculated using the vdW-DF2 method with the DREIDING FF (blue) and the Iteration 1 FF (green). The mean absolute deviation (MAD) for the DREIDING FF (4.12 kJ/mol) is higher than the MAD for Iteration 1 FF (2.9 kJ/mol), indicating that the Iteration 1 FF reproduces the DFT interaction energies significantly better than DREIDING.

Using the vdW-DF2 interaction energies for the new configurations, we refit the Morse potential parameters for ethane to obtain the 2nd iteration of the VDW-DF2 FF. On using this force field, the MAD decreases to ~2.4 kJ/mol, but a significant difference in the GCMC predicted isotherms is not seen. These results suggest that performing the 2nd iteration did not significantly improve the capability of the FF to describe the DFT data for ethane. Nevertheless, this approach validates the reliability of the Iteration 1 FF for predicting interaction energies of configurations that were not initially included in Section 4.3.1.

Figure 4.5 also shows a systematic underestimation of ~5 kJ/mol for low energy configurations for ethane for both the FFs. This discrepancy is also seen for ethylene and will be discussed later.

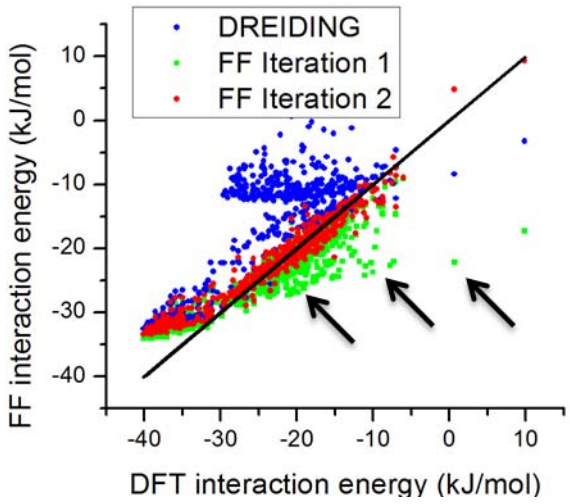

Figure 4.6. Comparison of the interaction energies calculated from vdW-DF2 DFT method with the DREIDING FF (blue), VDW-DF2 (Iteration 1) FF (green) and VDW-DF2 (Iteration 2) FF (red) for 600 configuration of ethylene in CuBTC. The arrows indicate some of the configurations were the Iteration 1 predicted energies are more negative than the vdW-DF2 predictions.

4.3.5. FF Iteration 2 for ethylene

Similar calculations are performed for ethylene and comparison of the DFT interaction energies with the DREIDING FF (blue) and Iteration 1 FF (green) is presented in Figure 4.6. Clearly, the DREIDING FF fails at predicting the vdW-DF2 interaction energies and a significant disagreement (MAD = 7.9 kJ/mol) is seen. Compared to the DREIDING FF, a significantly improved prediction of DFT energies is observed for the Iteration 1 FF (MAD = 3.2 kJ/mol). However, for a number of configurations (black arrows, Fig. 4.6) the FF predicted energies are more negative than

the vdW-DF2 predictions. In many of the cases, the deviations are larger than 10 kJ/mol indicating that the predictions from Iteration 1 FF are unsatisfactory.

Further analysis of these configurations suggests that the deviation occurs due to pairwise potential used for interaction of the CH2_sp2 united atom with the Cu OMS, and the orientation of the ethylene molecule.

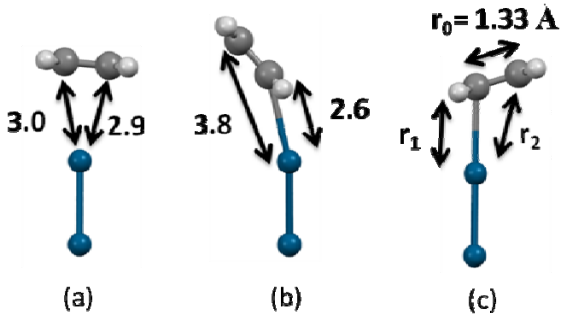

Figure 4.7. (a) and (b) Examples of ethylene configurations in CuBTC obtained from GCMC simulations at 295 K and 1 bar, and (c) notations used in Eq. 4.4. Only the Cu dimer closest to ethylene is shown for clarity. The color scheme used is C (grey), O (red), H (white) and Cu (blue).

Table 4.2. Interaction energies for two ethylene configurations in CuBTC shown in Fig. 4.7 (a) and (b) calculated using vdW-DF2 and two iterations of the VDW-DF2 FF

Interaction Energy (kJ/mol)	**Configuration (a)**	**Configuration (b)**
vdW-DF2 (E_{DFT})	-29.1	9.8
Iteration 1 FF	-28.9	-17.0
Iteration 2 FF	-29.1 (E_{orient} = +0.2)	8.1 (E_{orient} = +25.1)

Figure 4.7 shows two ethylene configurations obtained from GCMC simulations and their relative positions to the closest Cu OMS. The interaction energies calculated from vdW-DF2 and VDW-DF2 FF are shown in Table 4.2. For configuration shown in

Fig. 4.7 (a), the two C atoms of ethylene are essentially equidistant (~2.9 Å) from the closest Cu atom. This orientation is similar to the initial configurations used in Section 4.3.1 for ethylene, and allows for very favorable interaction of the pi bond with the Cu OMS. Subsequently, the interaction energies predicted from vdW-DF2 is similar the VDW-DF2 FF value. Conversely, in (b), ethylene is tilted (r_1=2.6 Å and r_2=3.8 Å) and DFT yields an unfavorable interaction (E_{DFT}=9.8 kJ/mol) with the framework. Even though the minimum adsorbate distance remains the same in (a) and (b), favorable pi-bond/Cu OMS interaction is not possible in (b) due to the orientation of the molecule. As a pairwise description of the FF only considers the individual distances of the C atoms with the Cu OMS (r_1 and r_2), an interaction energy of -17.0 kJ/mol is predicted with the VDW-DF2 FF. In this case, both r_1 are r_2 are close enough to the Cu OMS to have a favorable interaction based on the fitted Morse potential for CH2_sp2/Cu parameters (Table 4.1).

Similar analysis of the individual r_1 and r_2 distances and comparison of the interaction energies for 600 ethylene configuration suggest that an additional orientation dependent term is required to correctly account for this phenomenon (denoted E_{orient}). Since the orientation of the pi-bond is most important for configurations close the Cu atom, the correction function should decay to small values away from the Cu atom. Also, for ethylene orientation that are on top of the Cu atom (i.e. $r_1 - r_2 = 0$), the E_{orient} value must rapidly approach zero. Further analysis (Appendix E) indicates that a a nested exponential function

$$E_{orient} = 1 - \exp\left[A \cdot \exp\left(-B \cdot r_1\right) \cdot \left(\frac{r_1 - r_2}{r_0} \right) \right] \qquad (4.4)$$

is suitable for describing the decaying nature of the required correction term. In Eq. 4.4, r_1 and r_2 are C-Cu distances, r_0 is the C-C bond length for ethylene (1.33 Å), and A and B are fitting parameters to be calculated. Note that the orientation dependent term is a 3-body interaction that depends the positions of the two ethylene C atoms relative to the framework Cu atoms.

Using the difference in the interaction energies calculated from vdW-DF2 and VDW-DF2 (Iteration 1) FF, parameters A and B are determined and the fitting results are shown in Table 4.3. This version of the ethylene FF that includes the orientation dependent energy term is denoted as VDW-DF2 (Iteration 2) FF.

Table 4.3. Fitting parameters for the orientation dependent term, E_{orient} for ethylene adsorption in CuBTC.[#]

	A (kJ/mol)	**B (Å^{-1})**
Ethylene	44.4772	0.9803

[#] Morse potential parameters to be used with Iteration 2 FF are same as the Iteration 1 FF and are provided in Table 4.1.

Table 4.2 shows that the interaction energies for two representative configurations calculated using the Iteration 2 FF are in good agreement with the vdW-DF2 data. The energy penalty term (E_{orient}) for configuration (b) accounts for the tilted orientation of the ethylene molecule and makes the total interaction energy unfavorable. In contrast, E_{orient} for configuration (a) is small as r_1 and r_2 are similar.

Figure 4.6 shows that the interaction energies calculated using VDW-DF2 (Iteration 2) FF (red circles) are in much better agreement (MAD = 2.3 kJ/mol) with the vdW-DF2 predictions than the Iteration 1 FF (MAD = 3.2 kJ/mol).

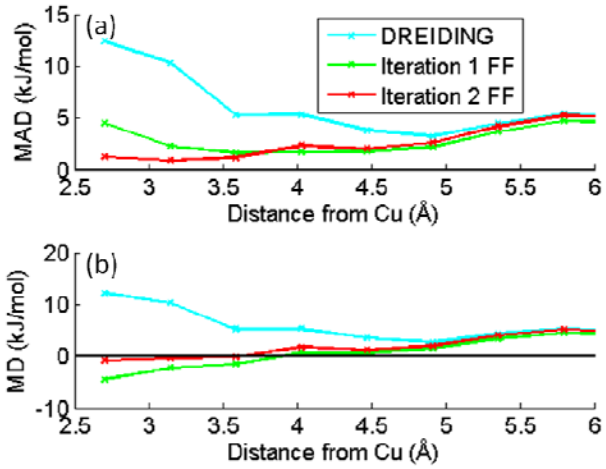

Figure 4.8 (a) Mean Absolute Deviation (MAD) and (b) Mean Deviation (MD) as a function of distance obtained from DREIDING FF (cyan), Iteration 1 FF (green) and Iteration 2 FF (red) compared to the vdW-DF2 for 600 configurations of ethylene in CuBTC.

Figure 4.8 (a) and (b) compares the MAD and MD for DREIDING, Iteration 1 and Iteration 2 FF as a function of the distance from the Cu OMS. As discussed previously, the DREIDING FF (cyan) fails at predicting the interaction energies close to the Cu OMS (MAD = 12 kJ/mol). For distances shorter than 4.5 Å, the MAD for Iteration 2 FF is less than 2 kJ/mol, while the MD close to zero. This is a significant improvement over the Iteration 1 FF where MAD of ~4 kJ/mol is seen for the same configurations. These results indicate that including the orientation dependent term considerably improved the quality of VDW-DF2 FF for the important configurations close to the Cu atom. While it is true that including more parameters in the force field necessarily

reduces the MAD, our data indicates that the functional forms chosen above are useful because they correctly capture the characteristics of the underlying interactions.

We now turn to addressing the systematic deviations previously observed in Fig. 4.6 for ethylene adsorption in CuBTC for all three FFs. This discrepancy is also seen from the Mean Deviation data in Figure 4.8 (b) for larger ethylene-Cu distances (5 - 6 Å). Analysis of these configurations shows that in essentially all cases where the interaction energies of more negative than -30.0 kJ/mol, the ethylene molecule is in the small octahedral pockets of CuBTC. In these configurations, the adsorbate/Cu distances are > 5 Å. As a result, the interactions with Cu atoms are small and the DREIDING FF that was used in all the calculations above for C, H and O atoms dominates the total interaction energy. For these confined hydrocarbon configurations, the DREIDING FF underestimates the interaction energy by ~5 kJ/mol, resulting in the deviations observed earlier.

One approach for resolving this discrepancy would be to re-parameterize the DREIDING FF for these confined hydrocarbon configurations. As the goal of this work was to parameterize the Cu OMS interactions without altering the DREIDING FF, we do not explore this issue further.

Notwithstanding the small shortcoming identified previously, we now show that inclusion of the orientation dependent term (Iteration 2) provides a more realistic description of ethylene adsorption in CuBTC compared to the Iteration 1 FF. We first discuss the ethylene adsorption isotherms obtained from the two versions of the FF. Typically, 3-body adsorbate/ framework integrations are not included in the common GCMC codes and custom modification to the RASPA simulation code was required.

Specifically, the Monte Carlo scheme and the biasing factors were modified to incorporate E_{orient} calculation while performing the translation, random translation, rotation, identity swap and the insertion/deletion moves.

Similar to the previous ethane results, we find that the ethylene adsorption isotherms calculated from Iteration 1 and Iteration 2 FFs are close to each other. However, careful analysis of the GCMC configurations reveal important differences in the adsorption characteristics of the two force fields. For both FFs, we used GCMC simulations at 295 K and 1 bar to obtain 5000 configurations of ethylene in CuBTC. The angle,θ formed between the direction of the C=C double bond and the vector connecting the Cu atom to the center of mass (COM) of ethylene is presented in Figure 4.9.

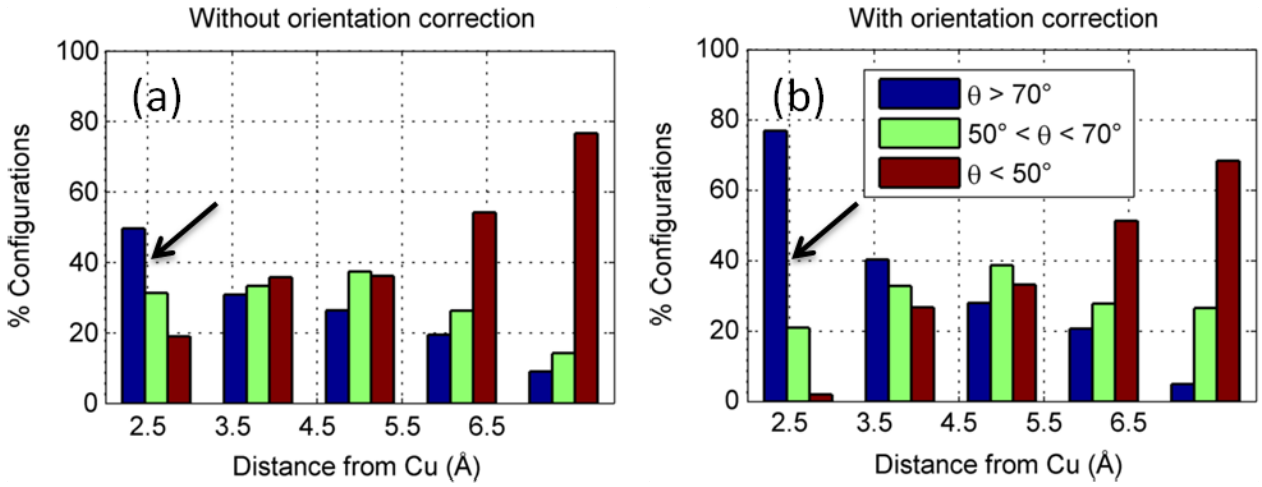

Figure 4.9 Angle formed between the double bond of the ethylene molecule and the vector from the nearest Cu atom to the COM of ethylene as a function of distance

Based on our previous discussion, the favorable configuration of ethylene is on top of the Cu atom and will result in θ = 90° close to Cu. At distances farther away from the Cu atom, the ethylene molecule will be more or less randomly oriented. At realistic pressures, a given adsorbate molecule will be affected by the thermal motions of the

surrounding molecules. For the following analysis, we consider an adsorbate molecule with θ > 70° to be 'flat' relative to the Cu atom and to have a favorable interaction of the pi-bond with the Cu OMS.

Figure 4.9 shows the distribution of the angle θ as a function of distance from using (a) Iteration 1 and (b) Iteration 2 force field. Our results show that at distances close to the Cu atom (< 3 Å, black arrows), only ~50% of ethylene molecules form an angle θ > 70°. On the other hand, when the orientation correction term is included (Fig. 4.9 (b)), close to 80% of the ethylene configurations are now 'flat' relative to the Cu atom. For the configurations at longer distances from Cu, the influence E_{orient} is not significant; suggesting that including the orientation term provides a more realistic description of the adsorbate orientations.

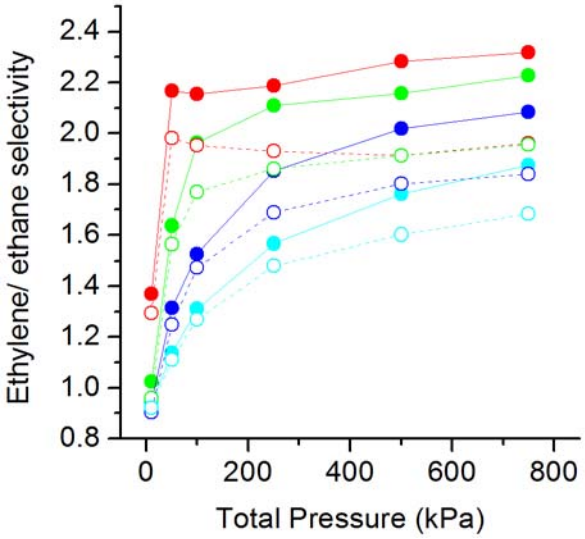

Figure 4.10 Selectivity calculated from GCMC simulations of equimolar ethylene/ethane mixtures in CuBTC using the Iteration 1 (empty circles) and Iteration 2 (filled circles) of the VDW-DF2 FF at 295 K (red), 323 K (green), 348 K (blue) and 373 K (cyan).

To further investigate the effect of the including the orientation dependent term, we simulated the adsorption of an equimolar mixture of ethylene and ethane in CuBTC at various pressure and temperatures. The selectivity is defined as

$$S = \frac{x_1 / x_2}{y_1 / y_2} \tag{4.5}$$

where, x_i and y_i are the mole fractions of the individual components in the adsorbed and the vapor phase.

From Figure 4.10, at low pressures the ethylene/ethane selectivity is close to 1, as the adsorption preferentially occurs in the non-selective octahedral cages. As the pressure is increased, the selectivity calculated from Iteration 2 FF increases to 2.3 (1.9) at 295 K (373 K). Comparing the two iterations of the FF, we see that the Iteration 2 FF always predicts a slightly higher ethylene/ ethane selectivity than the Iteration 1 FF. These results indicate that including the orientation dependent term affects the configurations of the two adsorbates and must be considered during a binary simulation.

4.4. Force Field Development for Propane and Propylene

In the previous section, we have outlined our force field development algorithm for ethane and ethylene adsorption in CuBTC using periodic DFT calculations. We now turn to extending the same approach for higher hydrocarbons such as propane and propylene.

From the ethane and ethylene results in Section 4.3, we now have Morse FF parameters for CH2_sp2 UA (ethylene) and CH3_sp2 UA (ethane) interactions with the Cu OMS. To describe adsorption of propane and propylene, additional CH_sp2

(propylene) and CH2_sp2 (propane) interaction parameters are required. The steps involved in this calculation are similar to the previous Section and only a brief description of the method is provided here.

Using a similar strategy as in Section 4.3.2, we performed single point energy calculations for an initial set of favorable configurations of propane and propylene in CuBTC. The propylene molecule is appropriately oriented to maximize the interaction of the C=C double bond with the Cu OMS. The vdW-DF2 functional is used to obtain the interaction energies from periodic DFT calculations, giving the results shown in Figure 4.11. Of the initial configurations sampled in our work, the largest interaction energy (-38.0 kJ/mol) is seen for propylene at a distance of 2.8 Å from the Cu OMS. This is comparable to ethylene results (-29.8 kJ/mol at 2.8 Å), indicating that the pi-bond/Cu OMS interactions are similar in both the olefins. For propane, the strongest interaction (-22.3 kJ/mol) is seen at a larger distance of 3.4 Å as specific interactions with the Cu atoms are absent.

The contribution of the unknown CH_sp2 (for propylene) and CH2_sp3 (for propane) interactions with the Cu atom are obtained by subtracting the known components from the total vdW-DF2 interaction energy (dotted lines, Fig. 4.11). These known terms include the CH2_sp2/Cu (from ethylene), CH3_sp2/Cu (from ethane) and DREIDING FF for C, H and O interactions.

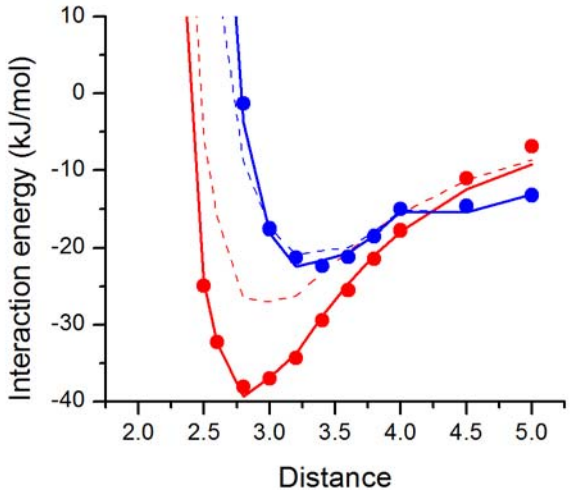

Figure 4.11. Interaction energies for initial configurations of propane (blue) and propyelne (red) in CuBTC calculated using vdW-DF2 DFT method (filled circles) and the fitted force field (solid lines). The dotted lines represent the contributions from the known CH2_sp2 and CH3_sp3 interactions with the framework.

Table 4.4. Fitted Morse parameters and orientation dependent terms for the interaction of the Cu OMS for propylene and propane in CuBTC.

Adsorbate united atom	D_0 (kJ/mol)	ρ (Å)	α	A (kJ/mol)	B ($Å^{-1}$)
CH2_sp3	1.38	19.14	3.34	-	-
CH_sp2	24.9	6.7	2.11	9.3957	0.5106

The difference between the vdW-DF2 and the known components was fitted using a classical Morse potential to give parameters for the CH_sp2/Cu (for propylene) and CH2_sp3/Cu (for propane) interactions. Figure 4.11 shows that the fitted Morse potential gives good agreement with the vdW-DF2 interaction energies, as expected, and this version of the FF is denoted as VDW-DF2 (Iteration 1).

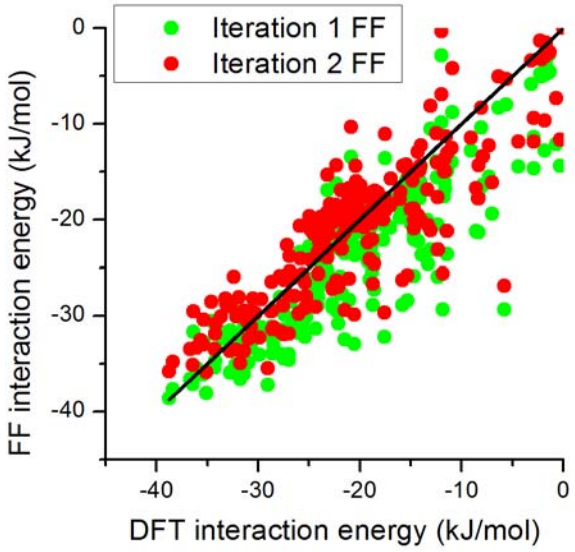

Figure 4.12 Comparison of the interaction energies calculated from vdW-DF2 DFT method with the VDW-DF2 (Iteration 1) FF (green) and VDW-DF2 (Iteration 2) FF (red) for 400 configuration of propylene in CuBTC.

Similar to the previous calculations for ethylene and ethane, another iteration was performed using 400 GCMC generated configurations of propane and propylene in CuBTC. The final FF parameters for the Iteration 2 FF include the orientation dependent term for propylene and are shown in Table 4.4. Figure 4.12 compares the vdW-DF2 predicted energies for 400 propylene configurations with the VDW-DF2 (Iteration 2) FF. The MAD (MD) is reduced from 4.0 kJ/mol (2.7 kJ/mol) for Iteration 1 to 3.5 kJ/mol (0.1 kJ/mol) for Iteration 2 when the orientation dependent term is included. Compared to the MAD for ethylene (~2 kJ/mol), the slightly higher MAD for propylene is due to the increasing complexity of the adsorbate and the addition degree of freedom from the CH3_sp3 united atom.

Using the FF parameters in Table 4.4, we performed GCMC simulations for propane and propylene in CuBTC. Figure 4.13 compares the predicted adsorption isotherms for propane and propylene with scaled experimental data from Fischer et al.[69]

The experimental data has been scaled based on the measured surface area to match the calculated value of 0.85 cc/g. The predicted isotherms show excellent agreement with the scaled experimental data for both propane and propylene adsorption at all conditions.

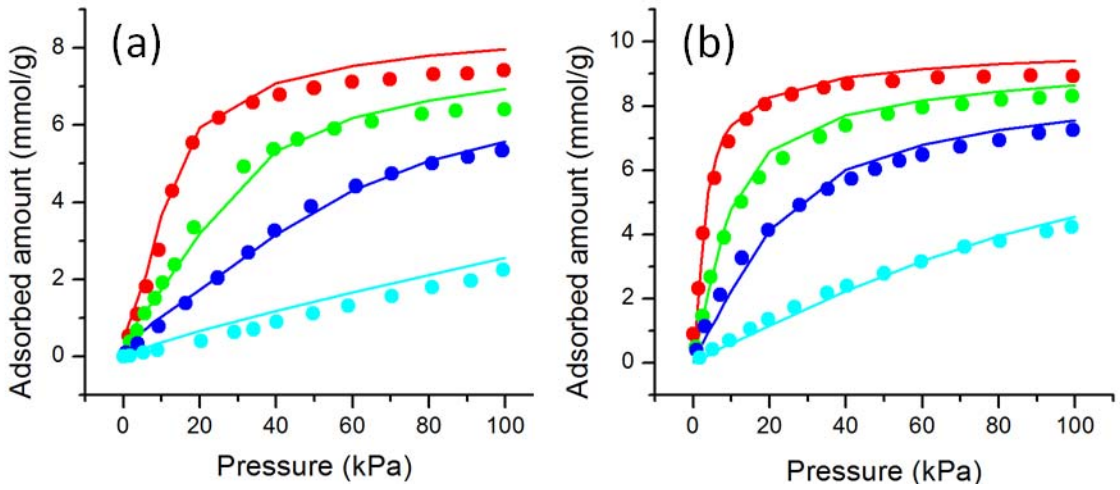

Figure 4.13 GCMC predicted adsorption isotherms for (a) propane and (b) propylene in CuBTC using the VDW-DF2 (Iteration 2) FF for the framework atoms and the TraPPE FF (solid lines) for the adsorbates at 323 K (red), 348 K (green), 373 K (blue) and 423 K (cyan). The scaled experimental adsorption isotherms from Fischer et al.[69] are shown by filled circles.

These results are encouraging and indicate the transferability and versatility of our FF development approach for modeling increasingly complex adsorbates. Since we now have interaction parameters for CH3_sp3, CH2_sp3, CH2_sp2 and CH_sp2 with the Cu OMS, the DFT-derived VDW-DF2 FF can be used for modeling adsorption of higher olefins and paraffins.

Note that the isotherms from GCMC shown in Figure 4.13 for both propane and propylene are obtained purely from computational methods and do not include any fitting or adjustments based on the experimental measurements.

4.5. Transferability to other Cu open metal site MOFs

To aid in selecting MOFs for for olefin/paraffin separations computationally, it is desirable for the FF derived above to be transferable to other Cu OMS MOFs. In this section, we evaluate the transferability of our ethane and ethylene FF based on DFT calculations and comparison to the available experimental data.

As discussed in the Introduction, experimental data for ethane/ ethylene adsorption in Cu OMS MOFs is limited, and reproducible isotherms from different groups are available to date only for CuBTC. However, a previous study by He et al.[75] has reported ethane and ethylene single component isotherms for a range of MOFs including MOF-505, PCN-16, UMCM-150, NOTT-101, NOTT-102 and USTA-20. Based on the size of the size of the unit cells of these materials, periodic DFT calculations are feasible only for MOF-505 and PCN-16. Similar to CuBTC, the metal center in these two MOFs consists of the di-copper cluster surrounded by 8 oxygen atoms in an octahedral geometry. The linkers for MOF-505 (3,3',5,5'-Biphenyltetracarboxyl) and PCN-16 (5,5'-Ethyne-1,2-diyldiisophthalato) differ from the CuBTC linker (1,3,5-benzenetricarboxylate).

It is important to note that the transferability of our FF to these two materials can be judged in two distinct ways. First, we can test whether our FF is consistent with DFT calculations for each material. Second, we can compare predictions using our FF to adsorption data from each material. Here, we focus on the evaluating the DFT transferability as the adsorption data reported by He et al.[75] have not been reproduced and verified by other experimental groups.

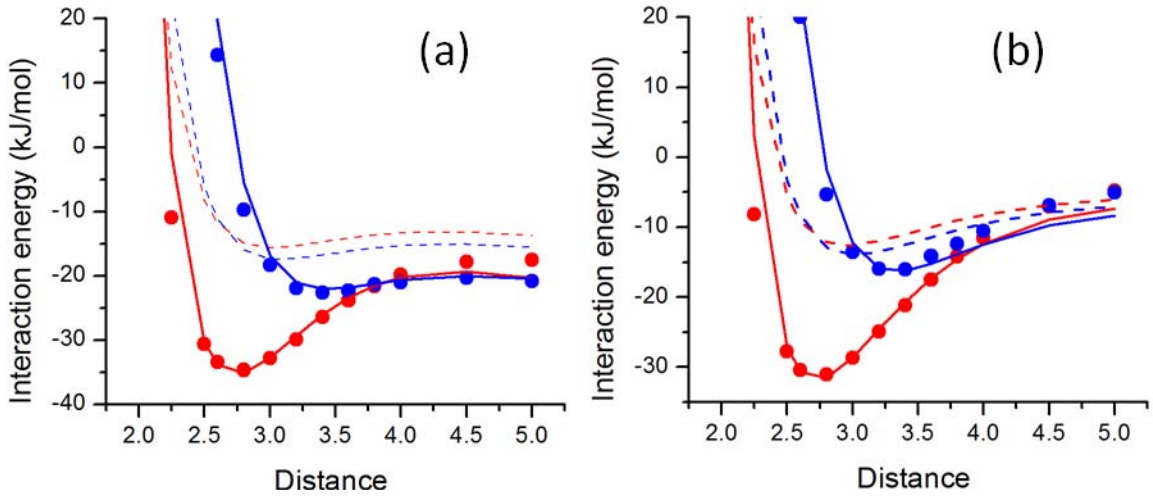

Figure 4.14 Interaction energies for initial configurations of ethane (blue) and ethylene (red) in (a) MOF-505 and (b) PCN-16 calculated using vdW-DF2 DFT method (filled circles) and the VDW-DF2 (Iteration 2) force field (solid lines). The dotted lines represent the contributions from the generic DREIDING FF for C, H and O interactions.

Similar to our calculations in Section 4.3.2, initial favorable configurations for ethane and ethylene were generated in MOF-505 and PCN-16. The DFT interaction energy is calculated using the vdW-DF2 functional and is compared to VDW-DF2 (Iteration 2) FF predictions in Figure 4.14 for MOF-505 and PCN-16. The results in Figure 4.14 indicate that the VDW-DF2 FF obtained from CuBTC, gives excellent prediction of the vdW-DF2 energies for MOF-505 and PCN-16 for both ethane and ethylene.

We now evaluate the transferability of the orientation dependent term fitted to CuBTC for the MOF-505 and PCN-16. A set of ethylene configurations were obtained from the GCMC snapshots and were used for periodic DFT calculations using vdW-DF2 functional. The DFT interaction energies for 400 GCMC generated configurations are compared with the DREIDING and VDW-DF2 FF predictions in Fig. 4.15 for MOF-505 and PCN-16.

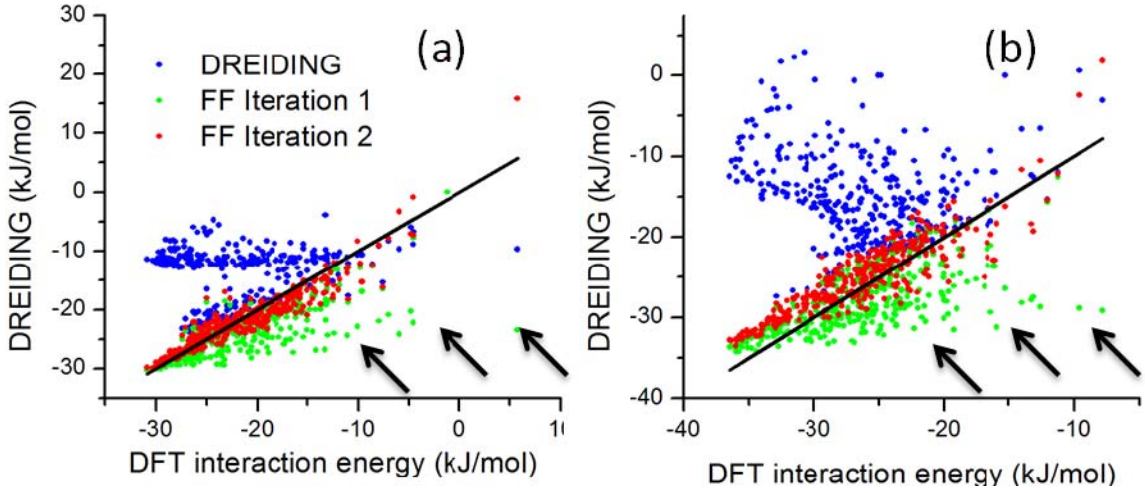

Figure 4.15 Interaction energies for 400 GCMC configurations of ethylene in (a) MOF-505 and (b) PCN-16 calculated using vdW-DF2 DFT method compared to the predictions form DREIDING FF (blue), VDW-DF2 (Iteration 1) FF (green) and the VDW-DF2 (Iteration 2) FF (red).

Not surprisingly, the DREIDING FF fails at predicting the vdW-DF2 interaction energies. The Iteration 1 FF gives good agreement with the DFT energies but overpredicts the interaction energies for some of the configurations (black arrows). This is due to the unfavorable orientations of ethylene close to the Cu OMS. The best performance is seen for the Iteration 2 FF, which includes the orientation correction. The MAD for the interaction energies obtained from Iteration 2 FF for MOF-505 (2.2 kJ/mol) and PCN-16 (1.7 kJ/mol) are actually lower than the CuBTC results (2.3 kJ/mol). The improved quality of predictions seen for MOF-505 and PCN-16 is because the confinement effect previously seen for octahedral side-pockets in CuBTC is absent in these MOFs. The parameters used for the VDW-DF2 FF in all of these calculations were obtained from CuBTC results in Section 4.3 and are not re-parameterized for the new systems.

The previous discussions suggest that the Morse FF parameters and the orientation dependent terms generated from periodic CuBTC calculations can be used for predicting interaction energies in other OMS MOFs. It should be highlighted that the VDW-DF2 (Iteration 2) FF reproduces the ethane and ethylene interaction energies in MOF-505 and PCN-16 even though the linkers are different than the simple 1,3,5-BTC linker in CuBTC. This is an important observation, as it implies that for MOFs containing Cu open metal sites, the interactions of the Cu atom with the adsorbate are not significantly affected by the nature connecting ligand. This further suggests that the FF developed and validated in the previous sections can be used for evaluating other MOFs that contain Cu open metal sites.

4.6. Identification of open metal site MOFs

We have shown in the previous section that a FF developed from DFT methods is transferable to MOFs containing Cu open metal sites. However, due to the large number and the huge diversity of MOFs that have been reported, systematic identification of open metal sites is not trivial. Although the CSD database contains extensive data on MOF crystal structures, many of these structures are not directly suitable for computational studies due the presence of solvent, structural disorder, and other issues.

Recently, we have developed efficient methods for obtaining computation-ready MOF structures from the CSD.[159] The structures reported in the so-called CoRE MOF database resulting from this analysis have no disordered atoms, and no bound or unbound solvent species. We used the CoRE MOF database (~5000 structures) to identify MOFs that contain Cu open metal sites using the following criteria: (1) Identifying MOF that contain only one metal cluster with Cu as the metal atom (2) only including MOFs that

have di-copper metal cluster (3) only including MOFs that have octahedral geometry for both the individual Cu atoms. Since the FF has been developed for metal centers that consist of Cu dimers octahedrally surrounded by 8 neighbors, we have restricted our search to finding MOFs with similar Cu connectivities. Using this approach, we identify a set of ~100 structures that are used for the screening study described below.

4.7. Screening of Cu OMS MOFs for Olefin/Paraffin Separation

The list of MOFs that contain the di-copper open metal sites are listed in Table 4.5. As an example of an industrially relevant separation, we chose to study the separation of an equimolar mixture of propylene and propane. For each of Cu open metal site MOFs we perform binary GCMC simulation using an equimolar mixture of propylene and propane at 303 K and a total pressure at 2.5 bar. Figure 4.16 show the propylene/propane molar selectivity observed in the adsorbed phase as a function of the gravimetric propylene capacity. Our calculations suggest that there is a clear trade-off between olefin uptake and selectivity. The materials that have high olefin uptakes (> 40% by weight) generally have selectivities close to 1. The calculated propylene/propane selectivity of CuBTC at these conditions is 2.8 and the propylene uptake is ~31%. The highest selectivity is obtained for MOFs BIMDIL (15.5) and BIMDEF (10.0) with capacities of ~19% by weight. Further analysis of these two MOF structures indicates that the high selectivities are due the presence of 1-dimensional narrow channels that allow for preferential interactions of the Cu open metal sites with propylene.

Table 4.5 Cambridge Structure Database (CSD)[5] refcodes of 96 MOFs containing the di-copper open metal sites identified using the algorithm in Section 5.6.

QOJVAM	BIMDEF	QOWRAV01	VUJBIM	RICBEM	YEKXOD
LAZXOB	BIMDIL	ZIKJIO	XAHPON	XAHQAA	LASYOU
SUJNUH	LUYHAP	ZIKJOU	FEBXIV	LURRIA	MOCKEV
KOJZIT	MOCKAR	ALAMUW	ADASIJ	SUKYON	NUTQAV
CECVAI	RUVKAV	ANUGOG	MEHMET	GAGZEV	NUTQEZ
MOYYEF	BEXVEH	ANUGIA	RAHNOF	HABQUY	YUGLES
MOYYIJ	LASDEQ	HEXVEM	XAHPED	LEHXUT	HOGLEV01
PARNIH	KOJYEO	XITYOP	HANWAW	SUNLET	HOGLEV
LEDLEN	PALTON	SUKYIH	KIJRUS	TOHSAL	NAYZOE
OGEBAF	ANUGEW	ANOMUM	PEWLUA	XAHPUT	MAFJIO
PARNON	TEMPEI	ONIXOZ	REWNEO01	EPISOM	DICKEH
XOPLOE	NIBJAK	CUYWUP	REWNEO	OWIZAW	NIBHOW
XAHPAZ	ACUFEK	NIGDIS	BAZFUF	XAFFOB	XAFFUH
BAZGAM	LELDUD	LEVDIB	MUDTEL	SEMNEF	CAJQIP
EPOTAF	XAHPIH	XALXUF01	XALXUF		
FECXES	GEGDED	DAWMUL	DOTSOV		

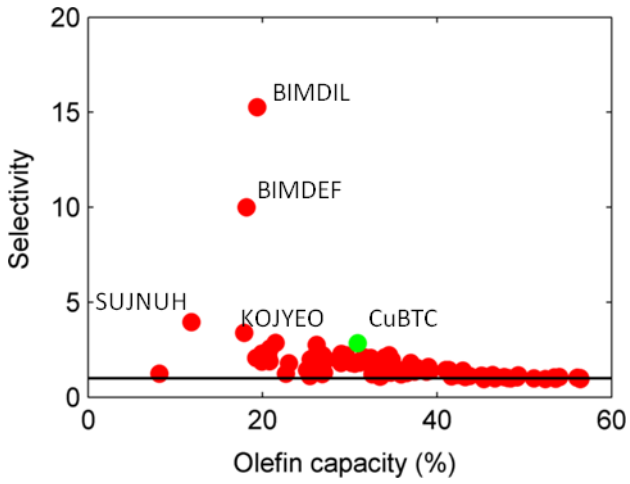

Figure 4.16 Propylene/propane selectivity for an equimolar olefin/paraffin mixture at 2.5 bar and 303 K as a function of propylene capacity for 96 MOFs that contain the di-copper open metal site. The green circle shows the performance of CuBTC.

4.8. Conclusions

In this Chapter, we have extended our previous force field development methodology to more complex MOFs that contain Cu open metal sites. Our results show

that the force fields derived from vdW-DF2 DFT method successfully predict the adsorption properties of ethane, ethylene, propane and propylene in CuBTC at different temperatures. The force fields are transferable to other similar materials and can be used for screening of MOFs for propylene/propane separations. In the future, we believe that similar analysis can be used to rapidly discover MOFs that show high performance for different industrially relevant separations.

CHAPTER 5

CONTROL OF METAL-ORGANIC FRAMEWORK CRYSTAL TOPOLOGY BY LIGAND FUNCTIONALIZATION: FUNCTIONALIZED HKUST-1 DERIVATIVES [b]

Metal-Organic Frameworks (MOFs) have received considerable attention over the last few years due to the possibility of tuning the macroscopic properties of the material by using appropriately functionalized ligands. The reticular synthesis approach is complicated in scenarios where ligand functionalization leads to new crystal structures. This phenomenon has been experimentally reported for CuBTC. In this chapter, we use a quantum chemistry approach to predict the crystal topology of CuBTC (HKUST-1) derivatives for different functionalized ligands. Our results show that the functionalized CuBTC structures can be rationalized computationally using Density Functional Theory (DFT) and electron localization function (ELF) calculations. This analysis leads to a simple "design principle" for predicting the structure by analyzing the bonding characteristics of the functional groups with the BTC linkers.

5.1. Introduction and Literature Review

Metal-organic framework (MOF) materials are nanoporous crystals that have attracted intense interest for fundamental and applied purposes.[160-163] MOFs are

---

[b] Portions of this chapter were adapted from DOI: http://dx.doi.org/10.1021/cg501285q (Just Accepted Manuscript, Co-first author)

interesting in part because of the concept of reticular synthesis, which allows families of isostructural crystals to be developed by varying ligand length and functionality.[164,165] Demonstrations of isostructural families are available for IRMOFs,[18] UIO-66,[166-168] and MIL-53,[169,170] among others. The predictability associated with MOF crystal structures is complicated in situations where ligand functionalization leads to new crystal structures.

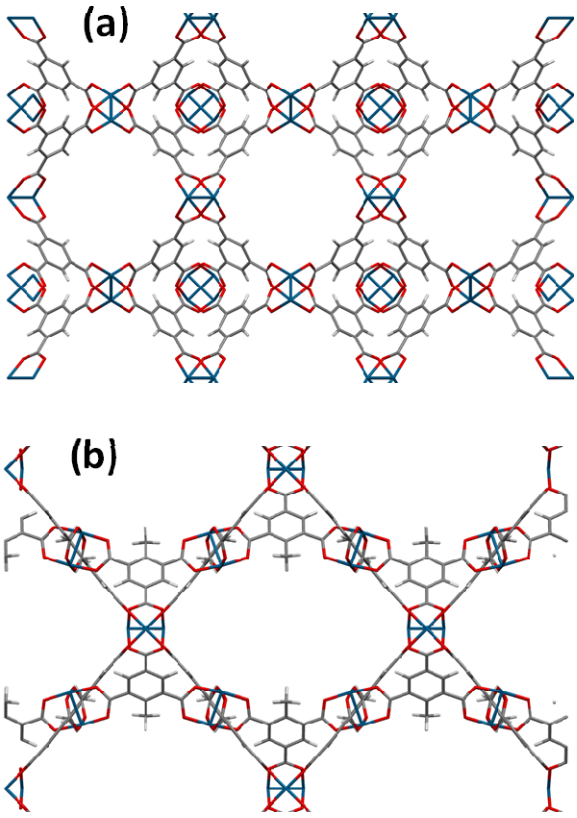

Figure 5.1. Comparison of the two experimentally observed topologies of CuBTC, viewed along the main pore direction: (a) tbo and (b) fmj-methyl [171] topology. The colors used are: oxygen (red), copper (blue), carbon (grey) and hydrogen (white).

HKUST-1 (also known as CuBTC), first reported by Chui et al.,[13] is one of these most widely studied MOFs. The structure is comprised of Cu^{2+} paddlewheel clusters coordinated to 1,3,5-benzenetricarboxylate (H_3BTC) organic linkers in a twisted boracite (tbo) topology (Fig. 5.1(a)). Although HKUST-1 has been well studied, limited work has

been done to modify the H_3BTC ligand or functionalize HKUST-1 to optimize its properties for specific applications. Recently, two Cu-based frameworks with methyl and ethyl functionalized H_3BTC ligands have been experimentally reported.[171] These two frameworks have a different crystal structures from HKUST-1. Topological analysis[172] shows these frameworks have a fmj net (Fig. 5.1 (b)). The fmj net has been constructed previously on purely topological grounds[173] but no material had previously been observed to form this structure. Recently, Peikert et al.[174] reported an amino-functionalized HKUST-1 MOF that is isostructural to the parent material. A large recent *in silico* library of possible MOF structures included HKUST-1 in the tbo structure but no other polymorphs with the same stoichiometry.[175]

More recently, we have shown[176] experimentally how the crystal structures of derivatives of HKUST-1 varies for a set of six functionalized ligands shown in Figure 5.2. Our experiments show that use of functionalized ligands within this family leads to multiple distinct crystal structures. In this chapter, we use periodic and cluster Density Functional Theory (DFT) calculations to show that these structures can be rationalized computationally. Our results open the possibility of predictively controlling crystal structure in similar situations for different MOFs.

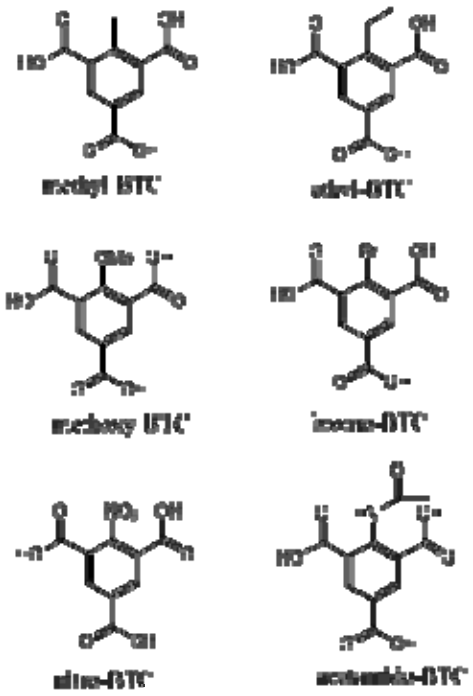

Figure 5.2. Functionalized ligands used for synthesizing derivatives of HKUST-1.

5.2. Computational Methods

We performed periodic Density Functional Theory (DFT) calculations as implemented in Vienna *ab-initio* Package (VASP)[177] using the PBE exchange-correlation functional[102] with Grimme's D2 correction[103] for dispersion interactions. The dicopper metal cluster is known to be anti-ferromagnetic,[14] so the periodic calculations were initialized with an anti-ferromagnetic spin ordering and spin polarization was used. The DFT energies were computed using a plane wave cutoff of 400 eV and a force tolerance of 0.03 eV/atom. Due to the large size of the unit cells, only the gamma point was used. To reduce computational cost, spin polarization was not used for the cluster calculations that are described in the next section. For geometry relaxations that involved a volume change, an energy cutoff of 700 eV was used for optimization of the lattice prior to the fixed volume calculation at 400 eV. For the tbo topology, the 156 atom, rhombohedral,

primitive cell of HKUST-1 was used.[14] The electron localization function (ELF) calculations were performed using VASP and the surfaces at an iso-value of 0.87 were used to generate the images. Our DFT calculations do not include solvent effects.

Table 5.1. Observed Crystal Structure and N_2 BET Surface Areas of HKUST-1 and 7 Analogous MOFs made with Functionalized Ligands.

Linker	Solvent	Topology	Surface Area (m^2/g)	
			Accessible[a]	BET
H-BTC[13]	DMSO	tbo	2224	1800[178]
methyl *	DMF	fmj	1921	1471
ethyl *	Water/ EtOH	fmj	1563	1434
methoxy *	DMF/ HCl sol.	fmj	1824	1259
bromo	DMF/ Formic acid	tbo	1929	1458
nitro	DMF/HCl sol.	tbo	1998	921
acetamide	DMF/HCl sol.	tbo	1680	1415
amino[174] *	DMA	tbo	2015	1834[174]

*Single crystal XRD structure has been solved [a] The theoretically accessible surface area was calculated using the methods of Düren et al.[179] using DFT-optimized structures.

5.3. Summary of Experimental Results

The key observations from the MOF synthesis and characterization are summarized in Table 5.1, which also lists the experimental crystal structure of each material. Four of the functionalized materials (bromo, nitro, acetamide, and amino) retain the same tbo topology as the parent HKUST-1 structure. The methyl, ethyl, and methoxy-functionalized ligands, however, lead to the formation of the fmj topology. In addition to

the ligands presented in Fig. 5.2, Table 5.1 also includes the amino functionalized material reported by Peikert et al.[174]

We used quantitative computational methods to rationalize the variation in crystal structures seen for the materials described above. To introduce these results, it is useful to consider how individual ligands differ in the tbo and fmj topologies. The configuration of the BTC linker can be described by carboxylate torsion angles, ϕ and C_1-C_2-C_3 angles, θ as shown in Fig. 5.3(a). First, we consider the tbo topology of HKUST-1. For the ideal tbo topology (Fig. 5.3(b)), all three carboxylate groups lie in plane with the benzene ring, making $\phi = 0°$. Additionally, the linker's three-fold symmetry and sp^2 hybridization of C_2 ensures that each $\theta = 120°$. Unlike the tbo topology, the presence of functional groups in the fmj topology pushes away two ortho-carboxylate groups and causes them to be twisted out of the plane ($\theta > 120°$ and $\phi > 0$). The third carboxylate group at the para position with respect to the functional group is essentially unaffected. The SBU of the fmj topology consists of two types of linkers with different values of ϕ and θ. For example, the SBU of fmj-ethyl (Fig. 5.3 (c)) has linkers with $\theta = 130.7°$, $\phi = 34.5°$ and $\theta = 121.1°$, $\phi = 55.0°$.

Besides the tbo and fmj topologies that have been observed with BTC linkers, another topology, pto, is known for Cu-paddle wheel MOFs using BTB [benzene-1,3,5-tribenzoate] as a linker.[180] Amirjalayer et al have compared the pto and tbo topologies for the BTC and BTB linkers using a DFT-derived molecular mechanics force field.[181,182] In this work, the tridentate BTB linker was replaced with the BTC linker to give a third polymorph for dicopper-BTC polymorphs. For the ideal dicopper-BTC pto topology, all three carboxylate groups are twisted by the same amount, $\phi = 34.1°$ (Fig. 5.3(d)).

In addition to the three nets that have been discussed earlier, various non-edge transitive nets have been studied for other 3,4-connected networks using force field methods.[183] Similar DFT calculations for our dicopper-BTC system are computationally infeasible and beyond the scope of this work. Details of the tbo, pto and fmj nets used in this work can be found online. [142]

Table 5.2. Comparison of DFT-D2 Predicted and Experimental Lattice Constants (*italics*) for HKUST-1 in the tbo Topology and Methyl-, Ethyl-, and Methoxy-Functionalized Materials in the fmj Topology. All values are reported in Å.

	a	***b***	***c***
HKUST-1	18.71 *(18.63)*	18.71 *(18.63)*	18.71 *(18.63)*
fmj-methyl	19.78 *(19.82)*	19.80 *(19.82)*	22.50 *(22.60)*
fmj-ethyl	20.25 *(20.13)*	20.22 *(20.13)*	20.57 *(20.55)*
fmj-methoxy	19.60 *(19.45)*	19.68 *(19.45)*	23.82 *(24.13)*

5.4. Periodic DFT Calculations

We performed Density Functional Theory (DFT) calculations to gauge the relative stability of various polymorphs. The DFT calculations were validated by comparing experimentally reported and DFT optimized structural parameters. Table 5.2 compares the experimental and DFT-predicted lattice constants of each material for which single crystal XRD data were available. Experimentally, the three ligands that give the fmj structure give quite different lattice parameters along *c* direction. The DFT results are in good agreement with the experimental data for all four materials.

5.4.1. Unfunctionalized BTC

We first discuss the polymorphs using the unfunctionalized BTC linker (denoted below as H-BTC). The initial structure for this linker in the fmj topology was obtained from the methyl- and ethyl-functionalized fmj crystal structures observed experimentally.[171] After replacement of the bulky alkyl groups by -H, a large volume change is observed during the DFT relaxation of the two fmj-H polymorphs; the *c* lattice constant changes from 22.60 (20.55) to 25.03 (25.09) during energy minimization. The final structures and energies for the two cases are very similar, however. Because the number of BTC linkers/unit cell is different for different topologies, polymorphs are compared based on the basis of energy/BTC linker. Table 5.3 compares the total energy/BTC linker for the three polymorphs relative to HKUST-1 (tbo). Of the three polymorphs, the experimentally observed tbo topology has the lowest total energy; the fmj (pto) polymorph is 3.3 (2.8) kcal/mol per BTC linker more unfavorable than the tbo structure. Our results are comparable to the force field approach of Amirjalayer et al, which predicts the pto topology to be 2.98 kcal/mol BTC linker higher in energy than tbo.[181,182]

It is also useful to compare these energy differences with experimentally observed polymorphs of zeolitic imidazolate frameworks (ZIFs). For ZIFs, energy differences of ~ 6.6 kcal/mol per imidazolate (~0.57 eV/ $Zn(Im)_2$)[184,185] have been shown to result in strong preferences for one polymorph over another. It is therefore not surprising that the energy differences listed in Table 5.3 lead to the tbo topology being observed experimentally. Table 5.3 also lists the energy differences associated with the DFT and dispersion correction energies for each structure. This decomposition shows that the

energy change associated with the metastable polymorphs is dominated by non-dispersion contributions.

Table 5.3. DFT-D2 energies (in kcal/mol BTC-linker) of fmj and pto polymorphs relative to the tbo topology for the H-BTC linker. The contribution of the electronic part (DFT) is larger than the dispersion interactions (vdW), and is compared to the relative energies obtained from cluster calculations using ϕ.

Topology	DFT-D2	DFT	vdW	Calculated based on ϕ
tbo	0.0	0.0	0.0	0.0
fmj	3.3	3.4	-0.1	3.2
pto	2.8	3.6	-0.8	3.6

The relative energies in Table 5.3 can be explained by the structural differences of the BTC linkers in the tbo, fmj and pto topologies (see Fig. 5.3). The DFT optimized fmj topology consist of two types of BTC linkers with ϕ = 51.7° and ϕ = 11.1°. For the pto polymorph, all three carboxylate groups have a torsion angle ϕ = 34.1°.

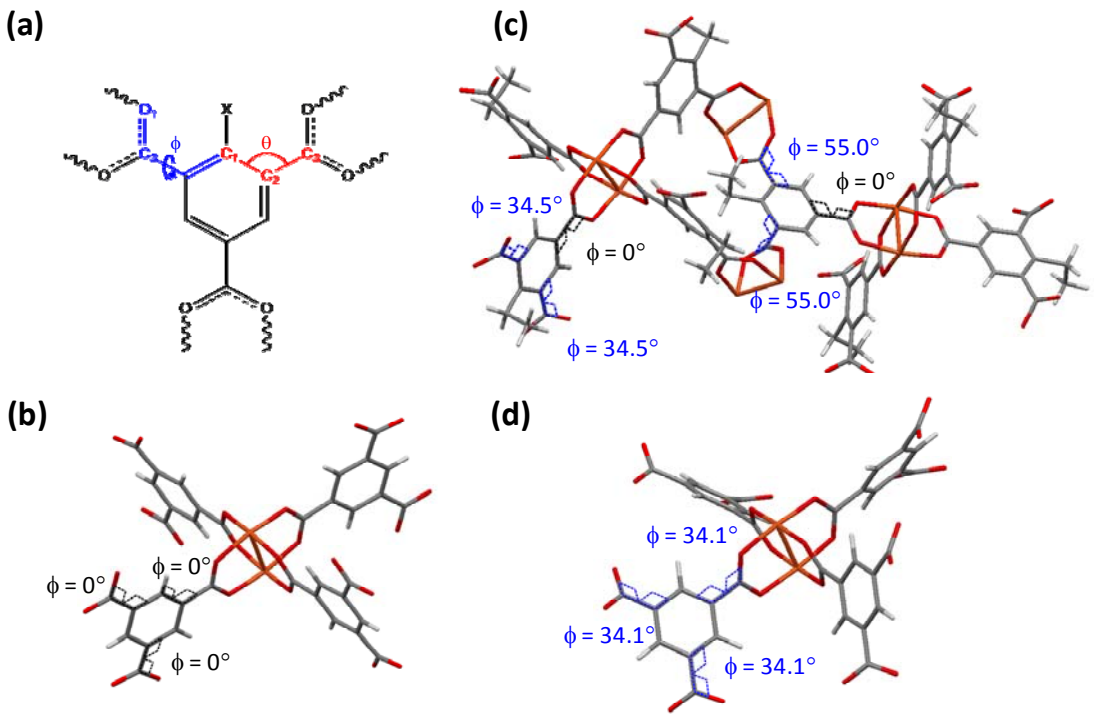

Figure 5.3. (a) Schematic of the BTC linker showing the sp^2 C_1-C_2-C_3 angle, θ (red) and carboxylate torsion angle, ϕ (blue). For unfunctionalized BTC linkers, X = H while for functionalized BTC linkers, X is replaced by the corresponding functional group. Representative images for secondary building units (SBU) are shown for the (b) tbo, (c) fmj and (d) pto topologies. The colors used are: oxygen (red), copper (orange), carbon (grey) and hydrogen (white).

We performed additional DFT calculations without dispersion corrections using a cluster with a single BTC linker coordinated to three formate-terminated dicopper dimers (Fig. 5.4(a)). After energy minimizing the cluster, the cluster energy was calculated as one carboxylate group was rotated (Fig. 5.4(b)). The energies for the periodic structure were then estimated using only the torsion angles, ϕ of the carboxylate groups of the crystal structure and the data in Fig. 5.4(b). The calculated relative energies (Table 5.3) show good agreement with the DFT energies for the fully periodic structures, showing the relative energies of the H-BTC polymorphs can be explained by the configuration of the BTC linkers.

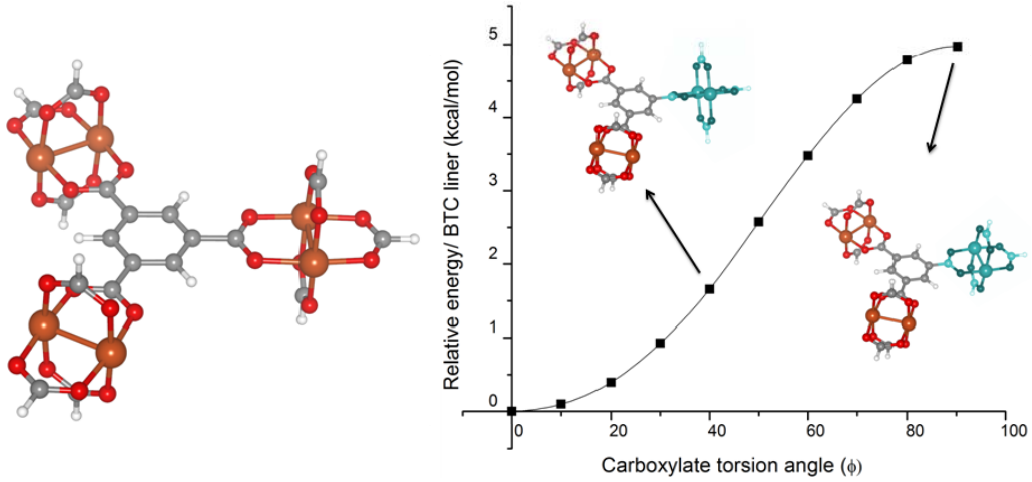

Figure 5.4. (a) Cluster used for single point energy calculations (b) Relative energies as a function of the rotation of one carboxylate group (black squares). The solid line represents the fitted spline curve used to obtain the relative energies shown in Table 5.3.

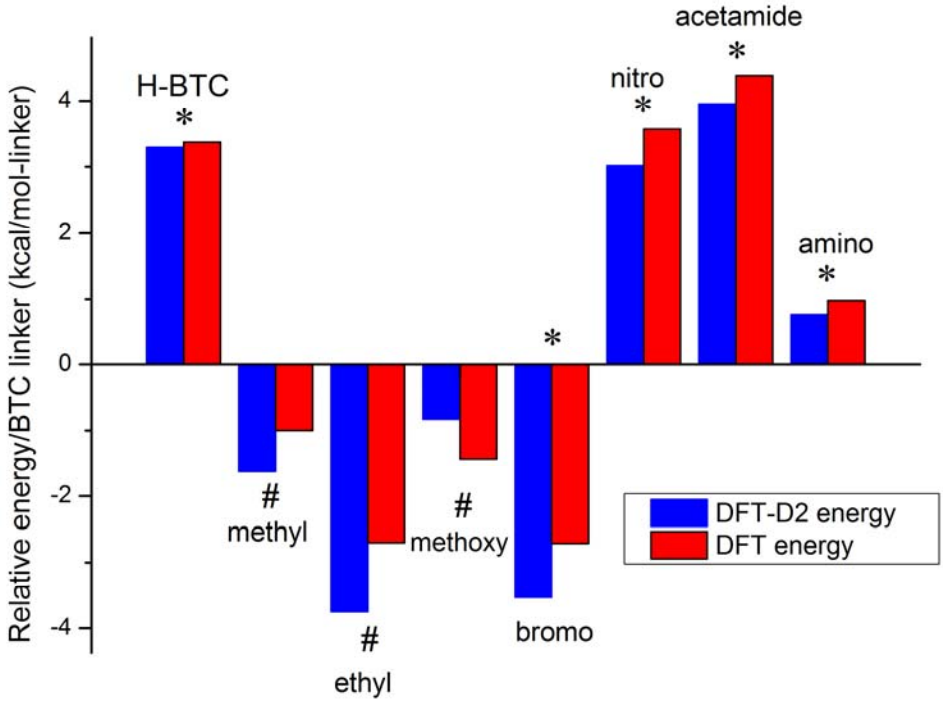

Figure 5.5. Comparison of the total DFT-D2 energy and the DFT energy without dispersion corrections for different functional groups for the fmj and tbo topologies. A positive value for relative energy indicates that the tbo topology is preferred. Experimentally, functional groups that are denoted by * prefer the tbo topology and the functional groups denoted by # prefer the fmj topology.

5.4.2. Functionalized BTC

We now turn to the functionalized BTC polymorphs. Functionalization makes the BTC linker locally anisotropic, and a preferred position of the functional group can no longer be determined by symmetry. Recent results have shown that the amino group is equally distributed at all possible positions of the BTC linker.[186] To account for the possible orderings of the functional groups, one hydrogen atom of each BTC linker in our primitive unitcell was randomly chosen and replaced. This makes the unit cell anisotropic and volume relaxations resulted in physically unrealistic distortions of the structure. To better account for possible changes in lattice constants due to functionalization, optimization of the internal coordinates was performed at different fixed values of the lattice constants. The minimum energy corresponding to each ordering of functional groups was then obtained by a parabolic fit to the data. The lowest energy from applying this fitting to three possible orderings was then taken to be the material's energy. We confirmed that considering more than three orderings for the functional group did not change the qualitative prediction. For the functionalized tbo topology, the lattice constant corresponding to the minimum energy is close to the optimized HKUST-1 lattice constant. For the pto topology, the effect of lattice constant is found to be even less significant, and only fixed volume relaxations at the optimized H-BTC pto lattice constant were used. For the cases where the fmj topology was not observed experimentally (bromo, nitro, acetamide and amino), the methyl/ethyl group in the known fmj topology was replaced by the corresponding functional group to obtain initial structures for energy minimization.

Table 5.4. Summary of the DFT-D2 calculations for functionalized materials in the tbo and fmj topologies. Positive (negative) energy differences correspond to the tbo (fmj) structure being predicted to be stable. The structures of the tbo and fmj topologies are described in terms of the –COO torsion angle, ϕ and C_2-sp^2 angle, θ.

Linker	Energy difference[a]	Predicted Topology	tbo topology (ϕ,θ) (deg)		fmj topology (ϕ_1,θ_1) (ϕ_2,θ_2) (deg)			
H-BTC	3.3	tbo	1.9	119.9	11.7	118.9	51.7	120.8
methyl	-1.6	fmj	15.0	122.0	29.5	123.8	55.9	122.5
ethyl	-3.8	fmj	18.5	122.5	38.9	124.5	58.1	125.2
methoxy	-0.8	fmj	14.8	122.0	18.8	122.2	57.5	123.7
bromo	-4.0	fmj	21.7	123.4	37.4	125.7	59.5	126.5
					32.6	125.8	58.1	124.8
nitro	3.0	tbo	6.0	122.9	18.7	124.3	66.5	124.9
amino	0.5	tbo	7.5	121.9	123.4	121.5	14.7	47.5

[a]Energies are reported in kcal/mol-linker.

The total DFT-D2 energies for each functionalized polymorph are presented in Table F1. In every case, the pto topology is energetically unfavorable relative to at least one of the tbo and fmj polymorphs. For this reason, we restrict our attention to the differences between tbo and fmj topologies below (Table 5.4 and Fig. 5.5). As with the unfunctionalized material, dispersion contributions are only a small part of the energy difference between functionalized polymorphs (Fig. 5.5). Based on the total DFT-D2 energy the fmj topology is predicted for methyl-, ethyl-, methoxy- and bromo- BTC while the tbo topology is predicted for nitro-, amino- and acetamide-functionalized linkers. Of the 7 functional groups, our calculations correctly predict the experimental topology for all the functional groups except bromo-BTC. One possible explanation for the one inconsistency is that the more polarizable bromo group may have stronger solvent effects than the other functional groups. When DFT calculations were initiated from different initial lattice constants (c = 20.9 Å, 22.4Å) for bromo-BTC, different final

optimized structure were obtained that differed in the final energy by < 0.5 kcal/mol-linker. This indicates that the fmj topology may have some degree of flexibility of the linker for this specific material, leading to multiple local minima with similar energies.

5.5. Cluster DFT Calculations and ELF Analysis

To better understand the effect of θ and ϕ on the relative energies of the BTC linkers, we performed cluster DFT calculations using a functionalized version of the optimized cluster shown in Fig. 5.4. The energy-minimized clusters gave local geometries very similar to the 3D periodic structures, confirming that these clusters can reliably be used as models for the full crystal structures (data not shown). Calculations were performed where θ was varied from 119°-126° and ϕ was varied from 0° to ±90° to generate 160 distinct cluster configurations for each functional group. In these calculations, only the functional group was allowed to move while the remaining atoms were held rigid. The data were then fit to a 3-d surface spline to obtain the contour plots of the DFT energy as a function of ϕ and θ. The values of ϕ and θ corresponding to the minimum energy configuration of the cluster are reported in Table F2 for all the functional groups.

We will first discuss the contour plot for the H-BTC linker (Fig. 5.6 (a)), for which the relative energy is almost a parabolic function of ϕ and θ. The minimum energy from the contour plot (ϕ = 0° and θ = 120°) is very close to the ideal 3D H-BTC structure (ϕ = 1.9° and θ = 120°, Table 5.4). The linker configuration in the DFT optimized tbo

topology (yellow squares) is much closer to the optimum than for the fmj topology (green circles), in agreement with the energetic preference for the tbo topology.

Contour plots for ethyl-BTC and nitro-BTC linkers are shown in Fig. 5.6(b) and (c), respectively, and are representative of the other functional groups. The contours for ethyl-BTC are not symmetric about $\phi = 0$ due to the lack of symmetry of the functional group with respect to the benzene ring. The potential energy surface has two distorted parabolas and the region corresponding to ideal tbo topology ($\phi = 0°$, $\theta = 120°$) is unfavorable (>10 kcal/mol-linker higher in energy than the minimum energy). Comparing ϕ and θ from the periodic calculations (Table 5.4) with the minima from cluster calculations indicates that the structural constraints imposed by the tbo topology (yellow squares), force ϕ and θ to be closer to the unfavorable regions ($\phi = 0°$ and $\theta = 120°$). This explains the significant distortion observed in the optimized tbo structure with the ethyl-BTC linker. The fmj topology does not impose strong structural constraints, and ϕ and θ for the periodic fmj structures (green circles) are close to the minima on the contour plot. The contour plots for methyl and methoxy-BTC (Figure E1), are similar to ethyl-BTC, and the energetic preference of the fmj net can be explained by similar arguments. The nitro functional group (Fig. 5.6(c)) is an example of a material that prefers the tbo net. The minimum energy configuration in Fig. 6(c) is $\phi = 0º$ and $\theta = 123º$. The optimized 3D structure of the nitro-BTC linker in the tbo topology ($\phi = 6°$ and $\theta = 122.9°$) is very close to this minimum. Similar to H-BTC, the linker configuration for the fmj topology (green circles) is relatively unfavorable and the tbo topology is preferred. Similar observations were also made for the amino-BTC material (Fig. E1).

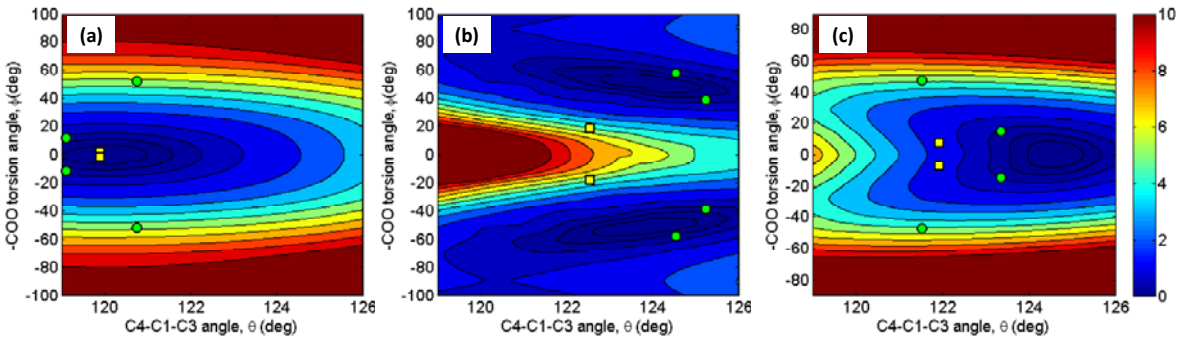

Figure 5.6. Contour plots of energy as a function of ϕ and θ for (a) H-BTC, (b) ethyl-BTC and (c) nitro-BTC linkers. The color scale ranges from 0 kcal/mol-linker (blue) to 10 kcal/mol-linker (red). The yellow squares and green circles represent the structural parameters from the DFT-D2 optimized tbo and fmj topology respectively.

Further insight into the topologies favored by different functional groups is provided by electron localization function (ELF) analysis[187] of relevant cluster geometries. Fig. 5.7 shows the ELF for a methyl-functionalized cluster in the tbo configuration and the energy minimum ($\phi = 40^o$, $\theta = 124^o$). The close proximity of the ortho carboxylate groups with H atoms of the functional group makes the tbo configuration unfavorable. Similar observations apply to the ethyl- and methoxy-functionalized materials, but not materials where the tbo configuration is favored (nitro, acetamide and amino). Analysis of the ELF plots for methyl, nitro and methoxy-BTC indicates that connecting groups that are sp^2 (sp^3) hybridized lead to minimal (significant) torsion of the carboxylate groups. That is, bulky sp^3-coordinated groups (e.g. methyl) prefer the fmj topology while sp^2-coordinated groups (e.g. nitro) prefer the tbo net.

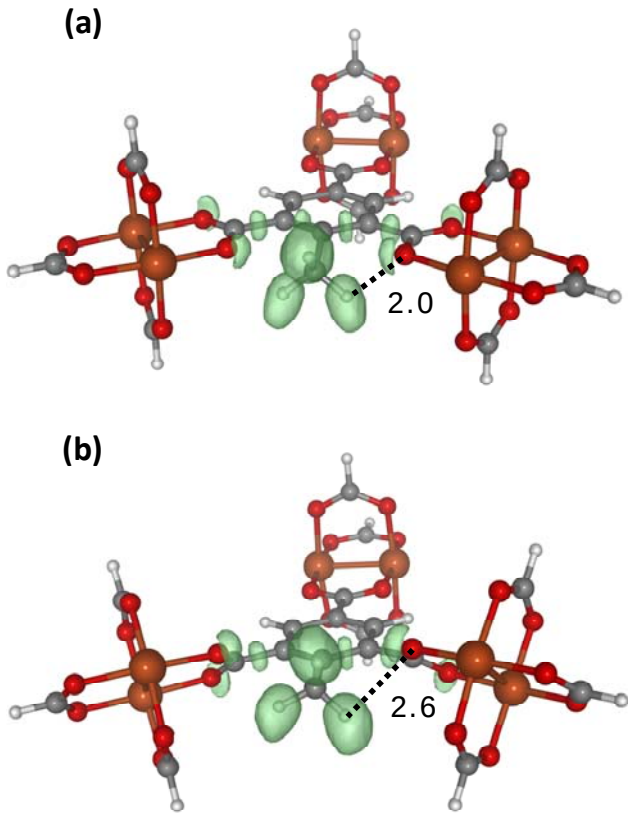

Figure 5.7. ELF for methyl-BTC for (a) the ideal tbo configuration and (b) the minimum energy configuration. The ELF is only shown in the vicinity of the functional group.

5.6. Conclusions

In this Chapter, we have described a DFT based approach for predicting the crystal topology of a number of functionalized HKUST-1 derivatives. Our results show that the existence of polymorphs of functionalized HKUST-1 materials can readily be understood by examining the potential energy surface associated with key degrees of freedom of the linkers in these materials. This analysis leads to a simple "design principle" for predicting the structure using the bonding characteristics of the functional groups to BTC linkers.

CHAPTER 6

CONCLUSIONS

6.1. Outlook

Metal-Organic Frameworks (MOFs) remain a very exciting area of research because of the potential applications in the chemical and related industries.[8] The reason for the continuously rising popularity of these materials is the relative ease with which novel MOFs can be synthesized. With the advent of efficient synthesis methods, highly functional ligands and better analysis techniques, it is likely to expect that MOFs and related materials will remain at the forefront of materials discovery and development.[188]

Given the huge diversity of the existing MOFs and the ever-increasing library of newly synthesized materials, it is a daunting challenge to study these materials for a given application. As newer and more complex materials are reported, it becomes impractical to thoroughly evaluate these materials experimentally. For instance, if a new MOF is initially reported to give reasonable performance for a certain application, it is quite possible that it may outperform the other known materials for a different application. This example highlights one of the weaknesses of using an isolated experiments based approach to identify top performing materials that target a specific application. Moreover, as the large scale synthesis and characterization of MOFs is time consuming and tedious, experimental screening of MOFs will be limited to only a handful of materials.

On the other hand, the large dataset of reported MOF structures provides an excellent opportunity to use molecular modeling techniques for rapidly screening

materials for a variety of applications.[136] Based on the published literature, most of these screening studies use generic force fields and have been focused on storage and separations of energy relevant molecules such as CO_2, CH_4 and H_2. [82,134,140,175] As more and more highly functional MOFs are synthesized, there is a clear need to develop better computational representation of the complex intermolecular interactions. In particular, the performance of generic force fields is unsatisfactory in scenarios where chemical interactions of the adsorbate and the framework dominate. One example is the interaction of the coordinatively unsaturated metal centers of the MOFs with molecules such as H_2O, olefins, CO_2 and NH_3.[14,21,87]

In such situations, it is necessary to generate force fields that can accurately model the energetics of the relevant adsorption system. One approach that has attracted significant attention is the use of quantum chemistry calculations to derive *ab-inito* force fields.[89] As these force fields are developed to model a certain complex adsorbate-framework interaction, it is reasonable to expect the force fields to be transferable to other materials where similar interactions dominate. This further implies that screening studies that are based on the *ab-inito* force field will result in more reliable predictions than the traditional generic force field approaches.[135] Assuming that reliable force field can be developed for modeling a certain subset of adsorption systems, the screening calculations can be easily extended to include the details of the actual separation process.

We believe that combining the high quality predictions obtained from *ab-inito* derived force fields with process modeling and optimization techniques will pave the way towards efficient material discovery and process development.

6.2. Summary

The overall objective of this thesis has been to study the various aspects of adsorption processes and nanoporous materials using different computational methods. In Chapter 2, we presented a process simulations study of a novel process for capturing CO_2 directly for the air. Our techno-economic analysis concludes that further detailed analysis of this process is justified.[42,189]

In Chapter 3, we evaluated the alkane/MIL-47(V) adsorption system using classical simulations approach and concluded that performance of the generic force fields was unsatisfactory. This issue was resolved by performing quantum chemistry calculations at the Density Functional Theory (DFT) level to develop force fields that give better agreement with experimental data.

In Chapter 4, this approach was further extended to studying more complex MOFs that contain coordinatively unsaturated metal centers. Our DFT based force fields show excellent predictions of experimental adsorption isotherms for HKUST-1 and are transferable to other MOFs that contain similar Cu open metal sites. The DFT-derived transferable force field was then used to screen ~100 MOFs of the industrially relevant propylene/propane separation.

Finally, in Chapter 5, we presented an application of DFT to predict the crystal topology of HKUST-1 derivatives for different functionalized ligands. Our calculations provided a framework for understanding the effects of linker functional groups on the overall topology of the MOF structure.[176]

6.3. Future Challenges and Opportunities

6.3.1. Force fields for open metal site MOFs and other adsorbates

As discussed previously, coordinatively unsaturated metal centers provide binding sites that allow chemical interactions of small molecules with the framework. In Chapter 4 of this work, we discussed a systematic approach for developing *ab-inito* force fields for Cu open metal sites with olefins, which were then used for a screening study. There a number of avenues, where similar force fields methods can be used for other open metal sites MOFs such as the MOF-74 series for Mg, Fe, Cu, Zn etc metal centers.[190] Moreover, this approach is not restricted to olefins and similar techniques can be applied for modeling interactions of ammonia, water, CO_2, H_2S and other polar molecules with open metal site MOFs.[89]

6.3.2. Material screening using detailed process models

To improve the performance of a given separation, it is not sufficient to just identify better performing materials. The optimum process conditions are strongly dependent on the macroscopic properties of the adsorbent, and a combined molecular modeling and process optimization approach is required.[50] For adsorption-based processes, this will involve additional breakthrough simulations to optimize the properties of each MOF during the screening procedure.[30]

6.3.3. Modeling flexibility of MOFs

Most of the adsorption results presented in this work have assumed that MOF structure remains rigid during the simulation. In reality, the MOF framework is not fixed

and may undergo changes upon adsorption of guest molecules.[17] The flexibility of the framework is even more important while calculating diffusion properties of larger molecules using MD simulations.[191] In such situations, it is necessary to develop force fields that model the intramolecular degrees of freedoms using first principles calculations. One approach towards systematically deriving and validating flexible force fields is to use a combined cluster and periodic DFT approach for studying Zeolitic Imidazolate Frameworks (ZIFs).[141]

6.3.4. Beyond DFT calculations

The force field development approach presented in this thesis assumes that Density Functional Theory is sufficiently accurate to model the interactions of adsorbates with the framework. In certain situations that involve charge transfer and polarization, the energies obtained from DFT are not suitable for force field development. In such scenarios, there is a need to develop methods that systematically correct DFT using computationally more expensive quantum chemistry methods.[192,193]

6.3.5. Force field development in zeolites

Similar to the approaches presented in this work, *ab-initio* force field development in siliceous and cationic zeolites has received considerable attention. Such studies have currently been limited to studying the adsorption of H_2O and CO_2 in Na^+, K^+ and Li^+ exchanged zeolites.[24,89,94] In additional to these cationic zeolites, there is a need to develop force fields that model the interactions of other polar adsorbates (H_2S, SO_x) with other cations such as Cu^{2+} and Cs^+. In many situations, the flexibility of the zeolite

framework in important and combined intramolecular and intermolecular force fields will be necessary for correctly modeling these systems.[191]

APPENDIX A

Table A1 Summary of annual climate data [50] for the six chosen US locations [a]

Location	Data Range	T_{max} (°C)	T_{min} (°C)	Mean T_{diff} (°C)	T_{mean} (°C)
Polk county, FL	2008-09	27.4	16.3	11.1	21.8
Black warrior river basin, AL	2008-09	24.4	11.5	13.0	18.0
Aneth fields, UT	2007-08	19.2	5.5	13.8	12.4
Atlanta, GA	2008-09	23.0	10.6	12.4	16.8
CRBG fields, WA	2008-09	18.0	6.4	11.6	12.2
Permian basin, TX	2009-10	25.0	10.0	15.1	17.5

[a] T_{max} and T_{min} are the average maximum and minimum temperatures observed in a year, respectively, T_{mean} is the mean temperature for a year and Mean T_{diff} is the average difference between the daily high and low temperature.

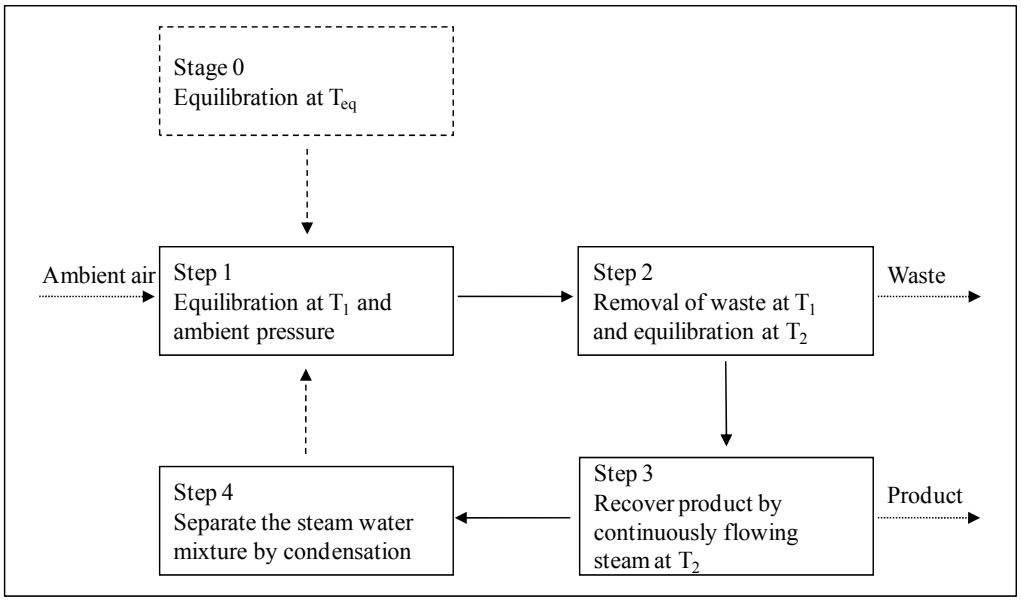

Figure A1 Schematic of TSA process used for the Air Capture process

Table A2 Cost and CO_2 emission factors for various sources of energy used in Chapter 2

Source [a]	Cost of energy [b]	CO_2 emissions [a]	
	\$/MWh	tCO_2e/MWh	MJ/tCO_2e
Coal			
Conventional coal	94.8	1.00	3591
IGCC	109.4	0.90	4000
IGCC with CCS	136.2	0.20	18000
Natural Gas			
Conventional combined cycle	66.1	0.40	9000
Advanced combined cycle	63.1	0.40	9000
Advanced CC with CCS	89.3	0.08	45000
Other			
Advanced nuclear	113.9	CO_2-free	NA
Wind	97.0	CO_2-free	NA
Wind—offshore	243.2	CO_2-free	NA
Solar PV	210.7	CO_2-free	NA
Solar thermal	311.8	CO_2-free	NA
Biomass	112.5	0.20	18000
Hydro	86.4	CO_2-free	NA
Steam [c]			
Steam generation (Scenario II)	15.2	0.30	11965
Purchased steam (Scenario III)	15.2	0.27	13236

[a] same as ref [28], [b] cost of electricity was updated based on a recent report [66], [c] from Table 2.4

APPENDIX B

Table B1. Parameters for the generic DREIDING[83] force field for framework atoms and TraPPE[106] force field for fluid-fluid interactions.

Atom Type	ε (K)	σ (Å)
C1	47.86	3.47
C2	47.86	3.47
C3	47.86	3.47
O1	48.19	3.03
O2	48.19	3.03
V1	8.05	3.14
H2	7.65	2.85
CH3_sp3	98	3.75
CH2_sp3	46	3.95
CH_sp3	10	4.65
CH2_sp2	85	3.67
CH_sp2	47	3.73

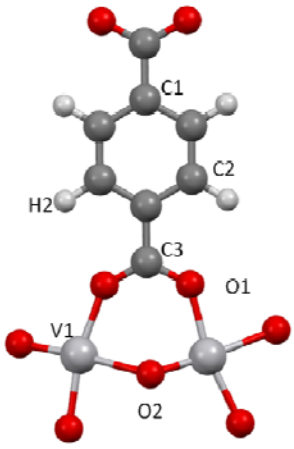

Table B2. Evolution of ε (in K) force field parameters for modeling ethane in MIL-47 (V) using PBE-D2 interaction energies.

Adsorbate atom type	MOF atom type	DREIDING	Iteration 1, FITTED_LJ	Iteration 2	Iteration 3 (PBE-D2 FF)
CH3_sp3_UA	C1	68.49	54.94	55.08	54.23
CH3_sp3_UA	C2	68.49	54.94	55.08	54.23
CH3_sp3_UA	C2	68.49	54.94	55.08	54.23
CH3_sp3_UA	O1	68.72	105.50	107.74	106.86
CH3_sp3_UA	O2	68.72	105.50	107.74	106.86
CH3_sp3_UA	V [#]	28.09	0.00	0.00	0.00
CH3_sp3_UA	H	27.38	8.19	4.03	6.13

[#] Note that the ε value for V-CH3_sp3_UA interaction has been set to zero.

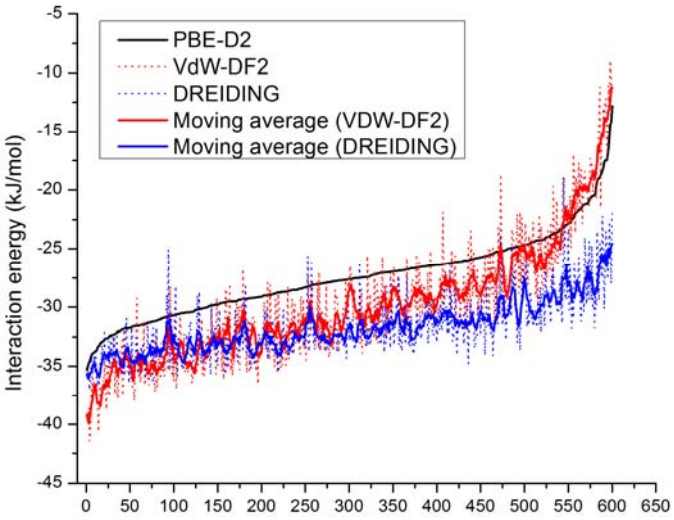

Figure B1. Interaction energies for 600 configurations of ethane in MIL-47(V) calculated using PBE-D2 (black, solid line) and VdW (red, dotted line), and DREIDING FF (blue, dotted line). The moving average forvdW-DF2 (red, solid line) and DREIDING FF (blue, solid line) is calculated using 5 configurations for each data point.

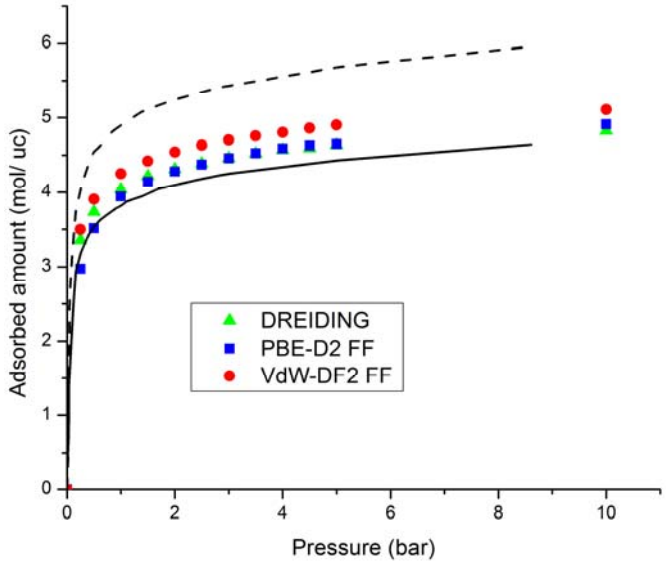

Figure B2. Adsorption isotherms for propane in MIL-47(V) using the PBE-D2 FF, VDW-DF2 FF and DREIDING FFs. The simulation data is compared to the scaled (dashed line) and unscaled (solid line) experimental data from Rosenbach et al. [97]

APPENDIX C

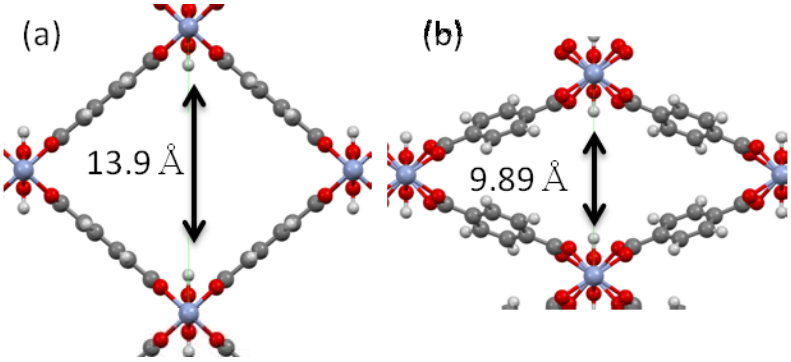

Figure C1. Schematic representation of the (a) LP and (b) NP form of MIL-53(Cr). The color scheme used is C (grey), O (red), H (white) and Cr (light blue).

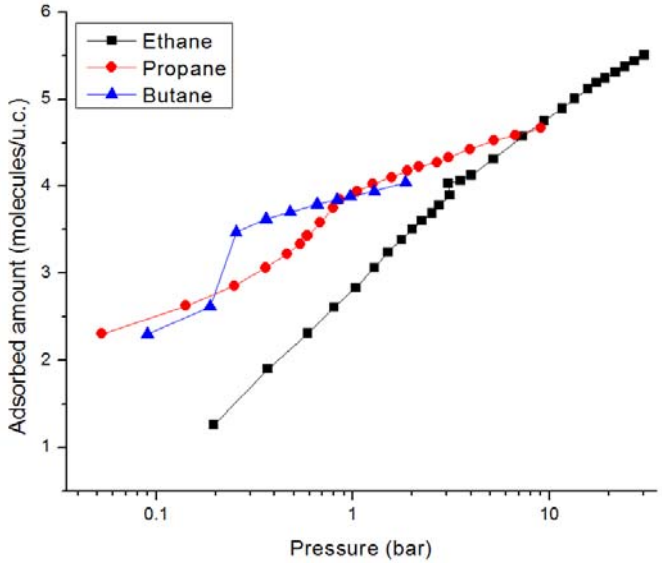

Figure C2. Experimental adsorption isotherms for ethane, propane and butane in MIL-53(Cr) at 303 K reported by Rosenbach et al. [97]

Details of MIL-53(Cr) calculations

DFT minimization of the atomic positions was perfomed in VASP using the vdW-DF2 functional. Other details are similar to those presented in Chapter 3 of the main text.

During the DFT optimization, the lattice constants were fixed at the values reported in the literature [99]. The "phase mixture" model was originally developed by Ghoufi et al. [125] for modeling CO_2 induced phase transitions in MIL-53(Cr). The procedure involves using a hybrid MD and GCMC approach to get an osmotic ensemble that allows volume fluctuations of the MIL-53(Cr) framework. A similar approach was used by Rosenbach et al. [97] to obtain the phase mixture model for propane and butane adsorption in MIL-53(Cr). In this work, we directly use their "phase mixture" results (Fig. 3.9 in the original publication[97]) in combination with our VDW-DF2 FF adsorption isotherms.

APPENDIX D

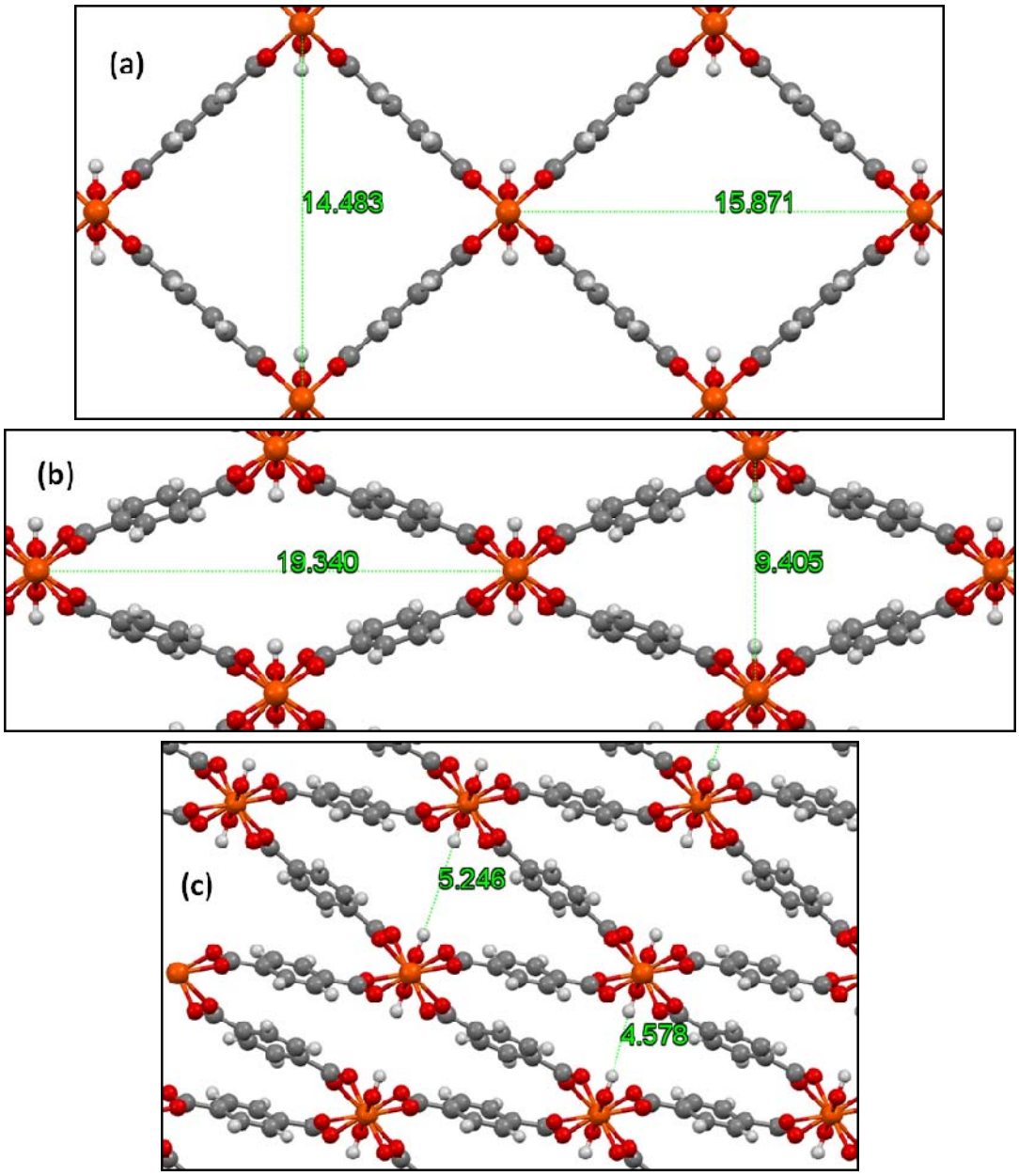

Figure D1. Schematic representation of the (a) LP and (b) NP and (c) INT form of MIL-53(Fe). The color scheme used is C (grey), O (red), H (white) and Fe (orange). Note that the INT structure consists of two types of pores, of which only one is available for adsorption.

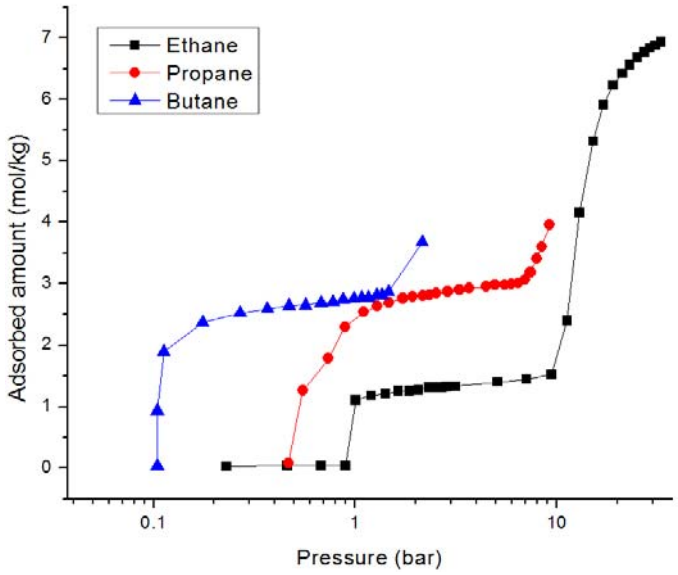

Figure D2. Experimental adsorption isotherms for ethane, propane and butane in MIL-53(Fe) at 303 K reported by Llewellyn et al. [100]

Table D1. Transition pressures corresponding to the steps observed in the ethane, propane and butane adsorption isotherms in MIL-53(Fe) at 303 K.

Isotherm		Transition pressure (bar)
Ethane	step1	1.01
	step2	11.25
Propane	step1	0.47
	step2	7.98
Butane	step1	0.10
	step2	1.46

APPENDIX E

Table E1 Parameters for the generic DREIDING[83] force field.

Atom Type	ε (K)	σ (Å)
C	47.86	3.47
O	48.19	3.03
Cu	2.52	3.11
H	7.65	2.85

Table E2 Parameters for the united atom TraPPE[106] FF for alkanes and alkenes.

Atom Type	ε (K)	σ (Å)
CH3_sp3	98	3.75
CH2_sp3	46	3.95
CH_sp3	10	4.65
CH2_sp2	85	3.675
CH_sp2	47	3.73

Table E3. Parameters for the alkane united atom FF from Dubbeldam et al. [158]

Atom Type	ε (K)	σ (Å)
CH3_sp3	98	3.75
CH2_sp3	46	3.95
CH_sp3	10	4.65

APPENDIX F

Table F1. The minimum DFT-D2 energy corresponding to each functionalized linker for the tbo, pto and fmj topology. The underlined values represent the minimum of the three topologies. In all the cases the pto topology is found to be more unfavorable than the fmj and/or the tbo topology.

Functional	**DFT-D2 (kcal/mol-linker)**		
group	tbo	pto	fmj
H-BTC	-3210.1	-3207.3	-3206.8
methyl	-3588.5	-3589.5	-3590.1
ethyl	-3969.8	-3973.0	-3973.6
methoxy	-3726.6	-3723.1	-3727.4
bromo	-3148.2	-3150.4	-3151.7
nitro	-3553.3	-3553.2	-3550.3
acetamide	-4240.4	-4226.5	-4236.5
amino	-3496.3	-3495.8	-3495.5

Table F2. Structural parameters of the minimum energy configurations for the various functionalized clusters obtained from the contour plots.

Linker	**Structural Parameters (θ, ϕ)**
H-BTC	120°, 0°
methyl	124°, 40°
ethyl	124°, 50°
methoxy	123°, 50°
bromo	123°, 60°
nitro	123°, 0°

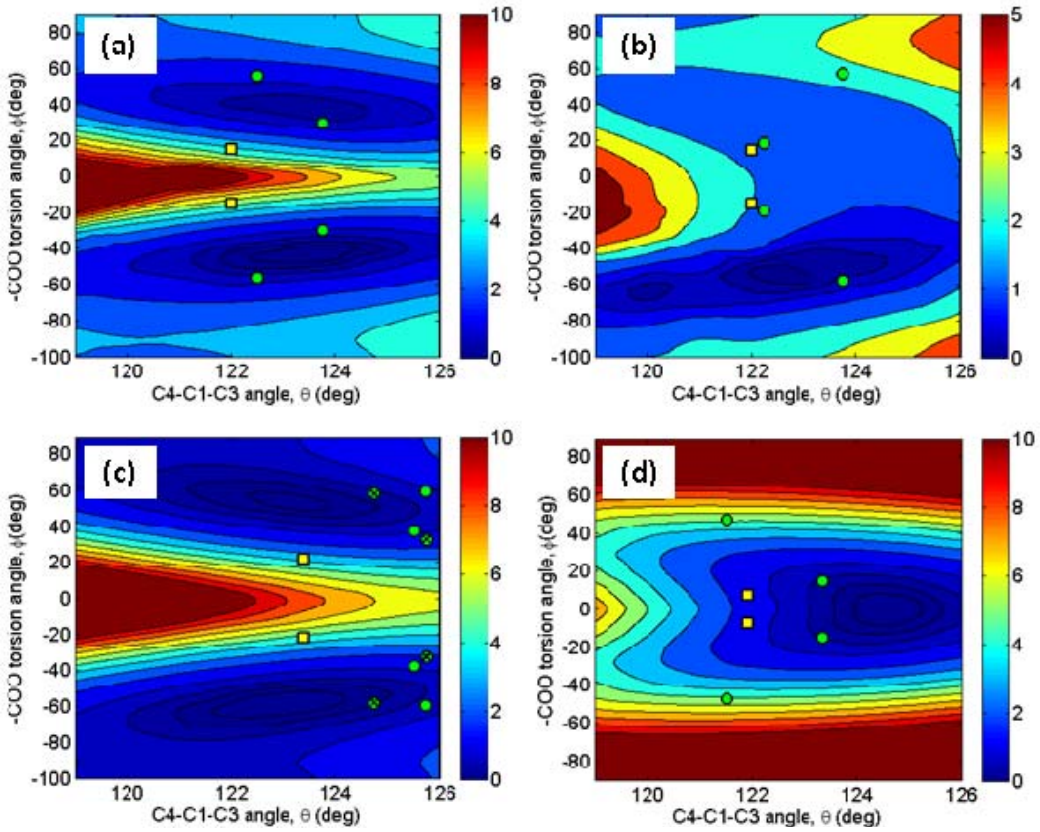

Figure F1 Contour plots of energy as a function of ϕ and θ for (a) methyl, (b) methoxy (c) bromo and (d) amino-BTC linkers. The yellow squares and green circles represent the structural parameters from the DFT-D2 optimized tbo and fmj topology respectively. For bromo-BTC (c), the green circles and the crossed green circles represents the structural parameters for two energy minimized fmj structures, each having different lattice parameters.

REFERENCES

(1) Lu, G. Q.; Zhao, X. S.; Wei, T. K. *Nanoporous materials: science and engineering*; Imperial College Press, 2004; Vol. 4.

(2) Wang, Q. M.; Shen, D. M.; Bulow, M.; Lau, M. L.; Deng, S. G.; Fitch, F. R.; Lemcoff, N. O.; Semanscin, J. *Microporous and Mesoporous Materials* **2002**, *55*, 217.

(3) Mueller, U.; Schubert, M.; Teich, F.; Puetter, H.; Schierle-Arndt, K.; Pastre, J. *Journal of Materials Chemistry* **2006**, *16*, 626.

(4) Li, H.; Eddaoudi, M.; O'Keeffe, M.; Yaghi, O. M. *Nature* **1999**, *402*, 276.

(5) Allen, F. H. *Acta Crystallographica Section B: Structural Science* **2002**, *58*, 380.

(6) Wang, Z.; Cohen, S. M. *Chemical Society Reviews* **2009**, *38*, 1315.

(7) Farha, O. K.; Hupp, J. T. *Accounts of Chemical Research* **2010**, *43*, 1166.

(8) Stock, N.; Biswas, S. *Chemical Reviews* **2011**, *112*, 933.

(9) Kim, M.; Cahill, J. F.; Fei, H.; Prather, K. A.; Cohen, S. M. *Journal of the American Chemical Society* **2012**, *134*, 18082.

(10) Chui, S. S.-Y.; Lo, S. M.-F.; Charmant, J. P. H.; Orpen, A. G.; Williams, I. D. *Science* **1999**, *283*, 1148.

(11) Rosi, N. L.; Kim, J.; Eddaoudi, M.; Chen, B.; O'Keeffe, M.; Yaghi, O. M. *Journal of the American Chemical Society* **2005**, *127*, 1504.

(12) Dincă, M.; Long, J. R. *Angewandte Chemie International Edition* **2008**, *47*, 6766.

(13) Chui, S. S. *Science* **1999**, *283*, 1148.

(14) Watanabe, T.; Sholl, D. S. *The Journal of Chemical Physics* **2010**, *133*, 094509.

(15) Sun, D.; Ma, S.; Simmons, J. M.; Li, J.-R.; Yuan, D.; Zhou, H.-C. *Chemical Communications* **2010**, *46*, 1329.

(16) Férey, G.; Mellot-Draznieks, C.; Serre, C.; Millange, F.; Dutour, J.; Surblé, S.; Margiolaki, I. *Science* **2005**, *309*, 2040.

(17) Serre, C.; Millange, F.; Thouvenot, C.; Nogues, M.; Marsolier, G.; Louer, D.; Ferey, G. *Journal of the American Chemical Society* **2002**, *124*, 13519.

(18) Eddaoudi, M.; Kim, J.; Rosi, N.; Vodak, D.; Wachter, J.; O'Keeffe, M.; Yaghi, O. M. *Science* **2002**, *295*, 469.

(19) Park, K. S.; Ni, Z.; Côté, A. P.; Choi, J. Y.; Huang, R.; Uribe-Romo, F. J.; Chae, H. K.; O'Keeffe, M.; Yaghi, O. M. *Proceedings of the National Academy of Sciences* **2006**, *103*, 10186.

(20) Frenkel, D.; Smit, B. *Understanding Molecular Simulation, Second Edition: From Algorithms to Applications (Computational Science)*; Academic Press, 2001.

(21) Grajciar, L.; Bludsky, O.; Nachtigall, P. *J. Phys. Chem. Lett.* **2010**, *1*, 3354.

(22) Seminario, J. M. *Recent developments and applications of modern density functional theory*; Elsevier, 1996; Vol. 4.

(23) Geerlings, P.; De Proft, F.; Langenaeker, W. *Chemical Reviews* **2003**, *103*, 1793.

(24) Fang, H.; Kamakoti, P.; Zang, J.; Cundy, S.; Paur, C.; Ravikovitch, P. I.; Sholl, D. S. *The Journal of Physical Chemistry C* **2012**, *116*, 10692.

(25) Solomon, S.; Qin, D.; Manning, M.; Chen, Z.; Marquis, M.; Averyt, K. B.; Tignor, M.; Miller, H. L. *Summary for Policymakers: The physical science basis. Contribution of Working Group I to the Fourth assessment report of the*

Intergovernmental Panel on Climate Change; 2 ed.; Cambridge University Press, Cambridge, United Kingdom and New York, NY, USA, 2007.

(26) Choi, S.; Drese, J. H.; Jones, C. W. *ChemSusChem* **2009**, *2*, 796.

(27) Jones, C. W. *Annual Review of Chemical and Biomolecular Engineering* **2011**, *2*, 31.

(28) House, K. Z.; Baclig, A. C.; Ranjan, M.; van Nierop, E. A.; Wilcox, J.; Herzog, H. J. *Proc. Natl. Acad. Sci. U. S. A.* **2011**, *108*, 20428.

(29) Keith, D. W.; Ha-Duong, M.; Stolaroff, J. K. *Clim. Change* **2006**, *74*, 17.

(30) Krishna, R.; van Baten, J. M. *Physical Chemistry Chemical Physics* **2011**, *13*, 10593.

(31) Lackner, K. S.; Grimes, P.; Ziock, H.-J. In *Proceedings of the First National Conference on Carbon Sequestration* Washington, DC, USA, 2001.

(32) Lackner, K. S.; Ziock, H.-J.; Grimes, P. In *24th International Conference on Coal Utilization & Fuel Systems* Clearwater, FL, 1999.

(33) Zeman, F. S.; Lackner, K. S. *World Resource Review* **2004**, *16*, 157.

(34) Lackner, K. S. *Eur. Phys. J.-Spec. Top.* **2009**, *176*, 93.

(35) Hicks, J. C.; Drese, J. H.; Fauth, D. J.; Gray, M. L.; Qi, G. G.; Jones, C. W. *Journal of the American Chemical Society* **2008**, *130*, 2902.

(36) Choi, S.; Drese, J. H.; Eisenberger, P. M.; Jones, C. W. In *AIChE Annual Meeting* Nashville, TN, 2009.

(37) Belmabkhout, Y.; Serna-Guerrero, R.; Sayari, A. *Chemical Engineering Science* **2010**, *65*, 3695.

(38) Gebald, C.; Wurzbacher, J. A.; Tingaut, P.; Zimmermann, T.; Steinfeld, A. *Environ. Sci. Technol.* **2011**, *45*, 9101.

(39) Choi, S.; Drese, J. H.; Eisenberger, P. M.; Jones, C. W. *Environ. Sci. Technol.* **2011**, *45*, 2420.

(40) Choi, S.; Gray, M. L.; Jones, C. W. *ChemSusChem* **2011**, *4*, 628.

(41) Goeppert, A.; Czaun, M.; May, R. B.; Prakash, G. K. S.; Olah, G. A.; Narayanan, S. R. *Journal of the American Chemical Society* **2011**, *133*, 20164.

(42) Didas, S. A.; Kulkarni, A. R.; Sholl, D. S.; Jones, C. W. In *ChemSusChem (In Press)* 2012.

(43) Serna-Guerrero, R.; Sayari, A. *Chem. Eng. J.* **2010**, *161*, 182.

(44) Sayari, A.; Belmabkhout, Y. *Journal of the American Chemical Society* **2010**, *132*, 6312.

(45) Serna-Guerrero, R.; Belmabkhout, Y.; Sayari, A. *Adsorption-Journal of the International Adsorption Society* **2010**, *16*, 567.

(46) Serna-Guerrero, R.; Da'na, E.; Sayari, A. *Industrial & Engineering Chemistry Research* **2008**, *47*, 9406.

(47) Wurzbacher, J. A.; Gebald, C.; Steinfeld, A. *Energy & Environmental Science* **2011**, *4*, 3584.

(48) Li, W.; Choi, S.; Drese, J. H.; Hornbostel, M.; Krishnan, G.; Eisenberger, P. M.; Jones, C. W. *ChemSusChem* **2010**, *3*, 899.

(49) Choi, S.; Watanabe, T.; Bae, T.-H.; Sholl, D. S.; Jones, C. W. *The Journal of Physical Chemistry Letters* **2012**, *3*, 1136.

(50) Dzubak, A. L.; Lin, L. C.; Kim, J.; Swisher, J. A.; Poloni, R.; Maximoff, S. N.; Smit, B.; Gagliardi, L. *Nature Chemistry* **2012**, *4*, 810.

(51) Lin, L.-C.; Lee, K.; Gagliardi, L.; Neaton, J. B.; Smit, B. *Journal of Chemical Theory and Computation* **2014**, *10*, 1477.

(52) Elimelech, M.; Phillip, W. A. *Science* **2011**, *333*, 712.

(53) Eisenberger, P. M.; Chichilnisky, G. US, 2010; Vol. 12/793,504.

(54) Trung, T. K.; Déroche, I.; Rivera, A.; Yang, Q.; Yot, P.; Ramsahye, N.; Vinot, S. D.; Devic, T.; Horcajada, P.; Serre, C.; Maurin, G.; Trens, P. *Microporous and Mesoporous Materials* **2011**, *140*, 114.

(55) Harlick, P. J. E.; Sayari, A. *Industrial & Engineering Chemistry Research* **2007**, *46*, 446.

(56) Harlick, P. J. E.; Sayari, A. *Industrial & Engineering Chemistry Research* **2006**, *45*, 3248.

(57) Serna-Guerrero, R.; Belmabkhout, Y.; Sayari, A. *Chem. Eng. J.* **2010**, *161*, 173.

(58) Belmabkhout, Y.; Sayari, A. *Adsorption-Journal of the International Adsorption Society* **2009**, *15*, 318.

(59) Serna-Guerrero, R.; Belmabkhout, Y.; Sayari, A. *Chem. Eng. J.* **2010**, *158*, 513.

(60) Li, W.; Bollini, P.; Didas, S. A.; Choi, S.; Drese, J. H.; Jones, C. W. *Acs Applied Materials & Interfaces* **2010**, *2*, 3363.

(61) Bird, R. B.; Stewart, W. E.; Lightfoot, E. N. *Transport Phenomena*; 2 ed.; Wiley, 2010.

(62) House, K. Z.; Harvey, C. F.; Aziz, M. J.; Schrag, D. P. *Energy & Environmental Science* **2009**, *2*, 193.

(63) Bollini, P.; Choi, S.; Drese, J. H.; Jones, C. W. *Energy & Fuels* **2011**, *25*, 2416.

(64) U.S. Department of Energy Energy Information Administration: Electricity Emission Factors, http://www.eia.doe.gov/oiaf/1605/pdf/Appendix%20F_r071023.pdf

(65) Bae, Y.-S.; Yazaydın, A. Ö.; Snurr, R. Q. *Langmuir* **2010**, *26*, 5475.

(66) U.S. Department of Energy Energy Information Administration: Annual Energy Outlook 2012 (Early Release Overview), http://www.eia.gov/forecasts/aeo/er/pdf/0383er(2012).pdf

(67) Smith, R.; Varbanov, P. *CEP* **2005**, *101*, 29.

(68) Herm, Z. R.; Bloch, E. D.; Long, J. R. *Chemistry of Materials* **2013**, *26*, 323.

(69) Fischer, M.; Gomes, J. R. B.; Froeba, M.; Jorge, M. *Langmuir* **2012**, *28*, 8537.

(70) Rubes, M.; Wiersum, A. D.; Llewellyn, P. L.; Grajciar, L.; Bludsky, O.; Nachtigall, P. *Journal of Physical Chemistry C* **2013**, *117*, 11159.

(71) Kim, H.; Park, J.; Jung, Y. *Physical Chemistry Chemical Physics* **2013**, *15*, 19644.

(72) Geier, S. J.; Mason, J. A.; Bloch, E. D.; Queen, W. L.; Hudson, M. R.; Brown, C. M.; Long, J. R. *Chemical Science* **2013**, *4*, 2054.

(73) Maes, M.; Alaerts, L.; Vermoortele, F.; Ameloot, R.; Couck, S.; Finsy, V.; Denayer, J. F. M.; De Vos, D. E. *Journal of the American Chemical Society* **2010**, *132*, 2284.

(74) Hartmann, M.; Kunz, S.; Himsl, D.; Tangermann, O.; Ernst, S.; Wagener, A. *Langmuir* **2008**, *24*, 8634.

(75) He, Y.; Krishna, R.; Chen, B. *Energy & Environmental Science* **2012**, *5*, 9107.

(76) Luebbers, M. T.; Wu, T.; Shen, L.; Masel, R. I. *Langmuir* **2010**, *26*, 11319.

(77) Barcia, P. S.; Guimaraes, D.; Mendes, P. A. P.; Silva, J. A. C.; Guillerm, V.; Chevreau, H.; Serre, C.; Rodrigues, A. E. *Microporous and Mesoporous Materials* **2011**, *139*, 67.

(78) Van Der Voort, P.; Leus, K.; Liu, Y.-Y.; Vandichel, M.; Van Speybroeck, V.; Waroquier, M.; Biswas, S. *New Journal of Chemistry* **2014**, *38*, 1853.

(79) Alaerts, L.; Kirschhock, C. E. A.; Maes, M.; van der Veen, M. A.; Finsy, V.; Depla, A.; Martens, J. A.; Baron, G. V.; Jacobs, P. A.; Denayer, J. E. M.; De Vos, D. E. *Angewandte Chemie-International Edition* **2007**, *46*, 4293.

(80) Castillo, J. M.; Vlugt, T. J. H.; Calero, S. *Journal of Physical Chemistry C* **2009**, *113*, 20869.

(81) Haldoupis, E.; Nair, S.; Sholl, D. S. *Journal of the American Chemical Society* **2012**, *134*, 4313.

(82) Christopher, E. W.; Michael, L.; Chang Yeon, L.; Omar, K. F.; Brad, G. H.; Joseph, T. H.; Randall, Q. S. *Nature Chemistry* **2011**, *4*, 83.

(83) Mayo, S. L.; Olafson, B. D.; Goddard, W. A. *Journal of Physical Chemistry* **1990**, *94*, 8897.

(84) Rappe, A. K.; Casewit, C. J.; Colwell, K. S.; Goddard, W. A.; Skiff, W. M. *Journal of the American Chemical Society* **1992**, *114*, 10024.

(85) Zang, J.; Nair, S.; Sholl, D. S. *The Journal of Physical Chemistry C* **2013**, *117*, 7519.

(86) Nicholson, T. M.; Bhatia, S. K. *Adsorption Science & Technology* **2007**, *25*, 607.

(87) Jorge, M.; Lamia, N.; Rodrigues, A. E. *Colloids and Surfaces a-Physicochemical and Engineering Aspects* **2010**, *357*, 27.

(88) Lamia, N.; Jorge, M.; Granato, M. A.; Almeida Paz, F. A.; Chevreau, H.; Rodrigues, A. E. *Chemical Engineering Science* **2009**, *64*, 3246.

(89) Fang, H.; Demir, H.; Kamakoti, P.; Sholl, D. S. *Journal of Materials Chemistry A* **2014**, *2*, 274.

(90) Getman, R. B.; Bae, Y.-S.; Wilmer, C. E.; Snurr, R. Q. *Chemical Reviews* **2011**, *112*, 703.

(91) Han, S. S.; Mendoza-Cortes, J. L.; Goddard Iii, W. A. *Chemical Society Reviews* **2009**, *38*, 1460.

(92) Yang, Q.; Liu, D.; Zhong, C.; Li, J.-R. *Chemical Reviews* **2013**, *113*, 8261.

(93) Borycz, J.; Lin, L.-C.; Bloch, E. D.; Kim, J.; Dzubak, A. L.; Maurice, R.; Semrouni, D.; Lee, K.; Smit, B.; Gagliardi, L. *The Journal of Physical Chemistry C* **2014**, *118*, 12230.

(94) Fang, H.; Kamakoti, P.; Ravikovitch, P. I.; Aronson, M.; Paur, C.; Sholl, D. S. *Physical Chemistry Chemical Physics* **2013**, *15*, 12882.

(95) Chen, L.; Morrison, C. A.; Düren, T. *The Journal of Physical Chemistry C* **2012**, *116*, 18899.

(96) Deroche, I.; Rives, S.; Trung, T.; Yang, Q.; Ghoufi, A.; Ramsahye, N. A.; Trens, P.; Fajula, F.; Devic, T.; Serre, C.; Ferey, G.; Jobic, H.; Maurin, G. *Journal of Physical Chemistry C* **2011**, *115*, 13868.

(97) Rosenbach, N., Jr.; Ghoufi, A.; Deroche, I.; Llewellyn, P. L.; Devic, T.; Bourrelly, S.; Serre, C.; Ferey, G.; Maurin, G. *Physical Chemistry Chemical Physics* **2010**, *12*, 6428.

(98) Rives, S.; Jobic, H.; Ragon, F.; Devic, T.; Serre, C.; Férey, G.; Ollivier, J.; Maurin, G. *Microporous and Mesoporous Materials* **2012**, *164*, 259.

(99) Llewellyn, P. L.; Maurin, G.; Devic, T.; Loera-Serna, S.; Rosenbach, N.; Serre, C.; Bourrelly, S.; Horcajada, P.; Filinchuk, Y.; Ferey, G. *Journal of the American Chemical Society* **2008**, *130*, 12808.

(100) Llewellyn, P. L.; Horcajada, P.; Maurin, G.; Devic, T.; Rosenbach, N.; Bourrelly, S.; Serre, C.; Vincent, D.; Loera-Serna, S.; Filinchuk, Y.; Ferey, G. *Journal of the American Chemical Society* **2009**, *131*, 13002.

(101) Barthelet, K.; Marrot, J.; Riou, D.; Férey, G. *Angewandte Chemie International Edition* **2002**, *41*, 281.

(102) Perdew, J. P.; Burke, K.; Ernzerhof, M. *Physical Review Letters* **1996**, *77*, 3865.

(103) Grimme, S. *Journal of Computational Chemistry* **2006**, *27*, 1787.

(104) Kresse, G.; Joubert, D. *Physical Review B* **1999**, *59*, 1758.

(105) Siepmann, J. I.; Frenkel, D. *Molecular Physics* **1992**, *75*, 59.

(106) Martin, M. G.; Siepmann, J. I. *The Journal of Physical Chemistry B* **1998**, *102*, 2569.

(107) Lee, K.; Murray, É. D.; Kong, L.; Lundqvist, B. I.; Langreth, D. C. *Physical Review B* **2010**, *82*, 081101.

(108) Dubbeldam, D.; Torres-Knoop, A.; Walton, K. S. *Molecular Simulation* **2013**, *39*, 1253.

(109) Fischer, M.; Gomes, J. R. B.; Jorge, M. *Molecular Simulation* **2014**, *40*, 537.

(110) Walton, K. S.; Snurr, R. Q. *Journal of the American Chemical Society* **2007**, *129*, 8552.

(111) Rouquerol, J.; Llewellyn, P.; Rouquerol, F. In *Studies in Surface Science and Catalysis*; P.L. Llewellyn, F. R.-R. J. R., Seaton, N., Eds.; Elsevier: 2007; Vol. Volume 160, p 49.

(112) Finsy, V.; Calero, S.; Garcia-Perez, E.; Merkling, P. J.; Vedts, G.; De Vos, D. E.; Baron, G. V.; Denayer, J. F. M. *Physical Chemistry Chemical Physics* **2009**, *11*, 3515.

(113) Jobic, H.; Rosenbach, N.; Ghoufi, A.; Kolokolov, D. I.; Yot, P. G.; Devic, T.; Serre, C.; Férey, G.; Maurin, G. *Chemistry – A European Journal* **2010**, *16*, 10337.

(114) Sholl, D. S. *Accounts of Chemical Research* **2006**, *39*, 403.

(115) Douglass, D. C.; McCall, D. W. *The Journal of Physical Chemistry* **1958**, *62*, 1102.

(116) Leroy, F.; Rousseau, B.; Fuchs, A. H. *Physical Chemistry Chemical Physics* **2004**, *6*, 775.

(117) Millange, F.; Serre, C.; Ferey, G. *Chemical Communications* **2002**, 822.

(118) Alhamami, M.; Doan, H.; Cheng, C.-H. *Materials* **2014**, *7*, 3198.

(119) Coudert, F.-X.; Jeffroy, M.; Fuchs, A. H.; Boutin, A.; Mellot-Draznieks, C. *Journal of the American Chemical Society* **2008**, *130*, 14294.

(120) Volkringer, C.; Loiseau, T.; Guillou, N.; Ferey, G.; Elkaim, E.; Vimont, A. *Dalton Transactions* **2009**, 2241.

(121) Chen, L.; Mowat, J. P. S.; Fairen-Jimenez, D.; Morrison, C. A.; Thompson, S. P.; Wright, P. A.; Düren, T. *Journal of the American Chemical Society* **2013**, *135*, 15763.

(122) Coudert, F.-X.; Ortiz, A. U.; Haigis, V.; Bousquet, D.; Fuchs, A. H.; Ballandras, A.; Weber, G.; Bezverkhyy, I.; Geoffroy, N.; Bellat, J.-P.; Ortiz, G.; Chaplais, G.; Patarin, J.; Boutin, A. *The Journal of Physical Chemistry C* **2014**, *118*, 5397.

(123) Coudert, F.-X.; Boutin, A.; Fuchs, A. H. *Molecular Physics* **2014**, *112*, 1257.

(124) Schneemann, A.; Bon, V.; Schwedler, I.; Senkovska, I.; Kaskel, S.; Fischer, R. A. *Chemical Society Reviews* **2014**, *43*, 6062.

(125) Ghoufi, A.; Maurin, G. *The Journal of Physical Chemistry C* **2010**, *114*, 6496.

(126) Millange, F.; Guillou, N.; Walton, R. I.; Greneche, J.-M.; Margiolaki, I.; Ferey, G. *Chemical Communications* **2008**, 4732.

(127) Coudert, F.-X.; Mellot-Draznieks, C.; Fuchs, A. H.; Boutin, A. *Journal of the American Chemical Society* **2009**, *131*, 11329.

(128) Bourrelly, S.; Moulin, B.; Rivera, A.; Maurin, G.; Devautour-Vinot, S.; Serre, C.; Devic, T.; Horcajada, P.; Vimont, A.; Clet, G.; Daturi, M.; Lavalley, J.-C.; Loera-Serna, S.; Denoyel, R.; Llewellyn, P. L.; Férey, G. *Journal of the American Chemical Society* **2010**, *132*, 9488.

(129) Boutin, A.; Couck, S.; Coudert, F.-X.; Serra-Crespo, P.; Gascon, J.; Kapteijn, F.; Fuchs, A. H.; Denayer, J. F. M. *Microporous and Mesoporous Materials* **2011**, *140*, 108.

(130) Bae, Y.-S.; Snurr, R. Q. *Microporous and Mesoporous Materials* **2010**, *132*, 300.

(131) Fischer, M.; Hoffmann, F.; Fröba, M. *ChemPhysChem* **2009**, *10*, 2647.

(132) Mu, W.; Liu, D.; Yang, Q.; Zhong, C. *Microporous and Mesoporous Materials* **2010**, *130*, 76.

(133) Babarao, R.; Jiang, J.; Sandler, S. I. *Langmuir* **2008**, *25*, 5239.

(134) Yazaydın, A. Ö.; Snurr, R. Q.; Park, T.-H.; Koh, K.; Liu, J.; LeVan, M. D.; Benin, A. I.; Jakubczak, P.; Lanuza, M.; Galloway, D. B.; Low, J. J.; Willis, R. R. *Journal of the American Chemical Society* **2009**, *131*, 18198.

(135) Dzubak, A. L.; Lin, L.-C.; Kim, J.; Swisher, J. A.; Poloni, R.; Maximoff, S. N.; Smit, B.; Gagliardi, L. *Nat Chem* **2012**, *4*, 810.

(136) Ozturk, T. N.; Keskin, S. *The Journal of Physical Chemistry C* **2014**, *118*, 13988.

(137) Sun, W.; Lin, L.-C.; Peng, X.; Smit, B. *AIChE Journal* **2014**, *60*, 2314.

(138) Parkes, M. V.; Staiger, C. L.; Perry Iv, J. J.; Allendorf, M. D.; Greathouse, J. A. *Physical Chemistry Chemical Physics* **2013**, *15*, 9093.

(139) Meek, S. T.; Greathouse, J. A.; Allendorf, M. D. *Advanced Materials* **2011**, *23*, 249.

(140) Lin, L.-C.; Berger, A. H.; Martin, R. L.; Kim, J.; Swisher, J. A.; Jariwala, K.; Rycroft, C. H.; Bhown, A. S.; Deem, M. W.; Haranczyk, M.; Smit, B. *Nat Mater* **2012**, *11*, 633.

(141) Han, S. S.; Kim, D.; Jung, D. H.; Cho, S.; Choi, S.-H.; Jung, Y. *The Journal of Physical Chemistry C* **2012**, *116*, 20254.

(142) Li, W.; Grimme, S.; Krieg, H.; Möllmann, J.; Zhang, J. *The Journal of Physical Chemistry C* **2012**, *116*, 8865.

(143) Jorge, M.; Fischer, M.; Gomes, J. R. B.; Siquet, C.; Santos, J. C.; Rodrigues, A. E. *Industrial & Engineering Chemistry Research* **2014**.

(144) Fischer, M.; Kuchta, B.; Firlej, L.; Hoffmann, F.; Fröba, M. *The Journal of Physical Chemistry C* **2010**, *114*, 19116.

(145) Han, S. S.; Goddard, W. A. *The Journal of Physical Chemistry C* **2008**, *112*, 13431.

(146) Chen, L.; Grajciar, L.; Nachtigall, P.; Düren, T. *The Journal of Physical Chemistry C* **2011**, *115*, 23074.

(147) Toda, J.; Fischer, M.; Jorge, M.; Gomes, J. R. B. *Chemical Physics Letters* **2013**, *587*, 7.

(148) McDaniel, J. G.; Schmidt, J. R. *The Journal of Physical Chemistry A* **2013**, *117*, 2053.

(149) McDaniel, J. G.; Yu, K.; Schmidt, J. R. *The Journal of Physical Chemistry C* **2011**, *116*, 1892.

(150) Nicholson, T.; Bhatia, S. *Adsorption Science & Technology* **2007**, *25*, 607.

(151) Wang, S.; Yang, Q.; Zhong, C. *Separation and Purification Technology* **2008**, *60*, 30.

(152) Lamia, N.; Jorge, M.; Granato, M. A.; Almeida Paz, F. A.; Chevreau, H.; Rodrigues, A. E. *Chemical Engineering Science* **2009**, *64*, 3246.

(153) Jorge, M.; Lamia, N.; Rodrigues, A. E. *Colloids and Surfaces A: Physicochemical and Engineering Aspects* **2010**, *357*, 27.

(154) Ferreira, A. F. P.; Santos, J. C.; Plaza, M. G.; Lamia, N.; Loureiro, J. M.; Rodrigues, A. E. *Chem. Eng. J.* **2011**, *167*, 1.

(155) Plaza, M. G.; Ferreira, A. F. P.; Santos, J. C.; Ribeiro, A. M.; Müller, U.; Trukhan, N.; Loureiro, J. M.; Rodrigues, A. E. *Microporous and Mesoporous Materials* **2012**, *157*, 101.

(156) Plaza, M. G.; Ribeiro, A. M.; Ferreira, A.; Santos, J. C.; Lee, U. H.; Chang, J.-S.; Loureiro, J. M.; Rodrigues, A. E. *Separation and Purification Technology* **2012**, *90*, 109.

(157) Watanabe, T.; Sholl, D. S. *The Journal of Chemical Physics* **2010**, *133*.

(158) Dubbeldam, D.; Calero, S.; Vlugt, T. J. H.; Krishna, R.; Maesen, T. L. M.; Smit, B. *The Journal of Physical Chemistry B* **2004**, *108*, 12301.

(159) Chung, Y. G.; Camp, J.; Haranczyk, M.; Sikora, B. J.; Bury, W.; Krungleviciute, V.; Yildirim, T.; Farha, O. K.; Sholl, D. S.; Snurr, R. Q. *Chemistry of Materials* **2014**.

(160) Ferey, G. *Chem Soc Rev* **2008**, *37*, 191.

(161) James, S. L. *Chemical Society Reviews* **2003**, *32*, 276.

(162) Kitagawa, S.; Kitaura, R.; Noro, S. *Angewandte Chemie* **2004**, *43*, 2334.

(163) Czaja, A. U.; Trukhan, N.; Muller, U. *Chem Soc Rev* **2009**, *38*, 1284.

(164) O'Keeffe, M. *Chem Soc Rev* **2009**, *38*, 1215.

(165) Yaghi, O. M.; O'Keeffe, M.; Ockwig, N. W.; Chae, H. K.; Eddaoudi, M.; Kim, J. *Nature* **2003**, *423*, 705.

(166) Cmarik, G. E.; Kim, M.; Cohen, S. M.; Walton, K. S. *Langmuir* **2012**, *28*, 15606.

(167) Huang, Y.; Qin, W.; Li, Z.; Li, Y. *Dalton Trans* **2012**, *41*, 9283.

(168) Kandiah, M.; Nilsen, M. H.; Usseglio, S.; Jakobsen, S.; Olsbye, U.; Tilset, M.; Larabi, C.; Quadrelli, E. A.; Bonino, F.; Lillerud, K. P. *Chemistry of Materials* **2010**, *22*, 6632.

(169) Biswas, S.; Ahnfeldt, T.; Stock, N. *Inorganic chemistry* **2011**, *50*, 9518.

(170) Serra-Crespo, P.; Gobechiya, E.; Ramos-Fernandez, E. V.; Juan-Alcaniz, J.; Martinez-Joaristi, A.; Stavitski, E.; Kirschhock, C. E.; Martens, J. A.; Kapteijn, F.; Gascon, J. *Langmuir* **2012**, *28*, 12916.

(171) Cai, Y.; Zhang, Y.; Huang, Y.; Marder, S. R.; Walton, K. S. *Crystal Growth & Design* **2012**, *12*, 3709.

(172) Blatov, V. A.; Shevchenko, A. P.; Serezhkin, V. N. *Journal of Applied Crystallography* **2000**, *33*, 1193.

(173) O'Keeffe, M.; Peskov, M. A.; Ramsden, S. J.; Yaghi, O. M. *Accounts of Chemical Research* **2008**, *41*, 1782.

(174) Peikert, K.; Hoffmann, F.; Froba, M. *Chem Commun (Camb)* **2012**, *48*, 11196.

(175) Wilmer, C. E.; Leaf, M.; Lee, C. Y.; Farha, O. K.; Hauser, B. G.; Hupp, J. T.; Snurr, R. Q. *Nature Chemistry* **2012**, *4*, 83.

(176) Cai, Y.; Kulkarni, A. R.; Huang, Y.-g.; Sholl, D. S.; Walton, K. S. *Crystal Growth & Design* **2014**.

(177) Kresse, G.; Furthmüller, J. *Physical Review B* **1996**, *54*, 11169.

(178) Vitillo, J. G.; Regli, L.; Chavan, S.; Ricchiardi, G.; Spoto, G.; Dietzel, P. D. C.; Bordiga, S.; Zecchina, A. *Journal of the American Chemical Society* **2008**, *130*, 8386.

(179) Düren, T.; Millange, F.; Férey, G.; Walton, K. S.; Snurr, R. Q. *The Journal of Physical Chemistry C* **2007**, *111*, 15350.

(180) Chen, B.; Eddaoudi, M.; Hyde, S. T.; O'Keeffe, M.; Yaghi, O. M. *Science* **2001**, *291*, 1021.

(181) Amirjalayer, S.; Tafipolsky, M.; Schmid, R. *The Journal of Physical Chemistry C* **2011**, *115*, 15133.

(182) Tafipolsky, M.; Schmid, R. *The Journal of Physical Chemistry B* **2009**, *113*, 1341.

(183) Bureekaew, S.; Schmid, R. *CrystEngComm* **2013**, *15*, 1551.

(184) Lewis, D. W.; Ruiz-Salvador, A. R.; Gomez, A.; Rodriguez-Albelo, L. M.; Coudert, F.-X.; Slater, B.; Cheetham, A. K.; Mellot-Draznieks, C. *CrystEngComm* **2009**, *11*, 2272.

(185) Baburin, I. A.; Leoni, S.; Seifert, G. *The Journal of Physical Chemistry B* **2008**, *112*, 9437.

(186) Peikert, K.; Hoffmann, F.; Froba, M. *Chem Commun (Camb)* **2012**, *48*, 11196.

(187) Savin, A.; Nesper, R.; Wengert, S.; Fässler, T. F. *Angewandte Chemie International Edition in English* **1997**, *36*, 1808.

(188) Liu, Y.; Wang, Z. U.; Zhou, H.-C. *Greenhouse Gases-Science and Technology* **2012**, *2*, 239.

(189) Kulkarni, A. R.; Sholl, D. S. *Industrial & Engineering Chemistry Research* **2012**, *51*, 8631.

(190) Rudenko, A. N.; Bendt, S.; Keil, F. J. *The Journal of Physical Chemistry C* **2014**, *118*, 16218.

(191) Awati, R. V.; Ravikovitch, P. I.; Sholl, D. S. *The Journal of Physical Chemistry C* **2013**, *117*, 13462.

(192) Pulido, A.; Delgado, M. R.; Bludsky, O.; Rubes, M.; Nachtigall, P.; Arean, C. O. *Energy & Environmental Science* **2009**, *2*, 1187.

(193) Bludsky, O.; Rubes, M.; Soldan, P.; Nachtigall, P. *Journal of Chemical Physics* **2008**, *128*.